MULTISCALE STRUCTURED SURFACES AND THEIR EFFECT ON DRAG & FLUID FLOW

by

Elliot Jenner

Bachelor of Science in Physics, Rochester Institute of Technology,

2007

Submitted to the Graduate Faculty of

the Kenneth P. Dietrich School of Arts and Sciences Department of

Physics & Astronomy in partial fulfillment

of the requirements for the degree of

Doctor of Philosophy

University of Pittsburgh

2015

UNIVERSITY OF PITTSBURGH

KENNETH P. DIETRICH SCHOOL OF ARTS AND SCIENCES

This dissertation was presented

by

Elliot Jenner

It was defended on

February 26th 2015

and approved by

Brian D'Urso, Physics

Gurudev Dutt, Physics

Robert Coalson, Chemistry

Paul Shepard, Physics

Judith Yang, Chemical and Petroleum Engineering

Dissertation Director: Brian D'Urso, Physics

MULTISCALE STRUCTURED SURFACES AND THEIR EFFECT ON DRAG & FLUID FLOW

Elliot Jenner, PhD

University of Pittsburgh, 2015

In this thesis, we examine surface modification as a method for reducing fluid drag on a surface. Reducing drag is of great interest for many applications, including in ship construction, fluid pipelines, self-cleaning surfaces, and for use in MicroElectroMechanical Systems. Multiscale structured hydrophobic surfaces can reduce fluid drag, depending on surface chemistry and structure geometry. We examine the properties of artificial version of bio-inspired hydrophobic surfaces with multiple wetting states, including some not previously tested or known to exist.

Multiscale surfaces have structure on a small and a large scale. We evaluate the effect of changes in the large scale features on drag properties. We also vary the fluid state on the surfaces by application or removal of a passively retained secondary liquid. We examine the fluid properties in a number of ways, including torque and shear rate measurement in a custom made Cone & Plate Rheometer.

Conventional shear rate measurements in a Cone & Plate Rheometer depend on knowledge of the interface; since we are measuring unknown surfaces, we must develop an alternative method. We measure the components of the shear rate tensor $\mathcal{S}$ directly using Photon Correlation Spectroscopy, where we develop a general theoretical treatment for measuring 3-D flows with this technique. Previous work on Photon Correlation Spectroscopy has involved only approximate solutions, requiring free parameters to be scaled by a known case, or special cases, such as 2-D flow.

TABLE OF CONTENTS

LIST OF TABLES

LIST OF FIGURES

PREFACE

I would like to thank Dr. Walter Goldburg (Department of Physics, University of Pittsburgh, Emeritus), without whom I would never have known about or experimented with Photon Correlation Spectroscopy. I would also like to think him for his assistance with the theory thereof, and for the use of necessary equipment to perform experiments utilizing this measurement technique.

I would like to thank Dr. Charlotte Barbier (Center for Nanophase Materials Science, Oak Ridge National Laboratory) for her collaboration on initial torque measurements.

I would like to thank Dr. Kenneth Brakke (Mathematics Department, Susquehanna University), the creator of Surface Evolver, for his assistance with understanding and optimizing our simulation.

1.0 INTRODUCTION

In this thesis, we examine surface modification as a method for reducing fluid drag on a surface. Reducing drag is important in many fields. One area in which the development of drag reducing surfaces has the potential for application is ship design; significant fuel costs are associated with overcoming the effects of drag on ship hulls [1]. It is also of interest for those studying self-cleaning surfaces [2]. Fluid pipelines are another area in which drag reduction could result in significant cost benefits; reduced drag on the pipe walls will reduce the amount of pumping needed to move fluids through these systems [3, 4]. In MicroElectroMechanical Systems (MEMS), fluid drag (primarily from surface tension effects) in systems is a dominant force preventing fluids from moving, and thus reducing it is important to allow fluid systems to function on such size scales [5]. Surface tension modifications also open up the possibility of using these surfaces to create low-friction fluid bearings and actuators [6, 7].

In the past, methods for reducing drag by altering the fluid or the boundary layer have been explored, such as by lubricating fluids flowing past surfaces by continuously generating air layers across them [8, 9] or by injecting substances such as polymers into the working fluid to lower effective viscosity and suppress turbulence [10, 11]. These proved to be inefficient due to the need to maintain the effect continuously, as well as impractical in some applications where there is a desire to minimize the effect on the fluid composition.

The exact way that water and surfaces interact has been explored extensively [12, 13, 14, 15]. Hydrophobic (water repelling) surfaces are surfaces that utilize surface geometry and chemical properties in order to minimize wetting. They can occur naturally [16, 17] or be produced artificially [18, 19, 20, 21, 22].

Efforts to create surfaces displaying high hydrophobicity have focused on biomimetics (the duplication of natural systems), mimicking materials that have hydrophobic properties such as lotus leaves, pitcher plant bulbs, bird feathers, or waterstrider legs, and exploring how to enhance these properties [23, 24, 25, 26, 27]. Hydrophobicity is measured in terms of how easily water placed on the surface can move. This can be measured in terms of how small amounts of water, such as droplets, act on a surface, or in bulk fluids, where large areas of the surface are completely submerged. One metric for measuring droplet behavior is rolling angle, the angle to which a surface must be tilted for a droplet to begin rolling across it [28]; samples with vanishingly small rolling angles tend to have high hydrophobicity.

Another is to look at contact angle hysteresis, the difference between the interior angle the drop makes at the point it contacts the surface at the front of the advancing drop and at the back, which measure the energy cost of wetting/dewetting as the drop moves; low hysteresis indicates high hydrophobicity [29]. In bulk fluids, methods of measuring drag reduction focus on directly measuring force on the surface or velocity changes in the flowing fluids [30, 31].

A large amount of work has been focused on duplicating and improving surfaces based on the extremely hydrophobic lotus leaf [32, 17]. Surfaces that achieve high hydrophobicity by utilizing surface tension affects in the manner lotus leaves do are conventionally referred to as Superhydrophobic. Surface tension is used to support the water on top of a roughened surface, entrapping an air layer below the fluid; the lower viscosity of the trapped air allows the main fluid to apparently slip relative to the surface.

More recently, interest has been shown in the hydrophobic properties of the pitcher plant, which uses an oil coating to achieve hydrophobicity [33, 34]. Such surfaces are referred to as Slippery Liquid Infused Porous Surface (SLIPS), as they function by replacing the solid-liquid interface with a liquid-liquid interface; in this case the second liquid is one that is passively held by the underlying surface as opposed to actively injected. The water slides across the oil layer, creating apparent slip relative to the full-contact case. A Superhydrophobic surface whose patterning can also hold fluid can be used as a SLIPS; we utilize this fact to switch our samples between states, allowing for direct comparison between these two mechanisms where the only variable is the presence or absence of the second fluid.

Drag reduction on Superhydrophobic samples has been studied, but not in a consistent fashion; measurements have been taken in a wide variety of ways, including using strips glued to a couette cylinder [30], flowing water through a channel made of Superhydrophobic material [35], and by placing a sample in a Cone & Plate Rheometer [36]. A large amount of study of these surfaces has focused on measuring the contact angle of stationary drops, which is correlated to drag reduction on Superhydrophobic samples [37, 38]. This same correlation has not been shown to hold for SLIPS.

Multiscale patterning combines features on different length scales (for example, nanoscopic hairs on top of microscopic pillars [39]) to enhance the effectiveness of Superhydrophobic materials [40, 41, 42, 43, 44, 45]. Our examination of drag reduction focuses on the effect of the

larger scale features on multiscale surfaces. We utilize a nano-scale roughness coated with a fluoropolymer as our underlying material; such patterning induces Superhydrophobicity on flat surfaces [46, 47, 23]. We produce this roughness on top of concentric millimeter scale grooves, and examine how drag is affected as we vary groove depth and groove angle. We use single point diamond turning to create the grooves, then grow self-ordering Porous Anodized Alumina on top of these to create the roughness, and finally spin on a polymer coating to achieve Superhydrophobicity. These surfaces can be made into SLIPS with the introduction of a second liquid, so we can compare the drag reduction caused by multiscale surface variations in SLIPS as well and directly compare them to the Superhydrophobic behavior. There have been no studies on the effects on drag properties of larger multiscale feature on SLIPS. An examination of the mechanism responsible for Superhydrophobicity shows that these multiscale structures have the potential to produce a SLIPS surface in a Superhydrophobic-like state which we call SuperSLIPS which could further reduce drag; this has not been explored before [48].

Many studies that have been performed focus on the behavior of fluid drops on surfaces. This is not a direct measurement of drag. How well correlated drop behavior is with drag reduction in bulk fluids is not known for all types of surfaces; it may not be well correlated to drag properties in the case of SLIPS or SuperSLIPS at all. By taking measurements in full immersion, we can more directly test drag properties. One method is to examine the force or torque exerted on the surface by flowing water. This gives an average reading of the force exerted by the water on a large area of material. We can compare our modified surfaces to a control sample to quantify the difference in the drag.

Another way of observing the affect of changes to the surface is to measure shear rate in the fluid; this tells us how velocity of the fluid is effected by being in contact with a given surface. These readings are performed using Photon Correlation Spectroscopy (PCS), which measures the light scattered from small particles in the fluid to measure its motion. PCS measurements have been used to probe turbulent two-dimensional flow [49], Brownian motion [50], and have been used to approximately measure three-dimensional flow in a Couette cell and four-roll mill [51]. We study using this method to quantify the drag on these types of surfaces.

The Cone & Plate Rheometer (CPR) is a standard device used for measuring torque on many types of surfaces and/or for measuring shear rate with known surfaces [52, 53]. We use a CPR to perform torque measurements of our surfaces. We also take advantage of the well understood shear rate properties of the device to test the use of PCS for measuring shear rate with unknown surfaces. The mathematical treatments in prior work have either been special cases (2-D) or have been approximate derivations with free parameters, requiring calibration using a reference. We detail a method for performing PCS measurements of the shear rate with no free parameters in 3-D laminar flow in a CPR. We confirm that this method works and perform preliminary measurements on multiscale surfaces.

In Chapter 2, we look at possible surface wetting states and their requirements.

In Chapter 3, we detail our fabrication methods, as well as a brief look at durability of such surfaces.

In Chapter 4, we detail drop testing and static immersion testing of our samples. We also confirm the existence of the SuperSLIPS state.

In Chapter 5, we discuss the theory behind our dynamic drag measurements. We discuss Cone & Plate Rheometers, as well as Photon Correlation Spectroscopy.

In Chapter 6, we detail our full immersion drag measurement system design and construction.

Finally, in Chapter 7, we detail the results of our torque measurements and discuss our preliminary shear rate measurements.

More detailed procedures are given in Appendix A. Other work undertaken but no directly related to the thesis is detailed in Appendix B and Appendix C.

2.0 HYDROPHOBIC SURFACE STATES

Hydrophobicity is the tendency of a surface to repel water; more precisely, it is the tendency for water to wet less strongly to a surface. Efforts to produce surfaces possessing high hydrophobicity have focused on biomimetics: duplicating natural materials that have hydrophobic properties [23, 24, 25]. Duplicating and improving on the extremely hydrophobic lotus leaf has been a long term experimental focus [32, 17]. More recently, interest has been shown in the hydrophobic properties of the pitcher plant, which uses an oil coating to achieve hydrophobicity [33, 34].

Surface hydrophobicity is commonly characterized by examining the contact angle, the interior angle at the point where a liquid/vapor interface meets a solid surface (usually tested by looking at droplets on the surface), and the rolling angle, the angle from horizontal to which a sample must be tipped to before a drop placed on its surface starts rolling [28]. Contact angle hysteresis, which measures the difference between the advancing and receding contact angles when water is in motion across the surface, is also looked at; high contact angle hysteresis indicates that water is resistant to being moved [29].

One method of making a surface hydrophobic is to make the surface rough and chemically functionalize it [15, 14]. The interface characteristics of water in contact with a surface can be changed by structuring, utilizing surface tension effects [46]. Alternatively, it is also possible to produce surfaces with hydrophobic properties by altering the interface state. Methods for altering the fluid or the boundary layer have been explored in the past, for example by utilizing continuously fed air layers [8, 9], but these proved to be inefficient due to the need to continuously maintain the effect. Rather than actively altering the boundary layer, if the surface can passively retain a second fluid, water can be made to flow across it instead of the surface itself, resulting in increased hydrophobicity without active maintenance of the altered interface.

Water can be in several possible wetting states with respect to a surface [54, 55]. We look at three known states, as well as one additional state which has not previously been observed.

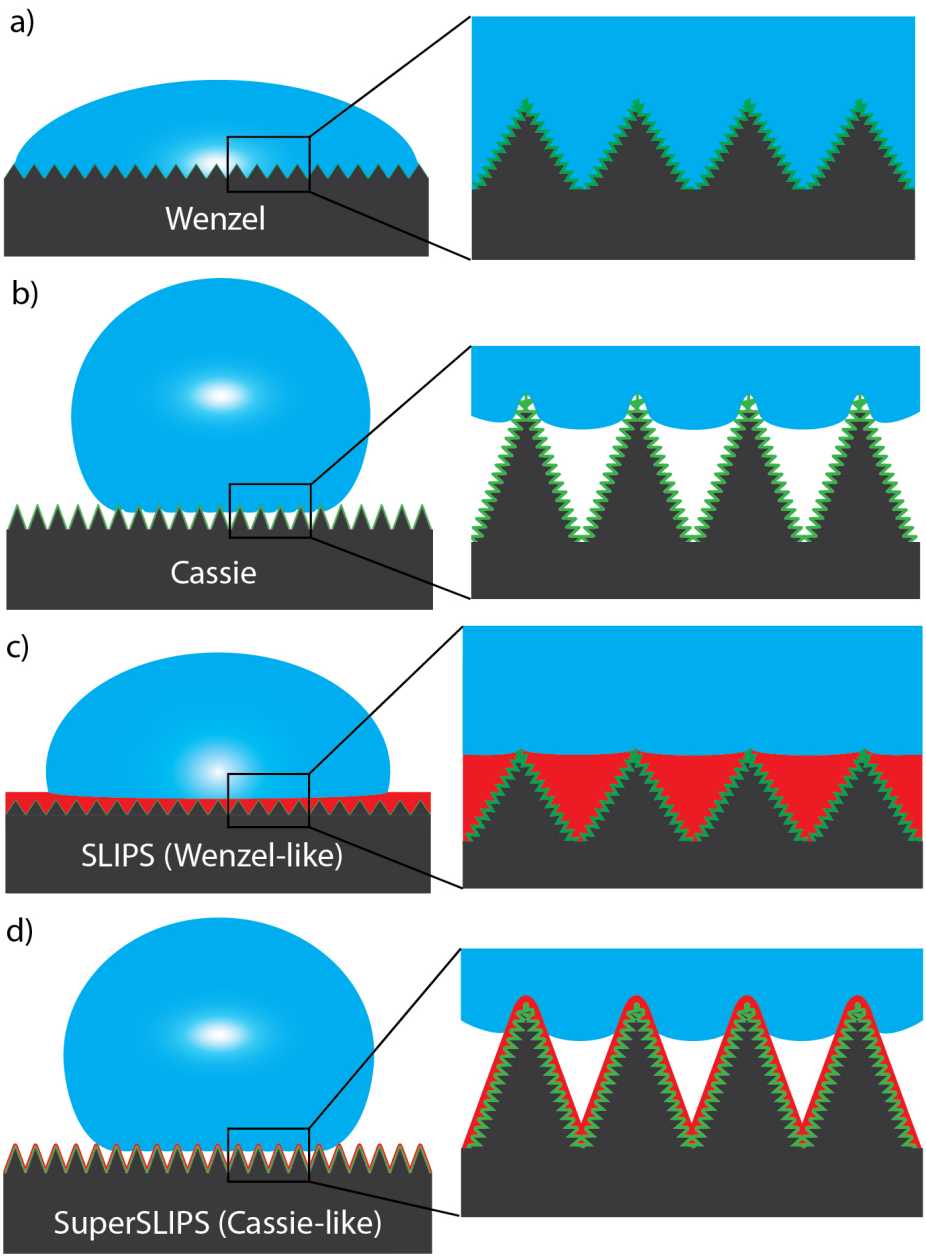

Figure 1: Diagram of possible wetting stat on multiscale surfaces. a) Wenzel: fully wetted, b) Cassie-Baxter: a layer of air separates most of the water from the surface, c) SLIPS: a layer of an immiscible liquid separates the water from the surface, d) SuperSLIPS: a layer of air separates most of the water from the surface, which is coated with a second liquid.

2.1 SURFACE WETTING STATES

2.1.1 The Wenzel State

If water fully wets the surface, it is in the Wenzel state (Fig. 1a) [56]. In this state, a drop of water placed on the surface may have a range of contact angles, but has high contact angle hysteresis and is resistant to being moved. This is the most conventional form of surface behavior, where the no-slip condition is applied at the liquid/solid interface and there is no need to worry about complicated dynamics. These surfaces are extensively studied and understood, and are the control surface in all our measurements [57, 58].

2.1.2 The Cassie-Baxter State

A surface that utilizes surface tension effects to minimize fluid drag, based on the lotus leaf, is in the Cassie-Baxter state (Fig. 1b) [59]. If a surface has microscale structure, and if the contact angle of the base material (or a coating thereof) and the surface geometry of these features meets certain requirements, water can be supported on the structure by surface tension such that it is mostly non-contacting, with a layer of air separating most of the liquid from direct contact with the solid surface. Surfaces which support a Cassie-Baxter state typically feature high contact angles, which in this case correlates with low contact angle hysteresis, so water slides off easily. If such a surface possessed a contact angle above 150°, which corresponds to very high hydrophobicity, it is by convention referred to as 'Superhydrophobic' [54]. Drops on this type of material will not spread, remaining nearly spherical, and will instead roll off without wetting [60, 61]. These surfaces are effective, but vulnerable to failure; since the effect is dependent on the structuring, physical damage can reduce or negate the surfaces' effectiveness. There are also known issues with biofouling, where the growth of biological material on the surface impairs or negates the drag reducing properties [62].

The Cassie-Baxter state is a consequence of surface tension interactions. With the right geometry, the vertical component of the surface tension, acting at the interface, holds up the liquid, so it is mostly riding on air. This can greatly reduce drag, as the majority of the

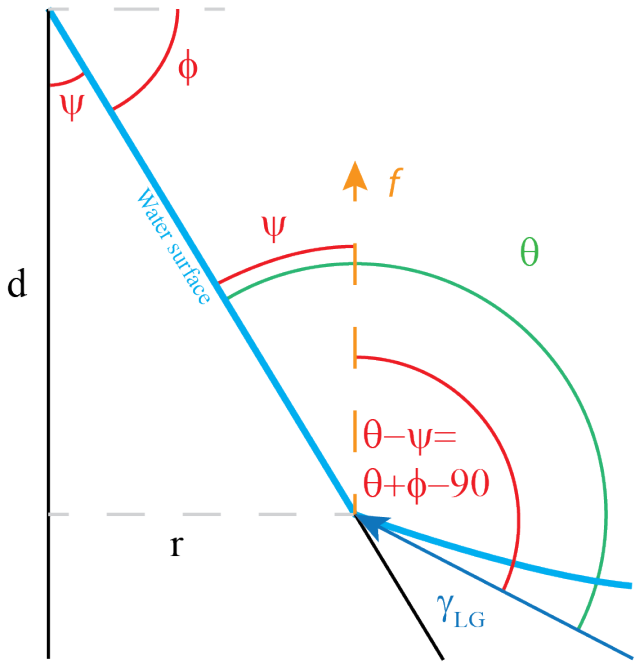

Figure 2: Geometry of forces in Cassie hydrophobicity on a sloped surface, looking at the response of the line directly *next to* the contact line on the fluid surface. d is the distance from the top of the slope to the interface, ψ is the slope half-angle, ϕ is the slope angle from the horizontal, θ is the contact angle, and γ_{LG} is the Liquid-Gas surface tension.

liquid interface is then in contact with air, rather than a solid surface to which it can wet. Drag forces between water and air are lower than between water and most solid surfaces, and the viscosity of air is far lower than that of water [59].

We consider the fluid interaction with a sloped surface. Looking at Fig. 2, we can write the vertical force per unit length f acting on the water/slope interface as

$$f = \gamma_{LG} \sin(\theta - \psi - 90^\circ) = -\gamma_{LG} \cos(\theta - \psi) = -\gamma_{LG} \sin(\theta + \phi) \tag{2.1}$$

where γ_{LG} is the Liquid-Gas surface tension, θ is the contact angle, ψ is the slope half-angle, and ϕ is the slope angle from the horizontal. We see that this prevents the interface from moving down the slope, allowing for the lower surface of the water to rest on the

trapped air pocket [46, 43]. Note that the geometry in Fig. 2 is for the line immediately *next to* the contact line on the fluid surface; using Newton's third law allows us to calculate the vertical force without needing to directly consider the surface tension from the other interfaces. Eq. 2.1 can be used as a criterion to determine how steeply sloped a surface needs to be to enter the Cassie-Baxter state once the contact angle has been measured on a flat surface.

We may construct our surface out of an array of microscopic spikes. Assuming that the spikes are steep and numerous enough, each of them will contribute to holding water placed on them out of the spaces between them, resulting in a high fraction of the water being in contact with air rather than the underlying surface. This is similar to the classic "bed of nails" demonstration, spreading the weight of the water across a large number of small supports without breaking the surface.

A force can be obtained by integrating around a closed line of contact. If we take the tips of the microscopic spikes to be approximately circular, we can integrate Eq. 2.1 to get the total upward force per spike $F_s = -\gamma_{LG} 2\pi d \tan(\psi) \sin(\theta + \phi)$, which shows a Hooke's law restoring force upward characterized by the distance down the spike the water contact line has descended.

2.1.3 SLIPS

Instead of depending on surface tension effects, we can modify the effective surface properties if the surface can be hold in place a second liquid which is immiscible with water. If the second liquid wets the underlying surface, and the contact angle of the second liquid on the surface is much lower than the contact angle of water, the second liquid will tend to coat the surface and displace water and air from between surface features. The water will then move along the surface of the second liquid while barely contacting any projecting features of the solid surface(Fig. 1c). This kind of hybrid liquid-solid surface is known as a Slippery Liquid Infused Porous Surface (SLIPS); an example of this kind of surface is the inside of a pitcher plant [33].

If the immiscible liquid is considered as part of the surface, then a water drop on a SLIPS

can be considered to be in a Wenzel-like state, in complete contact with the immiscible liquid or solid surface. However, it does not wet the surface, so the only resistance to motion is the viscous contact between the fluids and contact with the occasional projecting feature [63]. These surfaces tend to have low contact angle hysteresis, but typically have lower contact angles than Supherhydrophobic surfaces; the mechanism lowering the drag is that the water is sliding along the immiscible fluid without wetting, rather than being held out of contact with the surface by surface tension effects. Compared to Superhydrophobic surfaces, SLIPS are less vulnerable to damage, as the liquid can flow to fill in damage without radically changing the interface characteristics; the solid surface simply acts to hold the immiscible liquid layer in place [34, 64]. In addition to being of interest for their hydrophobic properties, they are also of great interest in antibiofouling, as the second liquid can be selected to prevent microorganism growth [65].

If the material is capable of retaining the second liquid, we can convert a structured Superhydrophobic surface into a SLIPS by applying the immiscible liquid to it. For certain immiscible liquids, a Superhydrophobic surface composed of microscopic spikes can be made into a SLIPS. In this case, the immiscible liquid is held in between the microscopic spikes and, when present in sufficient thickness, inside any macroscale features.

2.1.4 Multiscale Cassie-Baxter Behavior

Eq. 2.1 considers a sloped surface, but does not impose a scale requirement. If a Superhydrophobic material can be made in such a way that it retains its properties regardless of the macroscale shape of the underlying surface, there is nothing preventing us from trying to induce Cassie-Baxter behavior with respect to these larger features simultaneously.

The vertical force due to surface tension with respect to contact with the larger scale structure is simply

$$F_z \propto -\gamma_{LG} \sin(\theta' + \phi') \tag{2.2}$$

where ϕ' is the angle of the slope of the larger-scale structure measured from the horizontal near the tip, and θ' is the apparent contact angle of water on the surface material itself. We see that the requirement for a positive force is $\theta' + \phi' > 180°$. Since θ' is the contact angle for

the flat material surface, all that is required to generate a Cassie-Baxter state when larger grooved features are added is to make the groove slope adequately steep. For our experiments, we produce millimeter scale grooves in our surfaces to test multiscale behavior. We can do this using Superhydrophobic material, which allows us to create multiscale Cassie-Baxter surfaces.

2.1.5 SuperSLIPS

We note critically that the preceding considerations only depend on the contact angle of the surface. The particulars of the interface, such as material composition, are not important. Thus, if we measure the contact angle of our SLIPS material (made by applying an immiscible fluid to our Superhydrophobic material), there is no reason to believe that a SLIPS with sufficiently steep grooves cannot still achieve a Cassie-Baxter state relative to the larger grooves, provided $\theta' > 90°$ for the SLIPS material itself. In this hybrid state, the surface consists of micro-scale spikes filled with immiscible liquid while the grooves are empty of liquid and can support an air layer, theoretically providing the advantages of both types of surfaces (Fig. 1d).

We call these SuperSLIPS, indicating that SLIPS properties are enhanced by additional surface structure, similar to how structured hydrophobic surfaces are enhanced to become Superhydrophobic surfaces which support a Cassie-Baxter state. SuperSLIPS could combine the best features of Superhydrophobic surfaces (hydrodynamic drag reduction) and SLIPS (self-repair and biofouling resistance), which are otherwise difficult to obtain simultaneously [48]. The oil-coated feathers on some preening birds, such as those of penguins, which have been shown to retain significant air layers while underwater [66], may be natural examples of SuperSLIPS, and indicate that these surfaces could be highly desirable for underwater applications. These surfaces have not been produced or examined prior to the work in this thesis.

3.0 MATERIAL FABRICATION

There are a wide variety of methods for making Superhydrophobic surfaces. These surfaces are either made out of inherently hydrophobic materials (such a fluoropolymers) or are coated to make them hydrophobic. Common substrates have regular structure (such as spikes or posts) [40, 46, 24, 39, 67], porous structure [18, 19, 21] or unordered roughening [32, 22, 23]. Current methods for the production of such surfaces are often difficult, requiring multiple processing steps and complex, sometimes layered, materials [57]. Many of these surfaces are prone to degradation of their hydrophobic properties, in particular when immersed in liquids for extended periods [47, 18].

We have access to a single point diamond turning (SPDT) machine, which allows us to cut materials to less than 10 nm surface roughness [68]; we can also cut grooves to high precision even down to μm scale. Not all materials are compatible, but aluminum is one that can be easily cut using diamond turning. Aluminum oxide (alumina) coatings grown via anodization form hexagonally arranged pores if produced within current, temperature, and voltage limits that depend on the anodizing acid used; in this case it is referred to as Porous Anodized Alumina (PAA) [69]. We can convert this array of vertical pores into a spiked surface by alternating anodizing growth with chemical etching steps, as illustrated in Fig. 3. The PAA growth process is conformal to the aluminum surface, so it can be grown as easily on a grooved surface as a flat one. If we coat the PAA surface with a hydrophobic material, we can create samples that can be in the Superhydrophobic and either the SLIPS, or SuperSLIPS state, depending on the geometry of the underlying sample and whether it is coated with an immiscible liquid or not.

3.1 FABRICATION

3.1.1 Anodization

We utilize 99.999% pure aluminum discs for our substrates. For smaller test pieces, we used 50 mm diameter, 0.5 mm thick foil (Goodfellow AL000650) or 50 mm diameter 0.25 in thick aluminum disks, while for our primary test articles we used 4 in diameter, 0.25 in thick

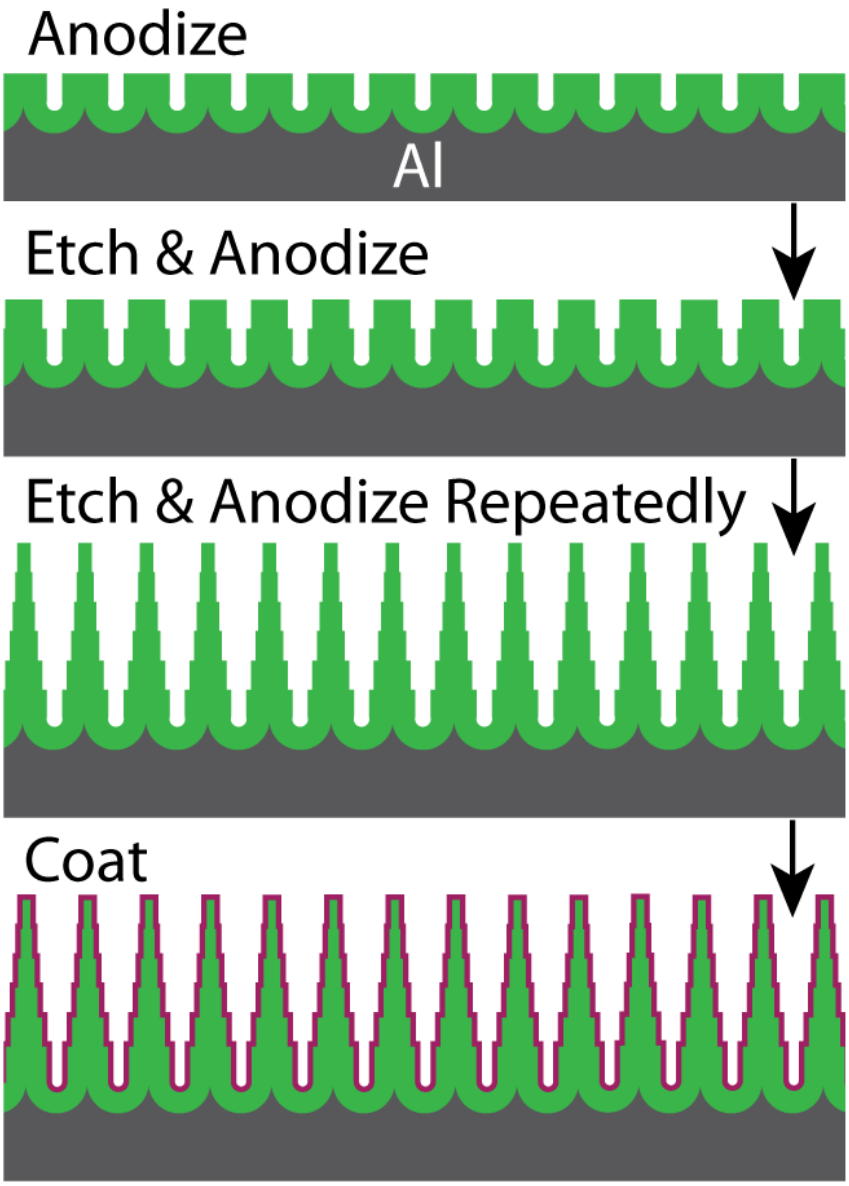

Figure 3: Illustration of anodizing and etching process. We grow, then etch back, then grow. Repeating this cycle allows us to create surface roughness with high aspect ratio from the straight vertical pores produced by anodization.

aluminum disks (0.25 in thick disks were originally manufactured as sputtering targets). If we wish to create multiscale surfaces, we can cut concentric circular grooves in the aluminum after cutting the surface flat, using dead sharp diamond tools with varying tip angles. The grooves cannot be cut all the way to the center of the disc due to tool clearance limitations. SPDT removes native oxide from our substrate, leaving a pure aluminum surface for anodization.

Since we observed that a thick native oxide layer interferes with further processing, we quickly place our samples in an evacuated bell jar after cutting so the diamond turned surface experiences minimal regrowth before anodization.

Anodization is performed in 0.1175 molar citric acid (in water) at 320 V, at a current density limit of 0.051 $\frac{A}{m^2}$ and a temperature of 18-20°C, which produces 750 nm spike separation [69]. Etching is performed in 2% w/w (in water) tetramethylammonium hydroxide (TMAH) at 18°C [70]. The older oxide is etched back further with each etching step, while newer material is grown underneath at each anodization step, creating a stepped spike array. The thickness of the oxide and aspect ratio of the spikes are easily controlled by choosing the total charge passed through the sample during anodization and the etching times, within certain limits. A similar technique is used to create molds for anti-reflection coatings, with different choices of chemical and voltage, has been described in detail [71, 72]. The growth of PAA is conformal; the pores are always perpendicular to the surface regardless of shape. For surfaces that have additional cut features in the aluminum, we are careful to maintain a constant thickness in each anodization step by increasing the current and total charge passed through the surface by the ratio of the surface area compared to a flat disc so that the current density if maintained; voltage is not changed as this determines pore spacing. An example of our anodized surface is shown in cross section in Fig. 4. A step-by-step anodization procedure can be found in Appendix A.1.3.

Spiked PAA surfaces are more hydrophilic (wet more strongly) than flat aluminum [73]. In order to achieve the Cassie-Baxter state, the surface needs to be altered to increase the contact angle of the sloped sides of the spikes. We utilize a surface coating of Solvey Plastics Hyflon AD-60, a hydrophobic fluoropolymer [40] (similar to Teflon AF [74]). Application of this material to our spiked PAA surface leaves the surface Surperhydrophobic.

It was necessary to try a variety of different methods of applying this coating, including different thermal cycles and a variety of adhesion promoters, in order to achieve a durable coating that could withstand testing without degrading.

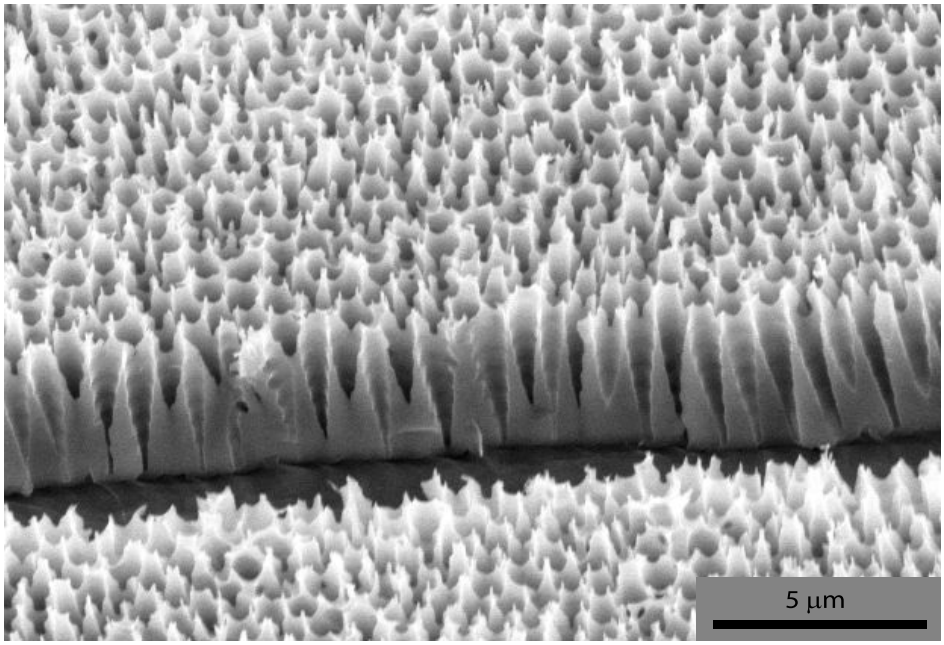

Figure 4: SEM image of a spiked PAA surface in cross section at 20 degrees inclination, thickness 4 μm. Note the visible steps made by alternation of 8 anodization and 7 etching steps.

3.1.2 Coating Durability Testing

3.1.2.1 Continuous Immersion We examined the use of underlying adhesion promoters, as well as multiple coatings of Hyflon, to find the optimal combination for long term water immersion. A thin foil disc was prepared with our PAA surface. The foil disc was cut with a knife blade into smaller pieces, so there would be no variation in the underlying structure between our samples. All samples were cleaned with isopropyl alcohol and baked at 200°C for 90 minutes to drive off any remaining surface liquids prior to being coated.

Two types of self assembled mono-layers (SAM) were tested: (tridecafluoro 1,1,2,2, tetrahydrooctyl) trichlorosilane (TTTS), which is also used in the production of hydropho-

bic surfaces [19, 75], and ethyltrichlorosilane (ETS) [76]. Hexamethyldisilazane (HMDS), a common adhesion promoter with hydrophobic properties [77, 21], was also studied. Coating combinations we examined are shown in table 1.

F0	Single Layer Hyflon
F1	Double Layer Hyflon
F2	ETS + Hyflon
F3	TTTS
F4	TTTS + Hyflon
F5	HMDS + Hyflon

Table 1: List of coatings tested.

Sample F2 was coated by submerging it for 30 minutes in a solution of 9.9 mL Hexane and 0.1 mL of ETS, F3 and F4 were treated likewise with 0.1 ml of TTTS. F0 and F1 were submerged in 10 mL Hexane for the same duration to ensure minimal variation in processing history. F0-F4 were then baked for 15 minutes at 150°C, and ultrasonically cleaned in isopropanol individually to remove residue, blown dry with compressed air, and then all but F3 were spin coated at 1000 RPM with 2% w/w Hyflon in 3M Fluorinert FC-40.

F5 was taken directly from the initial bake, allowed to cool, and then spin coated with propylene glycol monomethyl ether acetate (PGMEA):HMDS in 4:1 solution at 4000 RPM. This was followed immediately by a coating of the Hyflon solution at 1000 RPM (without being allowed to dry between coatings).

Following individual coating, all samples were baked together at 75°C for 30 minutes, then ramped to 150°C (heating the Hyflon above its glass transition temperature) and baked for 3 hours. Samples were allowed to cool, then a second coating of Hyflon was applied to F1 and all samples were subjected to the same bake cycle again to eliminate thermal history as a variable.

At the conclusion of fabrication, samples were photographed in profile with a drop of deionized water (held in place using a needle suspended above the surface) to determine static contact angles. Static contact angles of $161 \pm 1^{\circ}$ were seen for all samples, as shown in

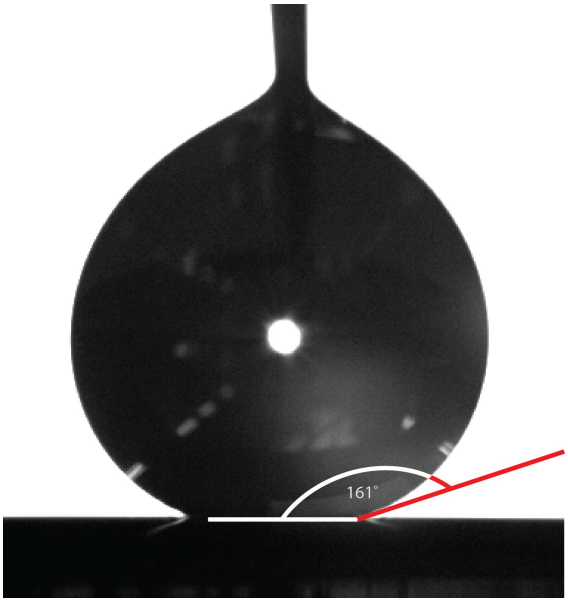

Figure 5: Profile image showing contact angle of a drop of water on the material before full immersion in water was undertaken. Drop is held in place with a needle suspended above the surface.

Fig. 5, indicating that they were initially superhydrophobic and very uniform in character. Numerical fitting was used to model the outline of the drops and determine contact angles.

To test long term coating durability in water, samples were immersed for an extended period and periodically extracted for testing (samples were allowed to air dry if any water adhered). The rolling angle was measured by applying a series of 15 μL and 30 μL drops at 10 different locations on each sample, then tilting the sample until the drop began to roll and reading from an inclinometer. These readings were taken at multiple points across the surface of the samples so that a representative sample of the surface was evaluated in the course of a measurement series; this ensured that if any small defects were included in the data, they did not dominate our evaluation. A reading of 90° was recorded for any drop that remained adhered until or past vertical inclination. Measurements were repeated over a period of 900 hours(37.5 days), taken at no longer than 48 hour intervals (see Fig. 6).

Initial rolling angles for all samples were low. F0 began with an average rolling angle of

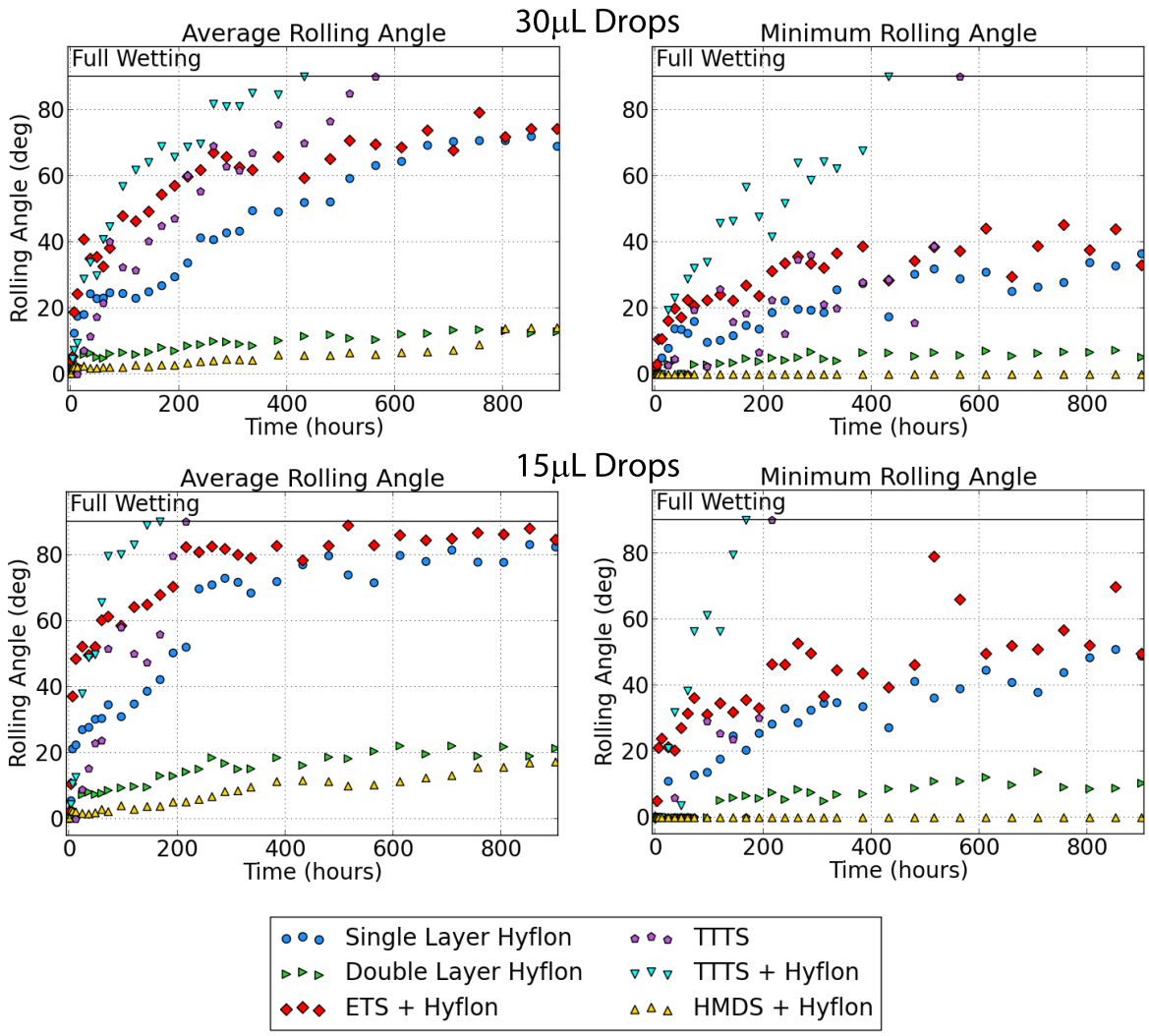

Figure 6: Rolling angle as a function of time. A reading of 90° indicates the drop adhered up to or past vertical tilt.

0.8° for 30 μL drops (0.2° for 15 μL drops), F1 with an average of 0.0° (0.4°), F2 with an average of 4.8° (2.2°), F3 with an average of 0.2° (0.1°), F4 with an average of 0.05° (0.1°), and F5 with an average of 0.2° (0.4°). The minimum rolling angle observed on each sample except for F2 was 0°; F2 began with a minimum rolling angle of 1.9° (0.0°).

Fig. 6 shows complete data for all testing using both 30 μL and 15 μL drops. F5 (HMDS+Hyflon) performed the best of all samples, with a final rolling angle at an average

of 14° (17°) by the end of testing. It was also the only sample that still had any areas with a rolling angle of 0.0° at the conclusion of the test. The increase in average rolling angle was extremely gradual, and remained below or even with the next best sample throughout the test.

The average contact angle for F1 (double Hyflon) was 7° after 24 hours, and reached 12° (21°) after 900 hours, indicating very good stability as well, with the most hydrophobic areas remaining having a rolling angle of 10° (13°).

By comparison, F0 (single Hyflon) and F2 (ETS+Hyflon) both showed a final average rolling angle of 70° (83°) and a final minimum at 35° (50°), with F2 increasing quickly and then stabilizing, while F0 gradually increased to this point.

F3 (TTTS) and F4 (TTTS+Hyflon) both completely failed after 564 and 432 hours (216 and 168 hours), respectively, reaching a rolling angle of 90° across the entire surface. F4 began failing immediately, while F3 performed well for the first 12 hours, maintaining a near zero contact angle for this time, before failing at a rate similar to F4.

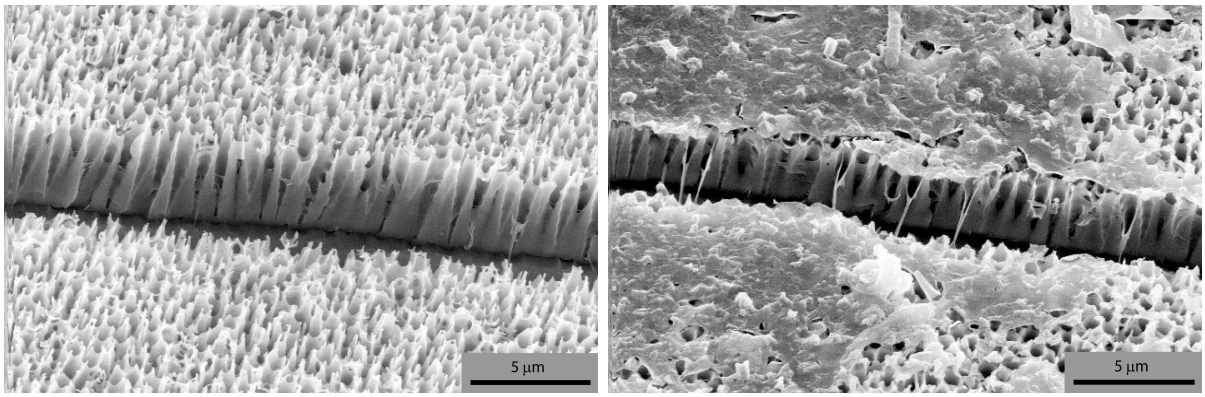

(a) Normal Hyflon Coating

(b) Hyflon Coating Failure

Figure 7: SEM images of sample, taken at a 20° angle after testing and cracked to show profile.

Hyflon sample coatings are highly conformal in most areas, as can be seen from a comparison of a coated (Fig. 7(a)) and uncoated (Fig. 4) surface. Evidence that the coating is present at all is only visible where small strings of polymer can be seen stretching across the crack made in the surface oxide to allow for a profile view.

Loss of hydrophobicity mostly began at one or more edges and proceeded inward, with all samples achieving at least a small area of full wetting before the conclusion of the test. The coating was uneven at the edges, possibly due to the non-circular shape of the samples and/or the transition from PAA to bare aluminum at the outer edge of the anodized region. The corners where a knife-cut edge and the edge of the anodized region met appeared to be the most vulnerable. The edge of the anodized area transitioning to bare aluminum is visibly different from the main body of the anodization, and was avoided in testing. As shown in Fig. 7(b), taken after testing was completed, the coating can be clearly seen to be on top of the surface, rather than coating it conformally. However, all the cut edges were prone to losing hydrophobicity, possibly due to damage to the substrate patterning resulting from being cut from the original disc.

It is possible that delamination of the coating occurred due to the cut edges and the anodization border allowing water underneath the coating. Note that point defects away from the edges, though they did become more hydrophilic with continued immersion, did not tend to expand. This indicates that this is an issue with the edge itself.

A scratch accidentally occurred on F5 during handling. While this area showed a rolling angle greater than average, it was still able to maintain a rolling angle of $<15^\circ$ ($<30^\circ$). This demonstrates a good resistance to macroscopic physical damage as well, but was not further investigated at this time.

Both double layer Hyflon and Hyflon with HMDS displayed similar performance. The second layer of Hylfon may have filled in gaps in the coating of single layered samples, allowing it to retain its properties and preventing water from undercutting the surface bonding. The HMDS, being both an adhesion promoter and itself a hydrophobizing agent, may have acted to both hold down the single layer of hylfon and similarly fill in gaps. The combination of two different hydrophobizing mechanisms may account for why completely superhydrophobic areas were able to survive.

ETS and TTTS were both unable to achieve such effects. In the case of TTTS, performance was degraded as compared to Hyflon on its own. ETS had a short term deleterious effect, but in the long term performance was the same as with single layer Hyflon.

All of these tests were performed on a single sample, so the effects of varying pore spacing

and aspect ratio of the features of the PAA are not considered, and may increase or decrease the durability and/or contact angle.

3.1.2.2 Transient Wetting Testing Long term nearly continuous immersion was tested above. However, it was observed that these surfaces degenerated more rapidly with continual application and removal of liquid. It was thus concluded that the coating, in addition to having a long term immersion limit, was also subject to a limit on the number of wet-dewet cycles that could be endured.

Having selected HMDS+Hylflon coatings as the best performing based on the previous tests, new samples were prepared and subjected to a variety of prebake methods and final bake temperatures. These samples were placed, slightly tilted, beneath a burette, positioned so the water would stream onto the sample and be held in place by the burette tip until pulled off by gravity acting on the water drop. This allowed the full surface to be subjected to repeated wet-dewet cycles. The samples would be tested for rolling angle after a set amount of water had been flowed across them to determine durability.

The primary parameter tested was the final bake temperature for curing the Hyflon. The melting point for Hyflon-AF powder is not known, but bulk hyflon melting point is 280-310°.

Bake Temp	Final Rolling Angle
150° C	22.8°
200° C	20.9°
250° C	17.2°
300° C	14.2°
310° C	18.2°

Table 2: Curing temperatures tested. Rolling angles are after 2 purretes (500ml) of water dripped over sample

Best results were achieved by increasing the baking temperature to 300° C; further increase in bake temperature rapidly worsened the outcomes, indicating the beginning of hyflon breakdown. A further test showed that 30 min was a sufficient baking time at this higher

temperature. Step-by-step coating procedures can be found in Appendix A.1.5.

The initial prebake was also tested. While oxygen plasma cleaning for 10 min at 50 W was found to be superior to baking for 90 min at 200° C, this process could only be applied to 2 in diameter samples, as the load lock for our vacuum chambers cannot accept samples above 3 in diameter. For larger samples, we had to continue to use the 90 min, 200° C prebake. Step-by-step pre-baking procedures can be found in Appendix A.1.2.

The full sample preparation and handling procedures used for samples in the remainder of this thesis can be found in Appendix A.1.

4.0 STATIC DROPLET MEASUREMENTS & EXPERIMENTAL VERIFICATION OF SUPERSLIPS

Using our fabrication process (see Chapter 3), we can theoretically create samples capable of being in either the Cassie-Baxter, SLIPS, or SuperSLPIS states, depending on the geometry and whether they have an immiscible liquid coating. Before we can proceed with bulk fluid measurements, it is necessary that we confirm that this is true. In particular, the SuperSLIPS states had not been observed before work in this thesis, and so it was of paramount importance to confirm that it actually existed. We test the behavior of water drops on these surfaces to obtain an initial understanding of their properties.

4.1 MULTISCALE SAMPLES

During durability testing (chapter 3.1.2), we established that our spiked PAA surfaces were capable of producing contact angles on the order of 160°, therefore based on Eq. 2.2, concentric grooves with an angle from the horizontal in excess of 20° will experience multiscale Superhydrophobic behavior. Using thick 2 in diameter aluminum discs, we produced a flat Superhydrophobic sample, and grooved Superhydrophobic samples with $\phi' = 30°$, 45°, 60° and 75° wall slopes, with the groove spacing fixed at 0.25 mm for all angles and cut deeply enough that they meet to form a series of sharp ridges. The grooves were not cut all the way to the center of the disc due to tool clearance limitations. Anodization was performed such that PAA thickness was maintained by compensating for the difference in surface area caused by grooving, see App. A.1.3. We do not vary the characteristics of our microscopic spikes, as this has been explored before.

We make our samples into SLIPS or SuperSLIPS by coating with a layer of polydimethylsiloxane (silicone) oil (5 cSt, Sigma-Aldrich 317667) by spin coating. Note that the viscosity of this fluid is greater than water. A water drop placed on our ungrooved SLIPS material with a thin oil layer (spun off at 10,000 RPM) has a contact angle of 111°. Combined with Eq. 2.2, this predicts that SuperSLIPS will result if the slope of the larger-scale features is greater than 69°. This can only occur if the oil layer is thin; otherwise the oil layer will fill in the larger scale features and produce a standard SLIPS.

We performed all measurements of samples in the Superhydrophobic state before we

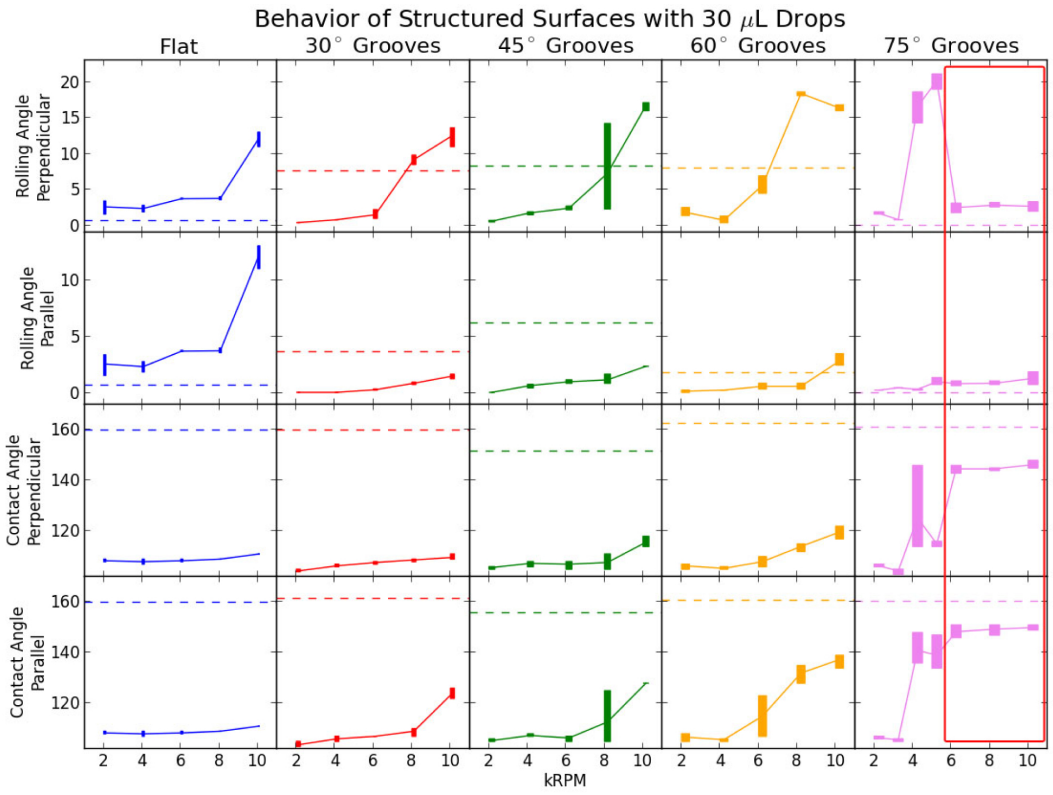

Figure 8: Data for rolling and contact angles as a function of oil layer thickness (quantified by spin-coating speed in kRPM). Values for surfaces without any oil are indicated by dashed lines. The apparent super-slippery regime is boxed.

coated these same samples with oil, to avoid concerns about contamination by or incomplete removal of the oil. We varied the thickness of the oil layer on the surface by applying 1 mL of oil to each sample and then spinning off the excess oil at various spin speeds (for 25 s) to create a uniform coating. We tested in a thickness range from 2,000 RPM to 10,000 RPM.

As can be seen from Fig. 8, the behavior can be broken into that for thinner layers and that for thicker layers, so we carefully examine one of each. The layer created by spinning at 2,000 RPM was examined to asses the behavior of a thick coating, while to look at the behavior of a thin layer we used samples spun at 10,000 RPM.

The results are summarized in Fig. 9. Several trends in the data are immediately visible. First, oil-free samples had the highest contact angles, as expected for Superhydrophobic

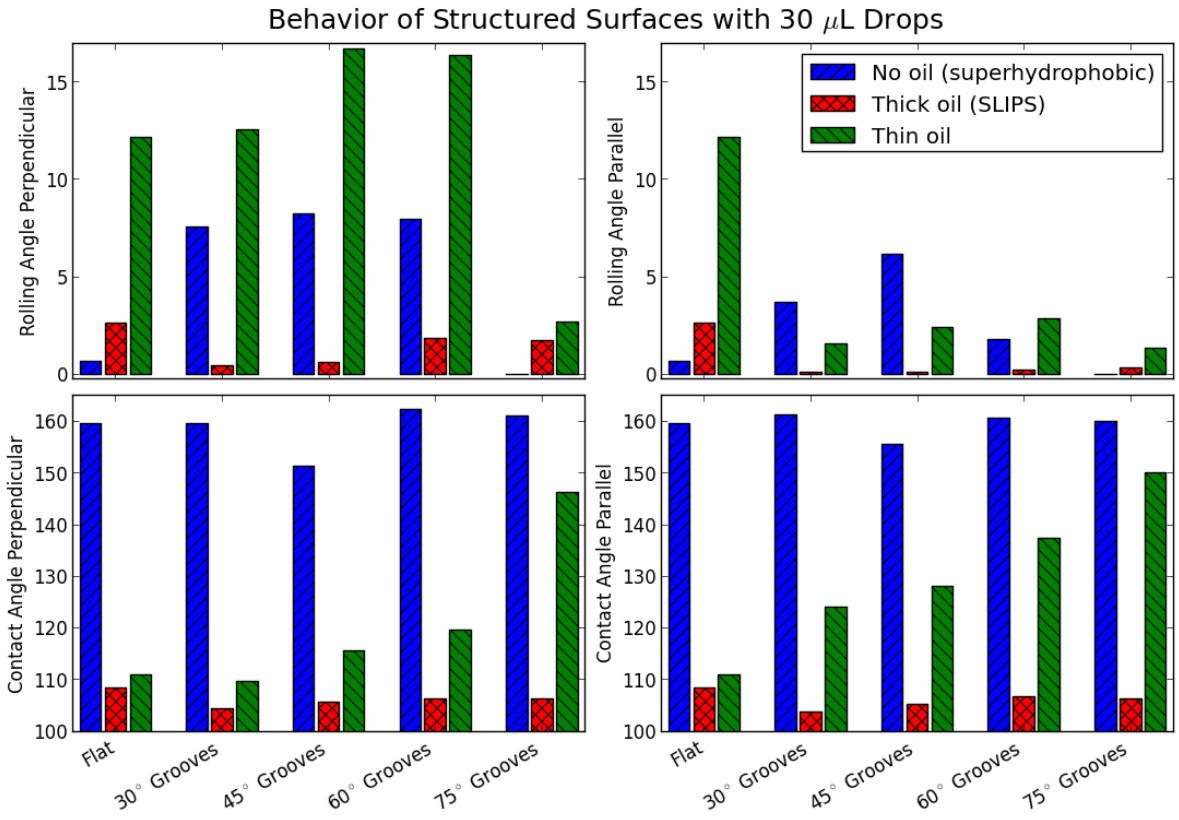

Figure 9: Rolling and contact angles of water on grooved and structured hydrophobic surfaces with no oil coating, a thick oil coating spun off at 2,000 RPM or a thin oil coating spun off at 10,000 RPM. Note the decrease in perpendicular rolling angle and increase in the perpendicular contact angle at high groove angles with a thin oil layer, which may indicate a SuperSLIPS state.

materials. Samples with a thick oil layer had the lowest contact angles and often the lowest rolling angles, which is expected for SLIPS, where the oil effectively fills in the grooves, creating a smooth surface for the drops to skate along. Contact angles for oil-free samples and samples with thick oil layers did not change significantly with variations in groove angle. Samples with thin oil layers had the highest rolling angles for almost all groove angles. In this case, the oil did not fill the grooves, and at most groove angles the water drop was pulled into the grooves as there was nothing preventing the formation of the Wenzel-like state with

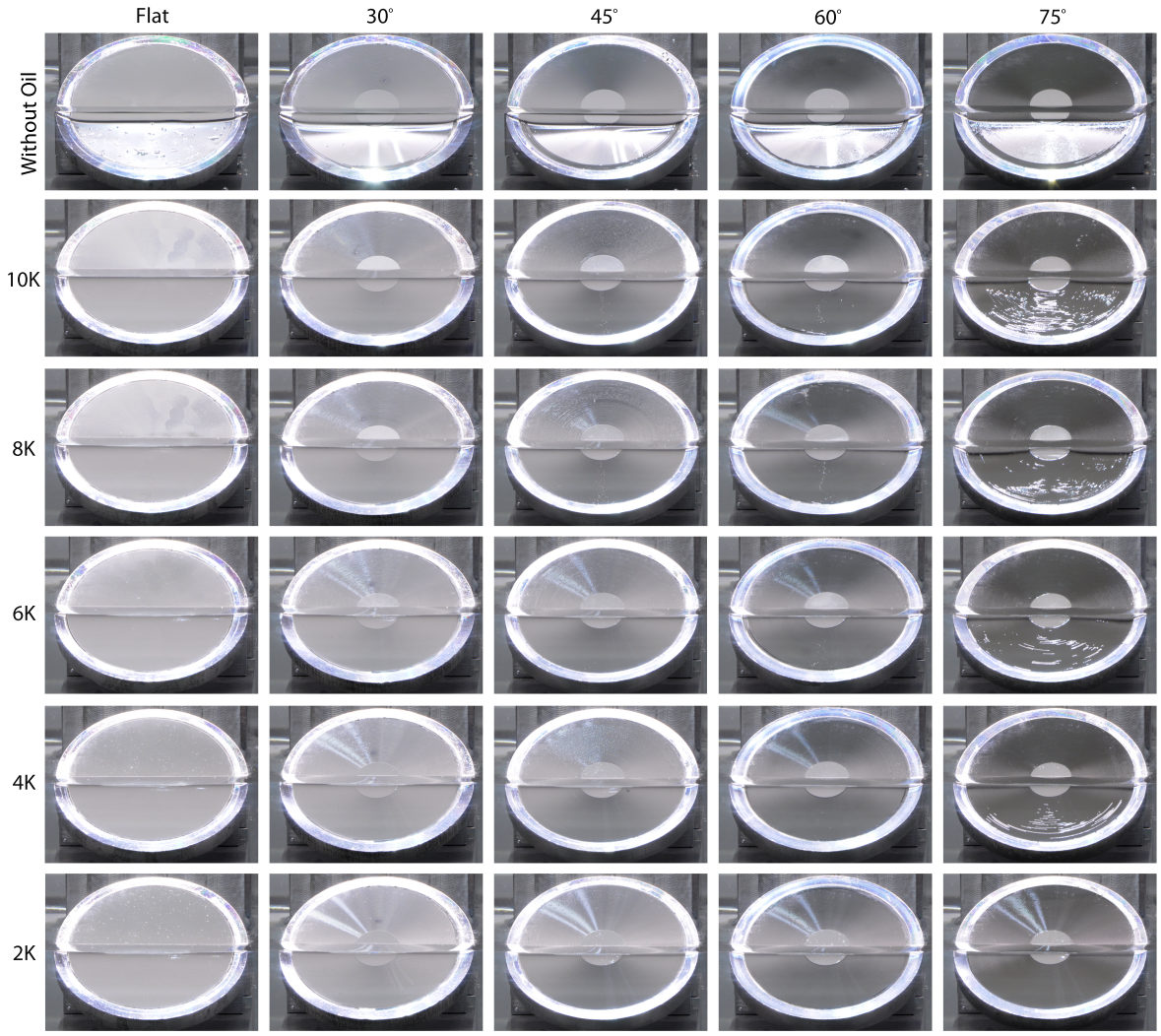

Figure 10: Samples half-submerged in water. Note the high reflectivity below the waterline when an air layer is present, as on all samples without oil. More of the surface of the 75°-grooved sample with thinner oil layers is highly reflective than is visible in the photograph, but the visibly reflective area depends on the viewing angle. All photographs were taken under identical conditions; there is a change in reflectivity with groove angle.

the oil in the microscopic spikes, making it more difficult for drops to roll over the ridges. This is expected from previous experiments on multiscale SLIPS [64].

Samples with 75° grooves showed comparatively anomalous behavior. The perpendicular

rolling angle was dramatically lower compared to other groove angles and the flat surface, near that of a flat surface with a thick oil layer. The parallel rolling angle also decreased to below that of a flat surface with a thick oil layer, and the contact angles both increased to nearly the oil-free values. The perpendicular contact angle, in particular, was much higher than with other groove angles. This confirms the hypothesized change in wetting state above 69° groove angles.

4.2 CONFIRMATION OF THE EXISTENCE OF SUPERSLIPS

One interpretation of the behavior of water drops on samples with 75° grooves and a thin oil layer is that the water was suspended from the oil-coated ridges with air filling the grooves, as in Fig. 1d. We observed the samples submerged in water to check for evidence of SuperSLIPS, shown in Fig. 10. Samples without oil displayed a highly reflective surface underwater, due to total internal reflection of light off the Cassie state air layer on the surface. The strong reflection disappeared with the addition of a thick oil layer, indicating the formation of a SLIPS with no air layer. However, for a thin oil layer and 75° grooves, part of the submerged surface was highly reflective, supporting the prediction that a Cassie-like SuperSLIPS state, having both an oil-coated surface and an air layer, existed on the surface. The difference in reflectivity suggests that the air layer was thinner or less complete than with the oil-free surfaces. Note that more area on this surface was highly reflective than is visible in Fig. 10, but due to the grooves, the entire air layer cannot be photographed from a single angle.

For additional evidence of the wetting state, we compared the behavior of 10 μL droplets of water resting on 45° and 75° samples, both with thin oil layers. It is clear (see Fig. 11) that on the 45° sample, the droplet is in complete contact with the surface in a Wenzel-like state. However, the droplet is clearly suspended near the tips of the grooves on the 75° sample, confirming that the behavior we were seeing was an indication of the Cassie-Baxter-like SuperSLIPS.

These results demonstrate that the addition of grooves to immiscible liquid coated surfaces modifies the behavior of water on those surfaces, and in particular, if the features

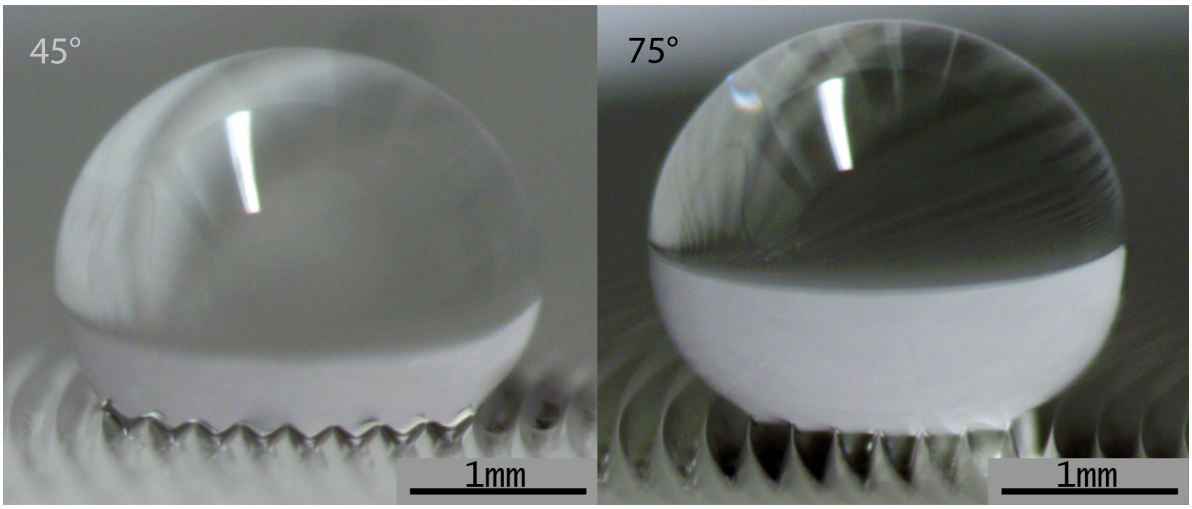

Figure 11: Photographs of the profile of a 10 μL drop of water on 45° and 75° grooved samples with a thin oil layer. The drop on the 45° sample is fully wetting to the oil (Wenzel-like), while the drop on the 75° sample is suspended over the air-filled grooves (SuperSLIPS).

have sufficiently steep slope and the oil layer does not fill the macroscopic features, there is evidence of SuperSLIPS. The results suggest that this combination of features is a result of having an immiscible liquid filling the gaps between nanoscale features and air filling gaps between macroscopic features, as postulated.

5.0 THEORY OF THE CONE & PLATE RHEOMETER AND PHOTON CORRELATION SPECTROSCOPY

We wish to examine the behavior of our surfaces with respect to bulk liquid flow across them, which can be done in several ways. Such measurements are often comparative, looking at the change in a quantity between a reference and a test samples. By looking at the change in torque applied to the surface, we can see an indication of how much force is being exerted on the surface. Alternatively, by looking at the change in the shear rate $\mathcal{S} = \frac{\partial v_\alpha}{\partial x_\beta}$, we see how much less the fluid is being slowed between the point of energy injection and the dissipative surface of our sample, which in turn tells us how much less energy is being transferred to the surface. The two measurements are related, but measure drag in different ways; torque measurements take an average reading over the surface of the entire sample, while shear rate measurement tells us what is occurring at a specific point.

An apparatus commonly used for measuring torque is the Cone & Plate Rheometer (CPR). Because of the geometry of this system, torque can be related to shear rate theoretically in some cases [52]; this is the conventional method of finding shear rate. However, this relationship depends on simple boundary conditions; one of these conditions is that the plate must be flat. As our samples are expressly not flat plates, we cannot in general utilize these relations, and we must directly measure the shear rate in the fluid.

Direct fluid velocity measurements can be taken using hot wire anemometry [78] or Laser Doppler Velocimetry (LDV) [79]. Obtaining shear rate requires measuring a velocity component at a series of closely spaced points, from which the average slope is deduced. This requires some measurement time at each location and the region of interest must be scanned, so time-resolved measurements of shear are typically not practical with these methods. Furthermore, since hot-wire anemometry requires holding a probe in the flow, it may alter the flow and is sensitive to nearby surfaces [80, 81].

Photon Correlation Spectroscopy (PCS) measures the shear rate directly, does not require any sensor repositioning, does not require calibration or comparison to a reference, and can be performed to within a few percent within minutes. PCS measurements have been used to probe turbulent two-dimensional flow [49], Brownian motion [50], and have been used to approximately measure three-dimensional flow in a Couette cell and four-roll mill [51]. The mathematical treatments in prior work have either been special cases (2-D) or have been approximate derivations with free parameters, requiring calibration using a reference

to achieve relative measurements. We detail a method for PCS measurements of the shear rate in 3-D laminar flow and the beginning of secondary flow in a cone and plate rheometer (CPR) with no free parameters.

5.1 THE CONE & PLATE RHEOMETER

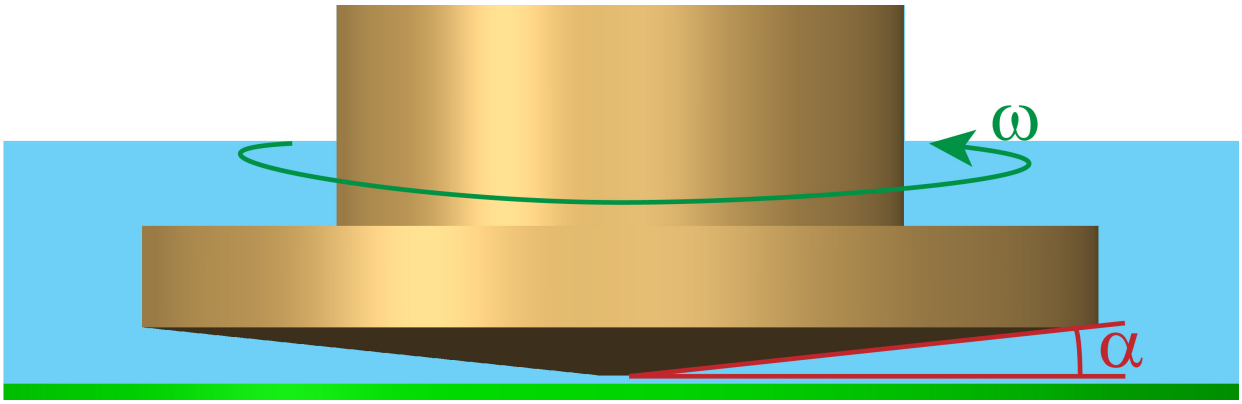

Figure 12: Schematic of a Cone & Plate Rheometer (tip truncation greatly exaggerated). Cone must be positioned such that, if the tip were not truncated, it would touch the plate at the tip. Our experimental samples will serve as the plate.

We begin by discussing the formalism of the Cone & Plate Rheometer. Because the system is cylindrically symmetric, we use a polar coordinate basis (ρ, ϕ, z), such that the origin is at the tip of the cone and $\hat{z}$ is along the axis of rotation. Note that a CPR is always assumed to be positioned so the point of the cone would be in contact with the surface; a real CPR has a small (micro-meter scale) truncation to prevent rubbing, which creates a negligible deviation from theory.

Because a CPR is cylindrically symmetric, we know that in laminar flow all derivatives with respect to the azimuthal direction must vanish $\mathcal{S}_{i\phi} = \frac{\partial v_i}{\partial r_\phi} = 0$. In turbulent flow, these terms may be nonzero, but must obey circular boundary conditions $\mathcal{S}_{i\phi}(\phi = 0) = \mathcal{S}_{i\phi}(\phi = 2\pi)$.

For a CPR, the flow state is characterized by a term proportional to the ratio of the centrifugal to the viscous forces,

$$\tilde{R} = \frac{\rho^2 \omega \alpha^2}{12\nu} = \frac{Re}{12} \tag{5.1}$$

where $\nu = \frac{\eta}{\chi}$ is the kinematic viscosity (we use χ for volume density of the fluid to avoid confusion with the radial coordinate) and Re is the Reynolds number. If $\tilde{R} \lesssim 0.5$ we are in the strictly laminar regime. For $0.5 \lesssim \tilde{R} \lesssim 4.0$, we are experiencing increasing levels of secondary flow. For $\tilde{R} \gtrsim 4.0$, we are firmly in the turbulent regime. This parametric characterization has been thoroughly tested; the factor of 12 in the denominator is a consequence of the Navier-Stokes equations [82]. Note that for measurements that take into account the entire gap, turbulence will begin at the edges of the cone and proceed inward as ω is increased.

5.1.1 Laminar Flow

We can solve the equations governing our system in laminar flow. In the laminar case, $v_\rho = v_z = 0$, as cross flow is a property of turbulence. The continuity equation in cylindrical coordinates is $\vec{\bigtriangledown} \cdot \vec{v} = \frac{1}{\rho}\frac{\partial \rho v_\rho}{\partial \rho} + \frac{1}{\rho}\frac{\partial v_\phi}{\partial \phi} + \frac{\partial v_z}{\partial z}$, which in the laminar case reduces to $0 = \frac{\partial v_\phi}{\partial \phi}$.

First, we examine the rheometer for the case of a flat plate. The boundary conditions are $v_\phi(z_c) = \omega\rho = \omega\frac{z_c}{\tan(\alpha)} \approx \omega\frac{z_c}{\alpha}$ and $v_\phi(0) = 0$, assuming a small cone angle $\alpha(\lesssim 6^\circ)$ and a cone surface defined by $z_c = \rho\tan(\alpha)$ (remembering that the cone tip,if it were not truncated, is treated as touching the plate at $\rho = 0$). Then $v_\phi(z) = \frac{\omega}{\alpha}z$, and thus the only nonzero component of the shear rate is

$$\mathcal{S}_{\phi z} = \frac{\omega}{\alpha} \tag{5.2}$$

which is independent of radial position. This means that in this case we can measure the shear rate anywhere in the gap. Radial independence is the reason a cone is chosen for the upper surface; if we replace the cone with another flat plate, we would instead have a Parallel Plate Rheometer, where the gap between the plates h could be set arbitrarily; then $v_\phi(z) = \frac{\omega\rho}{h}z$ and $\mathcal{S}_{\phi z} = \frac{\omega\rho}{h}$ are proportional to radius [52].

The stress on a plane is $\vec{\mathcal{T}}_{\phi z} = \frac{F_\phi}{A_{\phi z}}\hat{\phi} = -\eta \mathcal{S}_{\phi z}\hat{\phi}$, where F_ϕ is the sheering force on a plane with area $A_{\phi z}$ in the $\hat{\phi}$ direction of fluid with dynamic viscosity η. The torque τ on such a plane about the axis of fluid rotation is then

$$\tau = \int (\vec{\rho} \times \vec{\mathcal{T}}_{\phi z}) dA = \int_0^{2\pi} \int_0^R \rho |\mathcal{T}_{\phi z}| \rho d\rho d\phi = \frac{2\pi\eta R^3}{3}\mathcal{S}_{\phi z} = \frac{2\pi\eta R^3 \omega}{3\alpha} \tag{5.3}$$

Where R is the radius of the cone. This relation is what is used to measure shear rate in commercial CPR systems.

The preceding deals with a rheometer in which the plate is in the Wenzel state and only a single fluid occupies the entire gap [52]. In the event that the plate is altered so it retains a second fluid layer, so we have the water in contact with another fluid layer and the second fluid layer in contact with the plate, we must now treat both layers. If the second fluid is air, this is the the Cassie-Baxter state. The boundary condition at the cone is unchanged, $v_\phi(z_c) = \omega\frac{z_c}{\alpha}$. If we assume that the plate is still approximately flat, the boundary condition at the lower plate is the same for the second fluid, so $v'_\phi(0) = 0$, where primed variables are in the second fluid. New intermediate boundary conditions are introduced by matching the mutual stress and the velocity of the two fluids at the interface where the fluid layers interact, $v_\phi(z_t) = v'_\phi(z_t)$ and $\eta\frac{\partial v_\phi}{\partial z}|_{z_t} = \eta'\frac{\partial v'_\phi}{\partial z}|_{z_t}$, where z_t is the location of the boundary. Letting $H = \frac{\eta'}{\eta}$, the velocities in the two fluids are now

$$v_\phi(z) = \frac{\omega z_c[Hz + z_t(1-H)]}{\alpha[Hz_c + z_t(1-H)]} \qquad\qquad v'_\phi(z) = \frac{\omega z_c z}{\alpha[Hz_c + z_t(1-H)]}$$

We define the common factor of $z_t(\frac{1}{H} - 1) = z_t(\frac{\eta}{\eta'} - 1) = \delta$. The velocities and shear rates in the two fluids are then

$$\begin{aligned} v_\phi(z) &= \frac{\omega}{\alpha}\frac{\rho\alpha(z+\delta)}{(\rho\alpha+\delta)} & v'_\phi(z) &= \frac{\omega}{\alpha}\frac{\eta\rho\alpha z}{\eta'(\rho\alpha+\delta)} \\ \mathcal{S}_{\phi z} &= \frac{\omega}{\alpha}\frac{\rho\alpha}{(\rho\alpha+\delta)} & \mathcal{S}'_{\phi z} &= \frac{\omega}{\alpha}\frac{\eta\rho\alpha}{\eta'(\rho\alpha+\delta)} \end{aligned} \tag{5.4}$$

Where we see that, unfortunately, shear rate is no longer radially independent.

Looking at the velocity of the upper fluid, we see that $v_\phi(-\delta) = 0$, so δ is the position of an imaginary surface some distance from the real surface at $z = 0$ where the velocity of the upper fluid would be zero. This distance is referred to as the slip length, and is an alternative

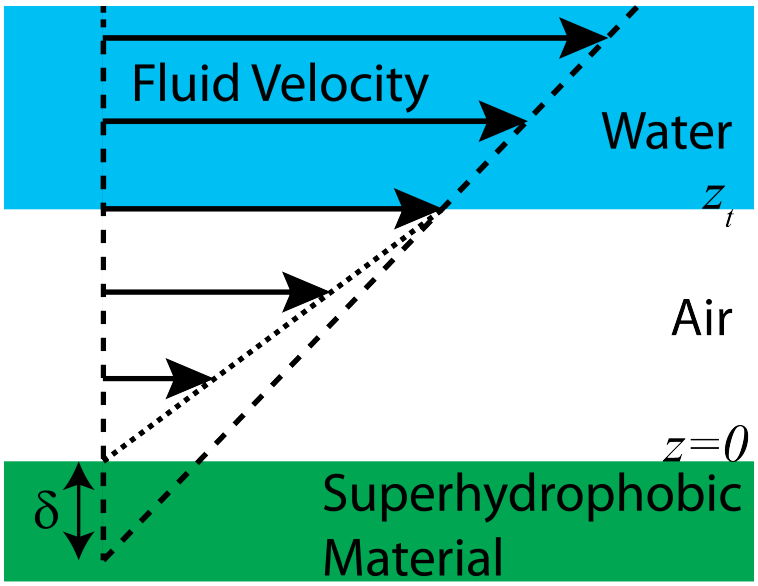

Figure 13: Graphical Explanation of Drag Reduction in the Cassie-Baxter State. This shows that the extrapolated velocity of the water is non-zero at the plate when an air layer is providing lubrication, so the water appears to be slipping. The no slip condition appears to apply a distance δ inside the material.

way to quantify drag reduction. If $\eta' < \eta$, then $\delta > 0$ and the velocity of the upper fluid is higher than in the single fluid case. The velocity of the primary fluid extrapolated to the interface with the plate now has non-zero velocity, and so can be said to be slipping, hence the name.

Integrating as in Eq. 5.3, the total torque on the plate in laminar flow is now

$$\tau = 2\pi\eta\omega \left[\frac{R\alpha(6\delta^2 - 3R\alpha\delta + 2\alpha^2 R^2)}{6\alpha^4} + \frac{\delta^3}{\alpha^4} \ln\left(\frac{\delta}{R\alpha + \delta}\right) \right] \tag{5.5}$$

Which is significantly more complicated than the single fluid case. It is smaller than the single fluid case so long as $\eta' < \eta$, showing that adding a second fluid with lower viscosity does reduce the torque. The torque no longer displays a simple proportionality with shear rate, making it harder to understand exactly what lower shear rate means in terms of torque applied to the surface.

The preceding still posits that we can treat the plate surface and interface between the fluid as approximately flat. For our PAA spikes alone, this may be an acceptable approximation. However, once millimeter scale grooves of any significant depth d and angle from the horizontal ϕ' (using the notation from chapter 2) are added, this approximation will very quickly break down, so we must consider a final case. The boundary condition at the cone is still unchanged, $v_\phi(z_c) = \omega\frac{z_c}{\alpha}$. The boundary condition at the lower plate for the fluid that is in contact with it, $v'_\phi(\zeta) = 0$, is now more complicated, as the lower surface is now represented by a triangle function $\zeta(\rho, \rho_0, d, \phi') = -\frac{2d}{\pi}\sin^{-1}[\sin(\frac{\pi}{d}\tan(\phi')(\rho-\rho_0))]$, where the grooves are cut into the original surface and begin at some radius ρ_0 (the surface is assumed flat for $\rho < \rho_0$). The intermediate fluid interaction conditions, $v_\phi(z_t(\zeta)) = v'_\phi(z_t(\zeta))$ and $\eta\frac{\partial v_\phi}{\partial z}|_{z_t(\zeta)} = \eta'\frac{\partial v'_\phi}{\partial z}|_{z_t(\zeta)}$, are still the same in form, but $z_t(\zeta)$ is no longer a constant distance from the $z = 0$ plane. The velocities in the two fluids are now

$$v_\phi(\rho, z) = \frac{\omega z_c[H[z + \zeta(\rho)] + [z_t(\zeta(\rho)) + \zeta(\rho)](1 - H)]}{\alpha[H[z_c + \zeta(\rho)] + [z_t(\zeta(\rho)) + \zeta(\rho)](1 - H)]}$$
$$v'_\phi(\rho, z) = \frac{\omega z_c[z + \zeta(\rho)]}{\alpha[H[z_c + \zeta(\rho)] + [z_t(\zeta(\rho)) + \zeta(\rho)](1 - H)]}$$

Which is dependent on the radial position and the shape of the fluid interface. We define the common factor of $[z_t(\zeta(\rho)) + \zeta(\rho)](\frac{1}{H} - 1) = \tilde{\delta}(\zeta(\rho))$, the effective spatially varying slip length. The velocities and shear rates in the two fluids are then

$$v_\phi(\rho, z) = \frac{\omega}{\alpha}\frac{\rho\alpha[z + \zeta(\rho) + \tilde{\delta}(\zeta(\rho)]}{[\rho\alpha + \zeta(\rho) + \tilde{\delta}(\zeta(\rho))]} \qquad v'_\phi(z) = \frac{\omega}{\alpha}\frac{\eta\rho\alpha[z + \zeta(\rho)]}{\eta'[\rho\alpha + \zeta(\rho) + \tilde{\delta}(\zeta(\rho))]}$$
$$\mathcal{S}_{\phi z} = \frac{\omega}{\alpha}\frac{\rho\alpha}{[\rho\alpha + \zeta(\rho) + \tilde{\delta}(\zeta(\rho))]} \qquad \mathcal{S}'_{\phi z} = \frac{\omega}{\alpha}\frac{\eta\rho\alpha}{\eta'[\rho\alpha + \zeta(\rho) + \tilde{\delta}(\zeta(\rho))]} \tag{5.6}$$

and so the equation for the torque is

$$\tau = \int(\vec{\rho}\times\vec{\mathcal{T}}_{\phi z})dA = \int_0^{2\pi}\int_0^R \rho|\mathcal{T}_{\phi z}|\rho d\rho d\phi = 2\pi\eta\int_0^R \rho\left|\frac{\omega}{\alpha}\frac{\rho\alpha}{[\rho\alpha + \zeta(\rho) + \tilde{\delta}(\zeta(\rho))]}\right|\rho d\rho \tag{5.7}$$

Without knowing the form of $\tilde{\delta}(\zeta(\rho))$, we cannot integrate this to obtain a torque relation (given the form of $\zeta(\rho)$, it is likely non-analytic in any case). Therefore, we cannot state any analytic relationship between shear rate and torque for these surfaces.

Based on this, we can see that a simple relation between torque and shear rate is truly achieved only in the case of a flat cone and a flat plate. This arrangement is commonly used to the properties of unknown fluids [53], but is useful for us only in that it allows us a case where we can very easily test any independent shear rate measurement we use.

5.1.2 Turbulent Flow

For turbulent flow, multiple terms in the shear rate tensor can be non-zero, and determining any of them requires further knowledge of the flow state. Additionally, any fluid-fluid interface is not well defined due the specially random nature of turbulence; determining the impact of the addition of large scale structure increases the complications even further. Theoretical discussion in turbulence is difficult and we cannot directly relate torque and shear rate in this regime.

5.2 PHOTON CORRELATION SPECTROSCOPY

In general CPR system usage, shear rate in fluids is measured using Eq. 5.3 and a smooth cone and plate [52]. We explicitly aim to measure the shear rate in water relative to a surface with unknown properties, where there may not be a simple relationship between torque and shear rate (see for example Eq. 5.7). Therefore we must measure the shear rate directly from the fluid, in a way that does not require that we know the exact form of the relationship between shear rate and torque beforehand. We utilize PCS measurements to obtain this information.

PCS measurements use laser light that is scattered from small particles that seed the flow in our CPR [83]. The scattered light is collected and the interference between the light scattered from pairs of particles results in the decay of the intensity autocorrelation function. At higher shear rates there is a larger spread of particle velocities and thus a wider spread of Doppler-shifted frequencies in the scattered light, which decreases the decay time of the autocorrelation function. Unlike LDV, which similarly uses the light scattered from

particles to measure velocity but uses a local oscillator (or multiple beams) for a heterodyne measurement, PCS is a homodyne measurement; no additional signal is mixed in.

PCS measures the normalized intensity autocorrelation function $G(\tau) = \frac{\langle I(t)I(t+\tau)\rangle}{|\langle I(t)\rangle|^2} - 1$, where the angular brackets designate an average over time and I indicates the intensity of light scattered from the particles. Scattering occurs in a volume containing N scattering particles defined by the intersection of the input beam and the field of view of the detector, which is a collimating lens feeding into a single mode optical fiber. If the input beam is a collimated Gaussian laser beam, then the electric field incident on the j^{th} particle is

$$\begin{aligned}\vec{E}_{incident,j}(t) &= \vec{E}_0 e^{-i\vec{k}_0\cdot\vec{r}_j(t)+i\omega_0 t} e^{-[\vec{r}_j(t)\cdot\vec{a}]^2} e^{-[\vec{r}_j(t)\cdot\vec{b}]^2} \\ &= \vec{E}_0 e^{-i\vec{k}_0^T\vec{r}_j(t)+i\omega_0 t} e^{-\vec{r}_j(t)^T\mathcal{Z}_1\vec{r}_j(t)}\end{aligned} \tag{5.8}$$

where $\vec{r}_j$ is the displacement from the center of the scattering volume to the j^{th} particle, $\vec{a}$ and $\vec{b}$ are the semi-major and semi-minor axes of the input beam (allowing for the possibility of an elliptical beam), and $\vec{k}_0$ is the input beam wave vector along the axis of the input beam ($|\vec{k}_0| = \frac{2\pi n}{\lambda}$). We write these using tensor notation (tensors represented by calligraphic symbols) to simplify and generalize the form of the equations, where all vector quantities are column vectors:

$$\vec{k}_0 = \frac{2\pi n}{\lambda}\begin{pmatrix}k_{01}\\k_{02}\\k_{03}\end{pmatrix} \qquad \vec{a} = \frac{\hat{a}}{w_a} = \begin{pmatrix}a_1/w_a\\a_2/w_a\\a_3/w_a\end{pmatrix} \qquad \vec{b} = \frac{\hat{b}}{w_b} = \begin{pmatrix}b_1/w_b\\b_2/w_b\\b_3/w_b\end{pmatrix}$$

$$\mathcal{Z}_1 = \vec{a}\vec{a}^T + \vec{b}\vec{b}^T = \begin{pmatrix}\frac{b_1^2w_a^2+a_1^2w_b^2}{w_a^2w_b^2} & \frac{b_1b_2w_a^2+a_1a_2w_b^2}{w_a^2w_b^2} & \frac{b_1b_3w_a^2+a_1a_3w_b^2}{w_a^2w_b^2}\\ \frac{b_1b_2w_a^2+a_1a_2w_b^2}{w_a^2w_b^2} & \frac{b_2^2w_a^2+a_2^2w_b^2}{w_a^2w_b^2} & \frac{b_2b_3w_a^2+a_2a_3w_b^2}{w_a^2w_b^2}\\ \frac{b_1b_3w_a^2+a_1a_3w_b^2}{w_a^2w_b^2} & \frac{b_2b_3w_a^2+a_2a_3w_b^2}{w_a^2w_b^2} & \frac{b_3^2w_a^2+a_3^2w_b^2}{w_a^2w_b^2}\end{pmatrix}$$

where w_a and w_b indicate the radius at which the field drops to $\frac{1}{e}$ in that direction and the numeric subscripts indicate projection. For a circular input beam, $w_a = w_b = w_0$ and $2w_0$ is the conventional intensity $\frac{1}{e^2}$ beam diameter commonly given by laser manufactures.

When light scatters from a particle illuminated by the input beam, the scattered electric field is a spherical wave, and at center of the lens of our detector it can be written as

$$\vec{E}_{scattered,j}(t) = \vec{E}_{incident,j}(t)\frac{e^{-i\kappa_j|\vec{R}-\vec{r}_j(t)|+i\omega_{sj}t}}{|\vec{R}-\vec{r}_j(t)|} \approx \vec{E}_{incident,j}(t)\frac{e^{-i\vec{\kappa}_j\cdot\vec{R}}}{R}e^{i\vec{\kappa}_j\cdot\vec{r}_j(t)}e^{i\omega_{sj}t} \tag{5.9}$$

where $\vec{R}$ is the displacement from the center of the scattering volume to the center of the detector along the optical axis of the detector, ω_{sj} is the frequency of the light scattered off the j^{th} particle and $\vec{\kappa}_j$ is the scattering vector from the j^{th} particle ($|\vec{\kappa}_j| = \frac{2\pi n}{\lambda}$; n is the fluid index of refraction and λ is the laser wavelength). Looking at the equations, we see that $\vec{\kappa}_j$ is parallel to $\vec{R} - \vec{r}_j(t)$, so $\kappa_j|\vec{R} - \vec{r}_j(t)| = \vec{\kappa}_j \cdot (\vec{R} - \vec{r}_j(t)) = \vec{\kappa}_j \cdot \vec{R} - \vec{\kappa}_j \cdot \vec{r}_j(t)$. We have also assumed $\vec{R} \gg \vec{r}_j(t)$ in the denominator of Eq. 5.9.

Allowing for the possibility of an elliptical detector, the lens-fiber detector system has effective major and minor axes $\vec{c}$ and $\vec{d}$ respectively:

$$\vec{c} = \frac{\hat{c}}{w_c} = \begin{pmatrix} c_1/w_c \\ c_2/w_c \\ c_3/w_c \end{pmatrix} \qquad \vec{d} = \frac{\hat{d}}{w_d} = \begin{pmatrix} d_1/w_d \\ d_2/w_d \\ d_3/w_d \end{pmatrix}$$

where w_c and w_d indicate the radius at which the electric field of a beam emitted from the fiber through the lens drops to $\frac{1}{e}$ in that direction. Only a fraction of the light scattered off each particle is coupled in the single mode fiber by the lens of the detector. Thus the field in the center of the fiber is $\vec{E}_j(t) \propto \sqrt{\eta_j(t)}\vec{E}_{scattered,j}(t)$, where $\eta_j(t)$ is the coupling efficiency, the fraction of the power transferred to the detector by the light scattered from the j^{th} particle [84].

In order to determine the coupling efficiency $\eta_j(t)$, we rewrite Eq. 5.9 for any observation point.

$$\vec{E}_{scattered,j}(\vec{h}, t) = \vec{E}_{incident,j}(t)\frac{e^{-iK|\vec{h}+\vec{g}(t)|}}{|\vec{h} + \vec{g}(t)|} \tag{5.10}$$

where K is the magnitude of the scattering vector parallel to $\vec{h} + \vec{g}(t)$ ($|\vec{K}| = \frac{2\pi n}{\lambda}$), $\vec{g}(t) = \vec{R} - \vec{r}_j(t)$ is the displacement from the particle to the center of the collimating lens, and $\vec{h}$ is the vector to the observation point from the center of the lens. We neglect the phase factor $e^{i\omega_s t}$ as it has no spatial dependence. Although the vector $\vec{K}$ changes direction as a function of $\vec{h}$, the magnitude is constant.

The field in a plane parallel to the plane of the lens may be represented by the collimated Gaussian TEM_{00} mode

$$E_f(\vec{h}) = E_{fi}e^{-(\vec{h}\cdot\vec{c})^2}e^{-(\vec{h}\cdot\vec{d})^2} \tag{5.11}$$

where E_{fi} is the field magnitude.

The coupling efficiency is given by the overlap integral

$$\eta_j(t) = \frac{\left|\int_A E_{scattered,j}(\vec{h},t)E_f^*(\vec{h})dA\right|^2}{\left|\int_A E_{scattered,j}^2(\vec{h},t)dA\right|\left|\int_A E_f^2(\vec{h})dA\right|} \tag{5.12}$$

which indicates the ratio of power coupling between the modes through a surface A to the total power in each mode [84]. Because $G(\tau)$ depends on the ratio of intensities, in all cases the constant normalization terms in the denominator are unimportant.

Turning to the coupling term, for the plane containing the lens we have

$$\eta_j(t) \propto \left|\int_A E_{scattered,j}(\vec{h},t)E_f^*(\vec{h})dA\right|^2 \approx \left|\int_A \frac{e^{-iK|\vec{h}+\vec{g}(t)|}}{|\vec{h}+\vec{g}(t)|}e^{-(\vec{h}\cdot\vec{c})^2}e^{-(\vec{h}\cdot\vec{d})^2}dA\right|^2 \tag{5.13}$$

which is non-analytic. However, since the integral is over this infinite plane, the integral must be the same on any parallel surface (so long as the reversed detector beam would still be approximately collimated when it passes through that surface), and we are free to choose the most convenient one. Thus we evaluate that integral on the surface containing the scattering particle, where $E_{scattered,j}(\vec{h},t) = E_{incident,j}(t)\delta(\vec{h}-\vec{g}(t))$, which gives

$$\eta_j(t) \propto \left|e^{-(-\vec{g}(t)\cdot\vec{c})^2}e^{-(-\vec{g}(t)\cdot\vec{d})^2}\right|^2 \tag{5.14}$$

We can also approximately evaluate the integral on the plane containing the lens. Looking at the spherical wave, $|\vec{h}+\vec{g}(t)| = \sqrt{h^2+g(t)^2+2\vec{h}\cdot\vec{g}(t)} \approx g(t) + \frac{h^2}{2g(t)} + \frac{\vec{h}\cdot\vec{g}(t)}{g(t)}$, where we have Taylor expanded to 1^{st} order with $g(t) > h$; we cannot a priori say that $h^2/2 \ll \vec{h}\cdot\vec{g}(t)$ (as $\vec{g}(t)$ and $\vec{h}$ are nearly perpendicular). If we retain both terms in this expansion, $E_{scattered,j}(\vec{h},t) \approx E_{incident,j}(t)\frac{e^{-iK\left(g(t)+\frac{h^2}{2g(t)}+\frac{\vec{h}\cdot\vec{g}(t)}{g(t)}\right)}}{g(t)}$, so

$$\begin{aligned}\eta_j(t) &\propto \left|\frac{e^{-iKg(t)}}{g(t)}\int e^{-iK\left(\frac{h^2}{2g(t)}+\frac{\vec{h}\cdot\vec{g}(t)}{g(t)}\right)}e^{-(\vec{h}\cdot\vec{c})^2}e^{-(\vec{h}\cdot\vec{d})^2}dA\right|^2 \\ &= \left|\frac{e^{-iKg(t)}}{g(t)}\frac{1}{\sqrt{(\frac{2}{w_c^2}-i\frac{K}{g(t)})(\frac{2}{w_d^2}-i\frac{K}{g(t)})}}e^{-\frac{K^2(-\vec{g}(t)\cdot\vec{c})^2w_c^4}{4g(t)^2-2ig(t)Kw_c^2}}e^{-\frac{K^2(-\vec{g}(t)\cdot\vec{d})^2w_d^4}{4g(t)^2-2ig(t)Kw_d^2}}\right|^2\end{aligned} \tag{5.15}$$

If we do not retain $h^2/2$, then we have performed the plane wave approximation and $E_{scattered,j}(\vec{h},t) \approx E_{incident,j}(t)\frac{e^{-iK\left(g(t)+\frac{\vec{h}\cdot\vec{g}(t)}{g(t)}\right)}}{g(t)}$, which gives

$$\begin{aligned}\eta_j(t) &\propto \left|\frac{e^{-iKg(t)}}{g(t)}\int e^{-iK\frac{\vec{h}\cdot\vec{g}(t)}{g(t)}}e^{-(\vec{h}\cdot\vec{c})^2}e^{-(\vec{h}\cdot\vec{d})^2}dA\right|^2 \\ &= \left|\frac{e^{-iKg(t)}}{g(t)}\pi w_c w_d e^{-\frac{K^2}{4g(t)^2}[(-\vec{g}(t)\cdot\vec{c})^2 w_c^4+(-\vec{g}(t)\cdot\vec{d})^2 w_d^4]}\right|^2 \end{aligned} \tag{5.16}$$

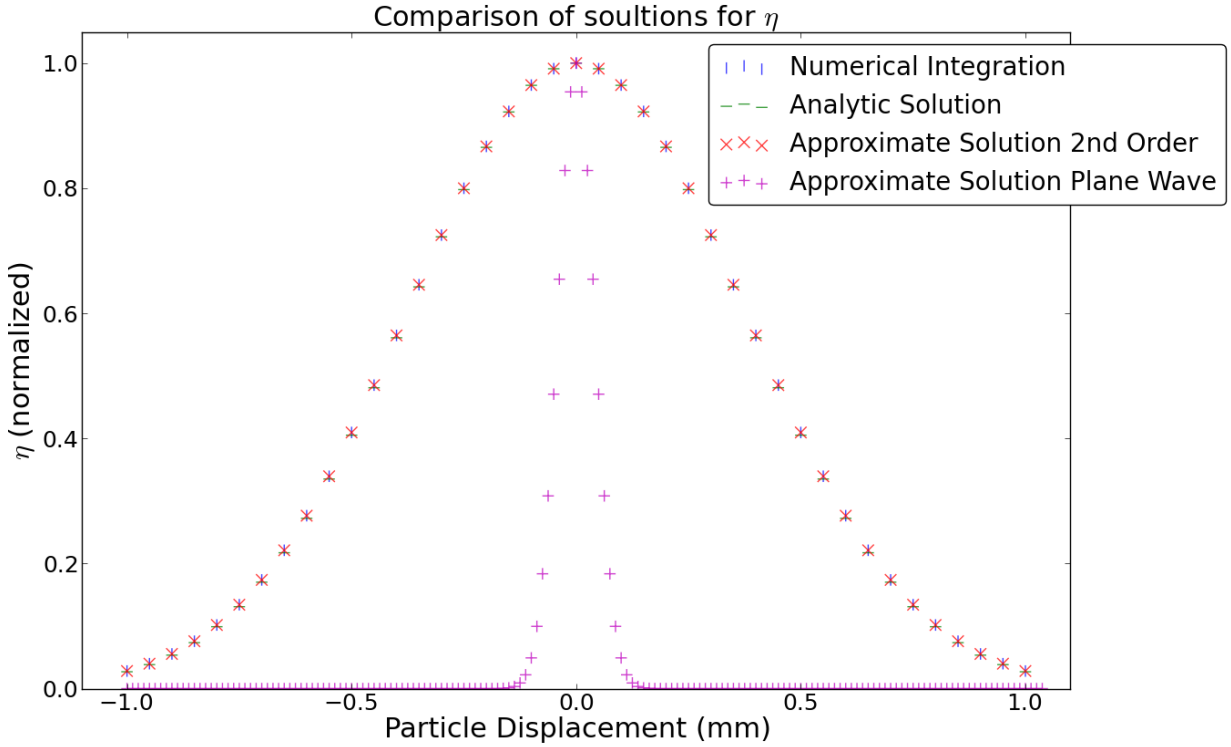

Figure 14: Comparison of the coupling efficiency in water at $g = 200$ mm and $\lambda = 633$ nm, as calculated numerically on the plane of the lens, analytically evaluated on the plane containing the particle, and approximately integrated on the plane of the lens. We also show the result of evaluating with a plane wave approximation (neglecting $h^2/2$) to demonstrate that this is an overapproximation.

A comparison of Eq. 5.14, Eq. 5.15 and the numerical integral of Eq. 5.13 shows excellent agreement when g is small compared to Kw_c and Kw_d, which is precisely the limit where

diffraction effects are not large. By contrast, Eq 5.16 is very different, showing that the plane wave approximation is a poor choice in this case (See Fig. 14).

Finally, using the exact solution (Eq. 5.14), remembering that $\vec{g}(t) = \vec{R} - \vec{r}_j(t)$, and noticing that $\vec{R} \perp \vec{c}$ and $\vec{R} \perp \vec{d}$ by definition, we see that

$$\eta_j(t) \propto \left| e^{-(-[\vec{R}-\vec{r}_j(t)]\cdot\vec{c})^2} e^{-(-[\vec{R}-\vec{r}_j(t)]\cdot\vec{d})^2} \right|^2 = \left| e^{-(\vec{r}_j(t)\cdot\vec{c})^2} e^{-(\vec{r}_j(t)\cdot\vec{d})^2} \right|^2 = |e^{-\vec{r}_j^T(t)\mathcal{Z}_2\vec{r}_j(t)}|^2 \tag{5.17}$$

where

$$\mathcal{Z}_2 = \vec{c}\vec{c}^T + \vec{d}\vec{d}^T = \begin{pmatrix} \frac{d_1^2 w_c^2 + c_1^2 w_d^2}{w_c^2 w_d^2} & \frac{d_1 d_2 w_c^2 + c_1 c_2 w_d^2}{w_c^2 w_d^2} & \frac{d_1 d_3 w_c^2 + c_1 c_3 w_d^2}{w_c^2 w_d^2} \\ \frac{d_1 d_2 w_c^2 + c_1 c_2 w_d^2}{w_c^2 w_d^2} & \frac{d_2^2 w_c^2 + c_2^2 w_d^2}{w_c^2 w_d^2} & \frac{d_2 d_3 w_c^2 + c_2 c_3 w_d^2}{w_c^2 w_d^2} \\ \frac{d_1 d_3 w_c^2 + c_1 c_3 w_d^2}{w_c^2 w_d^2} & \frac{d_2 d_3 w_c^2 + c_2 c_3 w_d^2}{w_c^2 w_d^2} & \frac{d_3^2 w_c^2 + c_3^2 w_d^2}{w_c^2 w_d^2} \end{pmatrix}$$

Then, the electric field in center of the fiber from a single scattering particle is

$$\vec{E}_j(t) \propto \frac{e^{-i\vec{\kappa}_j^T\vec{R}}}{R} \vec{E}_{incident,j}(t) e^{i\vec{\kappa}_j^T\vec{r}_j(t) + i\omega_{sj}t} e^{-\vec{r}_j^T(t)\mathcal{Z}_2\vec{r}_j(t)} \tag{5.18}$$

Combining Eq. 5.18 and Eq. 5.8, we find that the detected field from a single scattering particle is

$$\vec{E}_j(t) = \vec{E}_D e^{-i\vec{k}_j^T\vec{r}_j(t) + i\omega_j' t} e^{-\vec{r}_j^T(t)\mathcal{Z}\vec{r}_j(t)} \tag{5.19}$$

where $\omega_j' = \omega_0 + \omega_{sj}$ is the Doppler-shifted frequency of the light scattered off the j^{th} particle, $\vec{k}_j = \vec{k}_0 - \vec{\kappa}_j$ is the net scattering vector ($|\vec{k}_j| = \frac{4\pi n}{\lambda}\sin(\theta_j/2)$; θ_j is the scattering angle for the j^{th} particle), $\mathcal{Z} = \mathcal{Z}_1 + \mathcal{Z}_2$, and $\vec{E}_D \propto \vec{E}_0 \frac{e^{-i\vec{\kappa}_j^T\vec{R}}}{R}$ is the magnitude of the field, which is constant. Because of the form of $G(\tau)$, the value of $\vec{E}_D$ does not matter.

We assume that the particles are small enough that the velocity of each particle is the same as the velocity of the fluid at that location, that the fluid velocity is time-independent during the measurement, and that the beam is sufficiently small that the velocity of the fluid can be described by a first order expansion about the center of the beam. Then the position of the particles at some later time $t + \tau$ can be written as

$$\vec{r}_j(t+\tau) = \vec{r}_j(t) + \vec{v}\tau + \mathcal{S}\vec{r}_j(t)\tau + \vec{r}_{dif,j}(\tau) \tag{5.20}$$

where $\vec{v}$ is the average velocity of the fluid, $\vec{r}_{dif,j}(\tau)$ is additional displacement due to diffusion in the time τ between t and $t+\tau$, and the shear rate tensor is

$$\mathcal{S} = \frac{\partial v_\alpha}{\partial r_\beta} = \begin{pmatrix} \frac{\partial v_1}{\partial r_1} & \frac{\partial v_1}{\partial r_2} & \frac{\partial v_1}{\partial r_3} \\ \frac{\partial v_2}{\partial r_1} & \frac{\partial v_2}{\partial r_2} & \frac{\partial v_2}{\partial r_3} \\ \frac{\partial v_3}{\partial r_1} & \frac{\partial v_3}{\partial r_2} & \frac{\partial v_3}{\partial r_3} \end{pmatrix}$$

Then at a time $t+\tau$ Eq. 5.19 becomes

$$\begin{aligned} \vec{E}_j(t+\tau) &= \vec{E}_D e^{-i\vec{k}_j^T[\vec{r}_j(t)+\vec{v}\tau+\mathcal{S}\vec{r}_j(t)\tau+\vec{r}_{dif,j}(\tau)]+i\omega_j'(t+\tau)} e^{-[\vec{r}_j(t)+\vec{v}\tau]^T\mathcal{Z}[\vec{r}_j(t)+\vec{v}\tau]} \\ &= \vec{E}_D e^{-i\vec{k}_j^T\vec{v}\tau} e^{-\vec{v}^T\mathcal{Z}\vec{v}\tau^2} e^{i\omega_j'(t+\tau)} e^{-i\vec{k}_j^T\vec{r}_{dif,j}(\tau)} e^{-i\vec{k}_j^T[\vec{r}_j(t)+\mathcal{S}\vec{r}_j(t)\tau]} e^{-\vec{r}_j^T(t)\mathcal{Z}\vec{r}_j(t)} e^{-2\vec{v}^T\mathcal{Z}\vec{r}_j(t)\tau} \end{aligned} \tag{5.21}$$

Returning to the definition of $G(\tau)$, we have

$$G(\tau) = \frac{\langle I(t)I(t+\tau)\rangle}{\langle I(t)\rangle^2} - 1 = \frac{\sum_{ijkl}\left\langle E_i(t)E_j^*(t)E_k(t+\tau)E_l^*(t+\tau)\right\rangle}{\left|\sum_{mn}\langle E_m(t)E_n^*(t)\rangle\right|^2} - 1 \tag{5.22}$$

Terms relating more than two particles do not survive averaging over time if the particle distribution is random and the particles are spread over a volume larger than the wavelength of light used in all dimensions [85]. Applying this condition, only terms with pairs of particles can survive in the numerator. We also note that the expectation values of the different sums are independent. Therefore,

$$\begin{aligned} G(\tau) &= \frac{\sum_{ik}\langle E_i(t)E_i^*(t)E_k(t+\tau)E_k^*(t+\tau)\rangle + \sum_{ik}\langle E_i(t)E_k^*(t)E_k(t+\tau)E_i^*(t+\tau)\rangle}{\left|\sum_{mn}\langle E_m(t)E_n^*(t)\rangle\right|^2} - 1 \\ &= \frac{\left|\sum_j\left\langle E_j(t)E_j^*(t)\right\rangle\right|^2 + \left|\sum_j\left\langle E_j(t)E_j^*(t+\tau)\right\rangle\right|^2}{\left|\sum_{mn}\langle E_m(t)E_n^*(t)\rangle\right|^2} - 1 \end{aligned} \tag{5.23}$$

For the denominator,

$$|\langle I(t)\rangle|^2 = \left|\sum_{mn}\langle E_m(t)E_n^*(t)\rangle\right|^2 = \left|\sum_{m\neq n}\langle E_m(t)E_n^*(t)\rangle\right|^2 + \left|\sum_{j}\langle E_j(t)E_j^*(t)\rangle\right|^2$$
$$= \left|\sum_{j}\langle E_j(t)E_j^*(t)\rangle\right|^2 = \left|E_D^2\sum_{j}\langle e^{-2\vec{r}_j^T(t)\mathcal{Z}\vec{r}_j(t)}\rangle\right|^2$$
$$= \left|E_D^2 N\int_{-\infty}^{\infty} e^{-2\vec{r}^T(t)\mathcal{Z}\vec{r}(t)}d^n r(t)\right|^2 = \left|E_D^2 N\sqrt{\frac{\pi^n}{det(2\mathcal{Z})}}\right|^2 = E_D^4 N^2\frac{\pi^n}{det(2\mathcal{Z})} \qquad (5.24)$$

where each of the N expectation values is identical and the integral is n-Dimensional for generality.[1]

The first term in the numerator of Eq. 5.23 is identical to Eq. 5.24. For particles inside the scattering volume, there will be very little variation in the scattering vectors, so we can let $\vec{k}_j = \vec{k}_0 - \vec{\kappa}_j \approx \vec{k}_0 - \vec{\kappa} = \vec{k}$, where $\vec{k}$ is the average total scattering vector ($\vec{\kappa}$ is the average scattered wave vector which is along the axis of the detector) and $\omega_j' \approx \omega'$, where ω' is the average total phase shift. We see that each term in the sums is identical in form and integrated over all space. We also note that displacement due to diffusion is independent of the particle position, and so is integrated separately. Therefore

$$\left|\sum_{j}\langle E_j(t)E_j^*(t+\tau)\rangle\right|^2 =$$
$$|E_D^2\sum_{j}\langle e^{i\vec{k}^T\vec{v}\tau}e^{-\vec{v}^T\mathcal{Z}\vec{v}\tau^2}e^{-i\omega'\tau}e^{i\vec{k}^T\vec{r}_{dif,j}(\tau)}e^{i\vec{k}^T\mathcal{S}\vec{r}_j(t)\tau}e^{-2\vec{r}_j^T(t)\mathcal{Z}\vec{r}_j(t)}e^{-2\vec{v}^T\mathcal{Z}\vec{r}_j(t)\tau}\rangle|^2 =$$
$$E_D^4 e^{-2\vec{v}^T\mathcal{Z}\vec{v}\tau^2}\times$$
$$\left|\sum_{j}\int_{-\infty}^{\infty}P(\vec{r}_{dif,j}(\tau))e^{i\vec{k}^T\vec{r}_{dif,j}(\tau)}d^n r_{dif,j}(\tau)\int_{-\infty}^{\infty}e^{i\vec{k}^T\mathcal{S}\vec{r}_j(t)\tau}e^{-2\vec{r}_j^T(t)\mathcal{Z}\vec{r}_j(t)}e^{-2\vec{v}^T\mathcal{Z}\vec{r}_j(t)\tau}d^n r_j(t)\right|^2 \qquad (5.25)$$

where $P(\vec{r}_{dif}(\tau))$ is the n-D probability distribution of the displacement due to diffusion. The integrals are evaluated over all possible particle positions and diffusion displacements.

[1] $\int_{-\infty}^{\infty} e^{-x^T\mathcal{A}x}\,d^n x = \sqrt{\frac{(\pi)^n}{\det\mathcal{A}}}$. This can be verified by applying the unitary transform $a^\dagger a = 1$, where this diagonalizes $\mathcal{A}$, and then performing the integral in eigenspace. Such a transformation does not change the determinant.

For the integral over particle positions in Eq. 5.25, we have[2]

$$\int_{-\infty}^{\infty} e^{i\vec{k}^T\mathcal{S}\vec{r}_j(t)\tau}e^{-2\vec{r}_j^T(t)\mathcal{Z}\vec{r}_j(t)}e^{-2\vec{v}^T\mathcal{Z}\vec{r}_j(t)\tau}d^n r_j(t) = \sqrt{\frac{\pi^n}{det(2\mathcal{Z})}}e^{-\frac{1}{8}\vec{k}^T\mathcal{S}(2\mathcal{Z})^{-1}\mathcal{S}^T\vec{k}\tau^2}e^{-\frac{1}{2}i\vec{k}^T\mathcal{S}\vec{v}\tau^2}e^{\frac{1}{2}\vec{v}^T\mathcal{Z}\vec{v}\tau^2} \tag{5.26}$$

The n-D probability density for diffusion is $P(\vec{r}(\tau)) = \frac{1}{\sqrt{4\pi D\tau}^n}e^{-\frac{\vec{r}^2}{4D\tau}}$, where $D = \frac{k_B T}{3\pi\eta d}$ is the diffusion constant; k_B is Boltzmann's constant, T is the temperature of the liquid, d is the diameter of the scattering particles, and η here is the dynamic viscosity of the fluid [86, 50]. So for the integral over the diffusion displacements in Eq. 5.25 we have

$$\int_{-\infty}^{\infty} P(\vec{r}_{dif_j}(\tau))e^{i\vec{k}^T\vec{r}_{dif,j}(\tau)}d^n r_{dif,j}(\tau) = \frac{1}{\sqrt{4\pi D\tau}^n}\int_{-\infty}^{\infty} e^{i\vec{k}\cdot\vec{r}_{dif,j}(\tau)}e^{-\frac{\vec{r}_{dif,j}(\tau)^2}{4D\tau}}d^n r_{dif,j}(\tau) = e^{-Dk^2\tau} \tag{5.27}$$

Putting these into Eq. 5.25, we have (noting that the N terms in the summation are identical)

$$\left|\sum_j \langle E_j(t)E_j^*(t+\tau)\rangle\right|^2 = E_D^4 N^2 \frac{\pi^n}{det(2\mathcal{Z})}e^{-2Dk^2\tau}e^{-\vec{v}^T\mathcal{Z}\vec{v}\tau^2}e^{-\frac{1}{4}\vec{k}^T\mathcal{S}\mathcal{Z}^{-1}\mathcal{S}^T\vec{k}\tau^2} \tag{5.28}$$

Therefore,

$$G(\tau) = \frac{\langle I(t)I(t+\tau)\rangle}{|\langle I(t)\rangle|^2} - 1 = e^{-2Dk^2\tau}e^{-\vec{v}^T\mathcal{Z}\vec{v}\tau^2}e^{-\frac{1}{4}\vec{k}^T\mathcal{S}\mathcal{Z}^{-1}\mathcal{S}^T\vec{k}\tau^2} \tag{5.29}$$

The average velocity is important only at very high velocities ($\vec{v}^T\mathcal{Z}\vec{v} \gg \langle\mathcal{S}_{\alpha\beta}\rangle^2$) [49], where particles will be pass into and out of the beam during the course of a measurement. We can write the diffusion factor as $e^{-q\tau}$, where $q = 2Dk^2$ in the case of no shear; in the presence of shear, q also includes effects such as Taylor Diffusion [87]. This allows us to easily account for the effect of diffusion while fitting our data without worrying about the precise value of q under given conditions. This effective diffusion enhancement is visible in all data,

[2] $\int_{-\infty}^{\infty} e^{-\vec{x}^T\mathcal{A}\vec{x}+\vec{B}^T\vec{x}}d^n x = \sqrt{\frac{(\pi)^n}{\det\mathcal{A}}}e^{\frac{1}{4}\vec{B}^T\mathcal{A}^{-1}\vec{B}}$. This can be verified by applying the unitary transform $a^\dagger a = 1$, where this diagonalizes $\mathcal{A}$, and then performing the integral in eigenspace. Such a transformation does not change the determinant.

explaining the initial non-zero slope of $G(\tau)$, but does not effect the shear measurement. A constant factor G_0 is included to account for detection efficiency considerations, minimum measurement time and noise; its exact value is unimportant. The value of G_0 is obtained during fitting but is not relevant for determining the shear rate. Therefore we may write Eq. 5.29 as

$$G(\tau) = G_0 e^{-q\tau} e^{-\frac{1}{4}\vec{k}^T \mathcal{S} \mathcal{Z}^{-1} \mathcal{S}^T \vec{k} \tau^2} \tag{5.30}$$

which can be easily fit once the tensors in the exponent are evaluated for the geometry at hand. In contrast to previous 3-D theoretical treatment [51], Eq. 5.30 can be used to obtain quantitatively exact shear rate measurements; the unknown factors (q and G_0) are unimportant and all other factors in the equation can be determined independently.

This treatment recovers the previously presented results for 2-D flow [49], with corrections for including the coupling effects. Note that the definition of w used in [49] is in terms of intensity, rather than electric field. In Cartesian coordinates with the water constrained to the x-y plane ($\vec{v} = v_x\hat{x} + v_y\hat{y} + 0\hat{z}$), circular input beam with size w_0 for an input laser perpendicular to the water plane and detector with size w_s at some angle from the input beam, and assuming laminar flow ($\mathcal{S} = \mathcal{S}_{xy} = \frac{\partial v_x}{\partial r_y}$ is the only non-zero component), this is

$$G(\tau) = G_0 e^{-q\tau} e^{-\frac{k_x^2 \mathcal{S}_{xy}^2 w_0^2 w_s^2}{4(w_0^2 + w_s^2)} \tau^2} \tag{5.31}$$

To account for this correction, all shear rates reported in [49] should be increased by 10% (with $w_0 = 141$ μm and $w_s = 386$ μm [88]).

Note that PCS measurement is not sensitive to components of $\mathcal{S}$ involving the velocity perpendicular to the plane containing $\vec{k}$, $\vec{k}_0$ and $\vec{\kappa}$. For example in a CPR, we can eliminate terms involving v_z in our measurement by constraining $\vec{k}$ to be in a ρ, ϕ plane.

5.2.1 PCS Measurements in a Cone & Plate Rheometer

In the laminar limit detailed in Section 5.1, Eq. 5.30 reduces to

$$G(\tau) = G_0 e^{-q\tau} e^{-\frac{k_\phi^2 \mathcal{S}_{\phi z}^2 w_b^2 w_d^2}{4(w_b^2 + w_d^2)} \tau^2} \tag{5.32}$$

Where $k_\phi = \vec{k} \cdot \hat{\phi}$. Note that $G(\tau)$ in this case depends only on the size of the beam and the detector in the $\hat{z}$ direction. For laminar flow we can simply fit Eq. 5.32 to find $\frac{k_\phi^2 \mathcal{S}_{\phi z}^2 w_b^2 w_d^2}{4(w_b^2+w_d^2)}$, which has no unknown parameters except $\mathcal{S}_{\phi z}$. In the event we leave laminar flow, other additive terms in the exponent may appear.

Care must be taken to obtain the proper projection of $\vec{k}$. Neither the incident beam nor scattered beam will generally be along either the $\hat{\rho}$ or $\hat{\phi}$ axes, and so in order to evaluate $\vec{k}^T \mathcal{S} \mathcal{Z}^{-1} \mathcal{S}^T \vec{k}$, we must properly determine k_ϕ. With $\vec{k}$ assumed to be directed in a ρ, ϕ plane, this gives, in terms of either the component vectors or the total vector,

$$\vec{k}_0 - \vec{\kappa} = \frac{2\pi n}{\lambda}(\sin(\psi)\hat{\rho} + \cos(\psi)\hat{\phi}) - \frac{2\pi n}{\lambda}(\sin(\psi+\theta)\hat{\rho} + \cos(\psi+\theta)\hat{\phi})$$
$$\vec{k} = \frac{4\pi n}{\lambda} \sin\left(\frac{\theta}{2}\right)\left(\sin\left(\frac{\pi}{2} - \frac{\theta}{2} - \psi\right)\hat{\rho} + \cos\left(\frac{\pi}{2} - \frac{\theta}{2} - \psi\right)\hat{\phi}\right)$$

where $\psi = \tan^{-1}\left(\frac{R'}{R}\right)$ is the angle the $\hat{\phi}$ direction makes with the incoming beam at the observation point, R being the beam perihelion distance relative to the cone center and R' being the distance past this point of the center of the scattering volume. Then

$$k_\phi = (\vec{k}_0 - \vec{\kappa}) \cdot \hat{\phi} = \frac{2\pi n}{\lambda}\cos(\psi) - \frac{2\pi n}{\lambda}\cos(\psi+\theta) \tag{5.33}$$
$$k_\phi = \vec{k} \cdot \hat{\phi} = \frac{4\pi n}{\lambda}\sin\left(\frac{\theta}{2}\right)\cos\left(\frac{\pi}{2} - \frac{\theta}{2} - \psi\right) \tag{5.34}$$

So we must keep track of R and R' in addition to θ if we are to properly interpret our results. These factors are under the control of the experimenter.

6.0 DESIGN & CONSTRUCTION OF THE APPARATUS

While the static measurements performed in Chapter 4 provide some indication the behavior of the various wetting states, they do not tell the whole story. In those tests, we examined the behavior of single droplets, which may not be a good indicator of how these surfaces behave with regard to bulk water or full immersion. Droplet behavior involves the removal of water, and thus is inherently measuring wetting and de-wetting. Therefore the static tests are useful for applications where water/surface contact is transient, such as for repelling rain or spills. The behavior of surfaces may be different when water is instead continuously flowing along them.

In Chapter 5, we discussed torque and liquid shear in the Cone & Plate Rheometer (CPR), a standard diagnostic device for examining drag in bulk liquids. Commercially produced CPR systems are primarily concerned with measuring shear, strain, and torque of uncharacterized high viscosity fluids, rather than the reaction of fluids to different surfaces. As seen in Eq. 5.3, shear rate is simply related to torque in laminar flow with a smooth cone and smooth plate. This relation is what is used to compute shear rate from torque in commercial systems. Because we are measuring interfaces with unknown properties, and for which we do not have a simple relationship between torque and shear rate, we must utilize an alternative method of measuring shear rate. We utilize Photon Correlation Spectroscopy (PCS).

Commercial systems also depend on the viscosity of the sample to hold the liquid in the gap during high-speed measurements; water is relatively low viscosity and will be flung out of the gap at comparatively low speeds, especially if one of the surfaces is hydrophobic. We also cannot readily see through the uneven surface of water held in place by surface tension. It would be advantageous to hold the water with a transparent tank, allowing us to see into the gap and to hold the water in place at high speeds.

To enable measurements of torque and shear rate with unknown surfaces from low to high speeds, we constructed a our own custom CPR system.

6.1 CONE & PLATE RHEOMETER AND PCS MEASUREMENT SYSTEM

Our custom CPR/PCS system was designed to allow for measurement of both the torque, via a magnetic and optical readout, and the shear rate, via PCS measurements. The physical requirements on our design were:

- It must contain the water in a closed, transparent tank. Then the water cannot be ejected from the gap when surface tension is no longer sufficient to hold it in position, any irregularities in the gap are readily visible (bubbles, etc.), and we can perform for PCS measurements, which require a clear optical path through the gap.
- The torque sensing must be able to register torque in the μNm range.
- The gap must be able to be set with μm accuracy with reasonable uncertainty.
- We must be able to control and readout the relative angle and position of the laser beam and optical detector for PCS measurements (located outside the tank), and adjust their relative positions.

Note that we will avoid taking measurements close to the edge of the cone in order to minimize errors, as edge effects may differ from theory and previous work since we are in full immersion.

6.1.1 Cone Alignment

As is standard practice, a small truncation is present at the tip of our cone, so as to prevent it from rubbing on the lower surface when spun. This truncation is kept small to minimize the irregularity it creates [53]. Our cone is constructed to match the parameters of common commercially available rheometer cones (which were used in some initial testing of our surfaces by our collaborators at Oak Ridge National Laboratory, see Chapter 7.1.1), with a radius of 30 mm and a vertical truncation of 51 μm (0.002 in) [89, 31]. We use cones with $\alpha = 2°$ and $\alpha = 6°$ slopes from horizontal. The cone is rough machined on a conventional lathe and then diamond turned to the exact dimensions needed using custom chucks.

We drive the cone with a stepper motor. In a CPR, it is assumed that the cone is positioned such that if the truncation were not present, the tip of the cone with be exactly

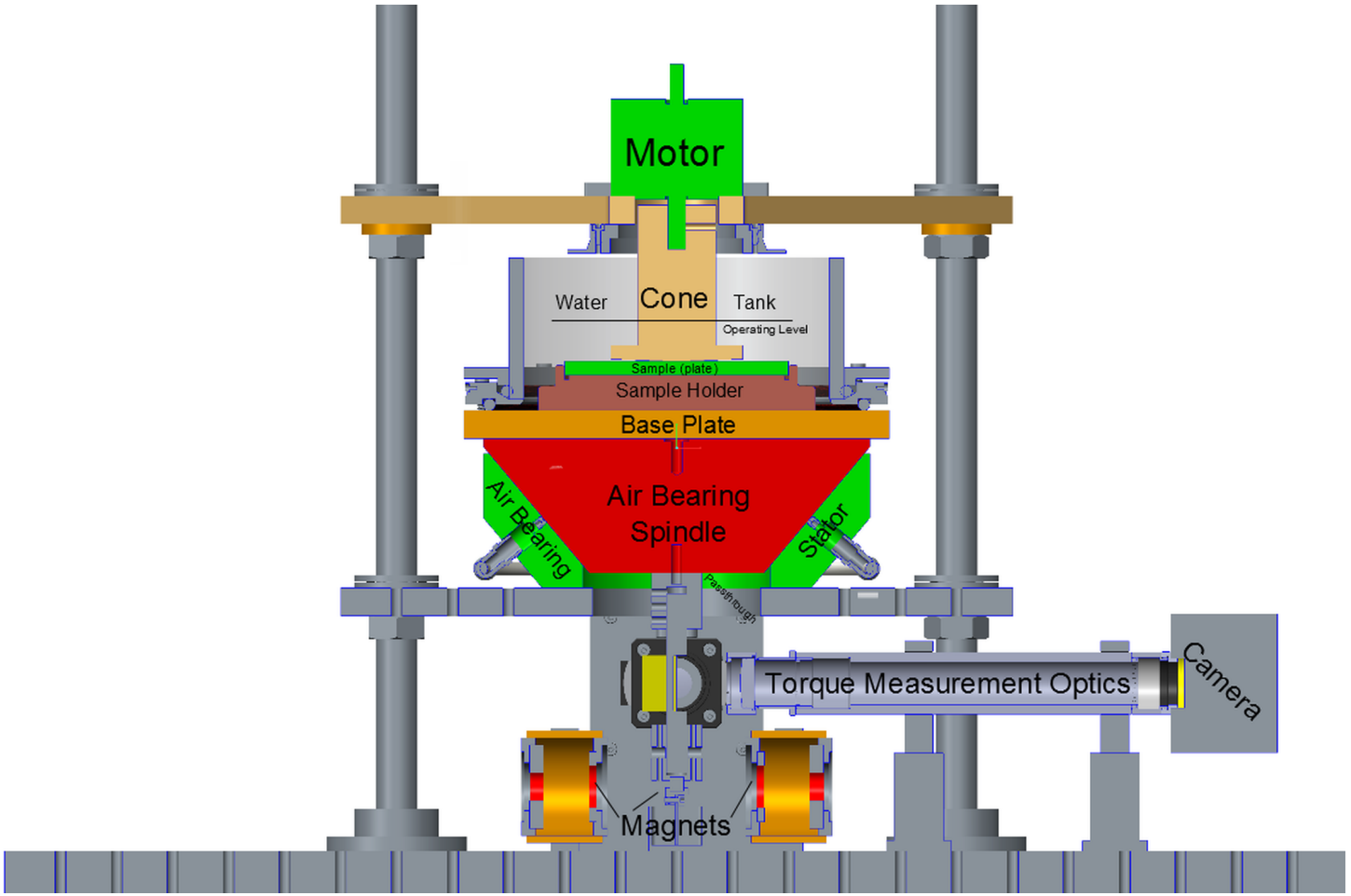

Figure 15: 3D render, in cross section, of the experiential apparatus for measuring torque and shear rate.

at the lower surface [52]. In order to perform this alignment, the cone and the motor are mounted on a movable X-shaped crossbar. This crossbar is connected at each of the 4 ends to 3/4-28 threaded rods with sleeve bearings. This allows the user to move the stage up and down by very fine increments using nuts underneath the bearings. A second pair of nuts pressing on wavesprings from above forms a compression pair around each adjustment point, ensuring that the crossbar cannot vibrate and preventing the sleeves from jamming on a thread as the crossbar is moved, since the weight of the motor and crossbar is very low.

In order to measure the spacing, a circular ring is placed on the upper lip of the cone. This ring is diamond turned such that it rests directly on the lip and the spacing from the top surface of the ring to the plate will be a fixed number when the cone is at the designed distance from the plate. The target spacing for the cone and measurement ring used is 1.74 mm; the exact value of this spacing is unimportant so long as it is known (it can be checked by using a machining standard 0.002 in shim). There are several slots in this ring through which a probe may be dropped to measure the top surface of the sample; we measure the spacing by taking a reading from the top surface, then rotating the ring so the probe will drop through a slot onto the lower surface. This is done as far out as possible on the sample, and well away from the gap, since it slightly mars the sample surface. The ring is solid and is captured by the cone when attached, since making the ring separate so it could be removed would introduce uncertainty into how it was resting on the cone lip; it is raised and secured to the cross plate while the experiment is in use.

A Linear Variable Differential Transformer (LVDT) is used to measure the distance between the upper surface of the ring and the plate. The model selected has a linear range of 2 mm, and is calibrated (using the Diamond Turning Machine's nanometer precision stages) to 1 V/mm (Omega LD320-2.5). By moving between the 4 gaps between the cross plate arms, it is possible to align the cone position to within approximately 10 μm. This alignment is performed using all 4 positions so the cone is no tilted relative to the plate.

6.1.2 Torque Measurement

In high end commercial rheometers, torque measurement is performed using a magnetically suspended drive spindle, by reading the added torque needed to achieve a given speed [89]. This drive spindle system is extremely complex. We instead utilize a simpler method, by allowing the tank to rotate against a calibrated magnetic spring and reading the rotation angle. Reading small torques requires negligible resistance from the sensing apparatus, while simultaneously requiring that the motion of the apparatus be as nearly critically damped as possible. Utilizing SPDT, magnets, and mineral oil, we were able to produce a suitable system. We place our samples in a tank, and allow the entire tank and the water inside it to rotate, because engineering a watertight pass through to allow the plate to move independently would be difficult and would introduce drag and hysteresis from the seal.

6.1.2.1 Air Bearing The active air-bearing is an extremely low resistance system allowing movement with minimal friction [90]. The two faces of the bearing are separated by a continuously replenished air layer, so there is no solid-solid contact and minimal viscous resistance from the air. They require extremely smooth surfaces to function well, which are not easily produced in conventional machining; such surfaces are easily achievable with SPDT [68]. By placing our tank on such a bearing, it will be free to rotate with negligible resistance from the bearing.

Support is needed in both the vertical and the rotational directions in order to allow free rotational motion. Rather than use 2 separate bearings to provide support in each direction individually, a conical bearing design was selected. This allowed the entire system to be supported by a single bearing, making the construction of the system much simpler.

Construction parameters for our cone are dictated by factors such as desired weight capacity and physical size, and available pressurized air. In order to relate these factors, we must look at the gas flow in the bearing. Such flow is well understood in general [90]; we present here the specific case for our conical bearing. The notation used is standard for the topic of bearing engineering and does match that used elsewhere in this thesis; please refer to Fig.16.

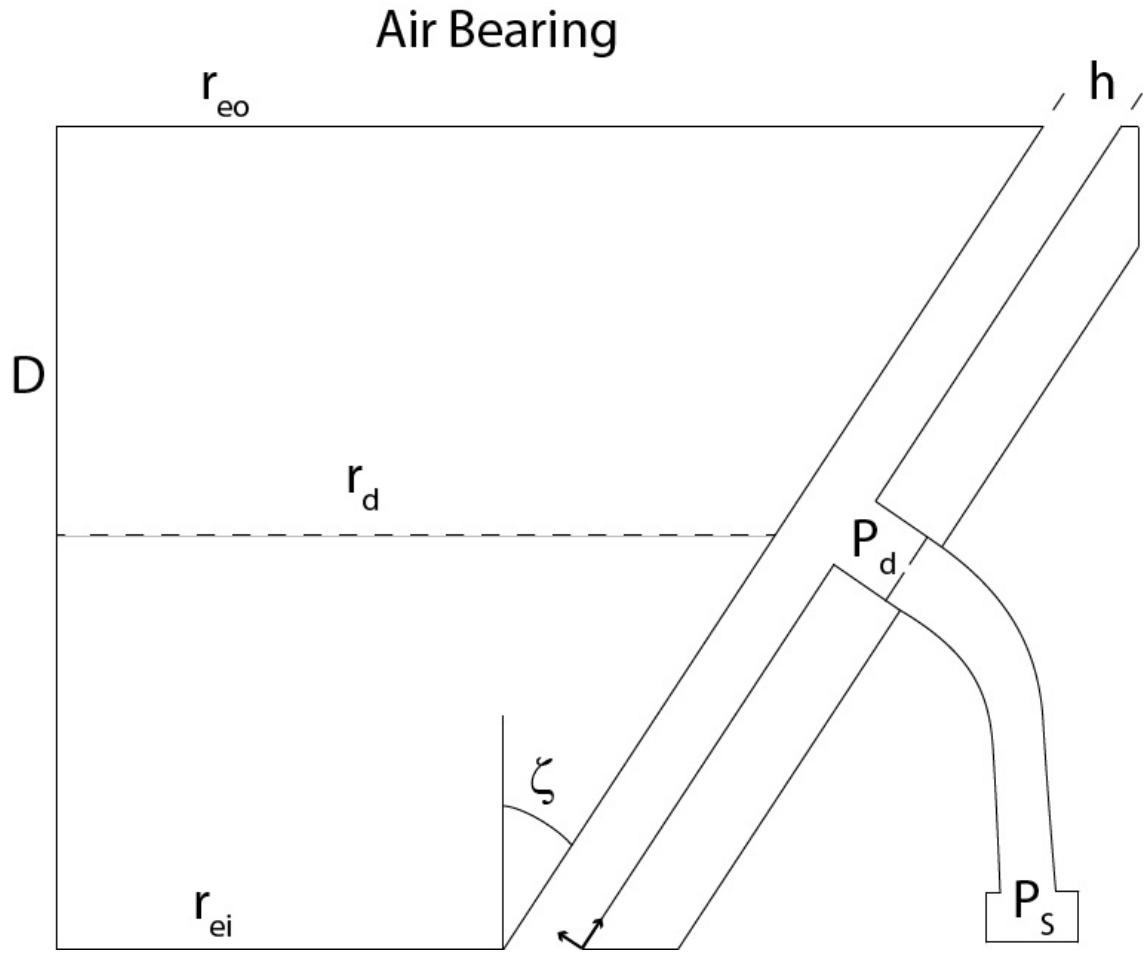

Figure 16: Cross-Section of the air bearing, cut in half at the rotation axis. We show only 1 side as the bearing is symmetrical. D is the total height of the bearing, r_{eo} is the radius of the top of the bearing, r_{ei} is the radius of bottom of the bearing, h is the height of the gap separating the bearing from the stator, ζ is the angle of the bearing from the vertical, P_s is the pressure of the air source and r_d and P_d are the radius and pressure at the dispenser (the place where air enters the bearing).

The following conditions are assumed inside the bearing:

- Frictional forces due to viscous shearing of the gas dominate
- Gas inside the bearing is in laminar flow
- The gas obeys no-slip boundary conditions at the walls

- Pressure on the walls is uniform

The gap between the rotor and the stator can be treated with a small slot of width a and height h going from the bottom to the top of the bearing, where we will construct our total bearing out of a sum these slots around the perimeter of the bearing. Given these conditions, the Navier-Stokes Equation in Cartesian coordinates becomes

$$\frac{\partial^2 v}{\partial y^2} = \frac{1}{\mu}\frac{\partial P}{\partial x} \tag{6.1}$$

where v is the velocity along the bearing ($\hat{x}$ direction) at a point, P is the pressure at that point, and μ is the dynamic viscosity of the gas. $\hat{x}$ the direction along the bearing gap (with the origin at the bottom of the bearing), while $\hat{y}$ is the direction across the gap.

Integrating Eq. 6.1 twice with respect to y, we find that

$$v = \frac{1}{\mu}\frac{dP}{dx}\frac{y^2}{2} + Ay + B \tag{6.2}$$

where A and B are integration constants. From the no-slip boundary condition, we have $v(y=0) = 0$, so $B = 0$, and $v(y-h) = 0$, so $A = -\frac{1}{2\mu}\frac{dP}{dx}h$. Therefore

$$v = \frac{y(y-h)}{2\mu}\frac{dP}{dx} \tag{6.3}$$

Which is parabolic in y.

If we now look at the mass flow rate $m = \rho \int_A \vec{v}\cdot d\vec{A}$ down the slot, where ρ is the density of the gas, we find

$$m = \rho a \int_0^h v dy = \frac{\rho a}{2\mu}\frac{dP}{dx}\int_0^h y(y-h)dy = -\frac{h^3 \rho a}{12\mu}\frac{dP}{dx} \tag{6.4}$$

where a is the perpendicular size of the region ($\hat{z}$ direction). Because we are working with a conical bearing, $a = r\Phi$, where r is the radius of the bearing at that point and Φ is the angular extent of the slice of the bearing we are examining. The radius at the bottom of the bearing is r_{ei}, and that at the top is r_{eo}. We further see that $x = (r - r_{ei})/\sin(\zeta)$, where ζ is the angle of the bearing from vertical. Substituting, we see that

$$m = -\frac{h^3 \rho r \Phi \sin\zeta}{12\mu}\frac{dP}{dr} \tag{6.5}$$

Because we are in laminar flow, we may treat this as an ideal gas, so $PV = nRT$, where V is the volume of the gas, n is the number of moles of gas, R is the molar gas constant, and T is the absolute temperature. We can rewrite this in molar form as $P\tilde{M} = \rho RT$, where $\tilde{M}$ is the molar mass. Then

$$m = -\frac{h^3 \tilde{M} r \Phi \sin\zeta}{12\mu RT} P \frac{dP}{dr} \tag{6.6}$$

Solving for PdP, we have

$$PdP = -\frac{12\mu RTm}{h^3 \tilde{M} \Phi \sin\zeta} \frac{dr}{r} \tag{6.7}$$

We must now pause before integrating this equation. We insert gas at some dispenser pressure P_d, at a location midway up the bearing. We notate this location with the radius of the bearing at that point r_d or the distance up the slot x_d, where $r_d = r_{ei} + x_d \sin(\zeta)$. From this location, the gas will flow away from the dispenser in both directions, decreasing in pressure as it moves through the bearing gap. When flowing in the negative $\hat{x}$ direction, that mass flow rate will be negative, however it is more convenient to consider the magnitude of the flow rate and handle the sign externally. Performing the integration, we find that

$$P^2 = P_d^2 \mp \frac{24\mu RTm_{\pm}}{h^3 \tilde{M} \Phi \sin\zeta} Log_e \frac{r}{r_d} \tag{6.8}$$

Where the upper sign indicates flow in the positive $\hat{x}$ direction and the lower sign indicates flow in the negative directions. We notate the magnitude of the mass flow rate $m_{\pm}$ to indicate that it is not necessarily the same in both directions. We note here that because of the nature of natural logarithms, this is a decreasing function in both directions. If we now go to the ends of the bearing, where P_e is the external pressure outside the bearing (in general atmospheric pressure), and solve for the mass flow rates in both directions (in terms of $P_d^2 - P_e^2$, which is positive), we find

$$m_+ = \frac{(P_d^2 - P_e^2) h^3 \tilde{M} \Phi \sin\zeta}{24\mu RT Log_e \frac{r_{eo}}{r_d}} \qquad m_- = -\frac{(P_d^2 - P_e^2) h^3 \tilde{M} \Phi \sin\zeta}{24\mu RT Log_e \frac{r_{ei}}{r_d}} \tag{6.9}$$

If the mass flow rate, and thus the pressure gradient, are different depending on the direction of flow, the bearing will not be stable. Therefore we set the mass flow rates to be equal in both directions; then $-Log_e \frac{r_{ei}}{r_d} = Log_e \frac{r_{eo}}{r_d}$, or more simply $r_d = \sqrt{r_{ei} r_{eo}}$. This fixes the

location of the dispensers relative to the other dimensions. Then the total flow rate M would be

$$M = \frac{(P_d^2 - P_e^2)h^3\tilde{M}\Phi\sin\zeta}{24\mu RT}\frac{Log_e\frac{r_{ei}}{r_{eo}}}{Log_e\frac{r_d}{r_{ei}}Log_e\frac{r_{ei}}{r_d}} \tag{6.10}$$

where M is the total mass flow rate into the bearing through a single orifice. Remembering that $m_+ = m_- = M/2$, and removing the variable having to do with the opening we are not dealing with,

$$P^2 = P_d^2 \mp (P_d^2 - P_e^2)Log_e\frac{r}{r_d}\begin{cases} Log_e\frac{r_{eo}}{r_d} & \text{for } r \geq r_d \\ Log_e\frac{r_{ei}}{r_d} & \text{for } r < r_d \end{cases} \tag{6.11}$$

where again the upper case is for positive flow and the lower is for negative flow. Note that this derivation is for a region with a single dispenser, so rather than letting Φ go to 2π, there must be N regions of equal size that are vector-summed to get the total force, where N is the number of orifices. This is the pressure applied perpendicular to the bearing surface.

It should be noted that the dispensers are generally very small orifices in order to decrease M. Thus P_d is very slightly smaller than the pressure provided by a compressor or other source, P_s. Since the orifice is circular, we use the Navier-Stokes Equation in cylindrical coordinates $\frac{1}{r}\frac{\partial}{\partial r}(r\frac{\partial v}{\partial r}) = \frac{1}{\mu}\frac{\partial P}{\partial z}$, where r is the radial directional with the original in center of the orifice. The solution with no slip conditions yields $v = -\frac{1}{4\mu}\frac{\partial P}{\partial z}(R'^2 - r^2)$, where R' is the radius of the orifice. Then $m_O = M = \int_0^{R'} v2\pi r dr = -\frac{\rho\pi R'^4}{8\mu}\frac{\partial P}{\partial z} = -\frac{\pi R'^4\tilde{M}}{8\mu RT}P\frac{\partial P}{\partial z}$, where we have again used the ideal gas law and we note that the flow through the orifice must be the same as the total flow in the bearing. Then the pressure difference from going through the orifice is

$$P_d^2 = P_s^2 - \frac{16\mu MRT}{\pi R'^4\tilde{M}}(l + h) \tag{6.12}$$

Where l is depth of the orifice. We include the cylinder inside the bearing directly above the orifice because as the bearing spacing shrinks the constriction at the end of the orifice will increase.

We can now simply calculate the net force applied to the rotor in the vertical direction, $F_w = N\cos\zeta\int\vec{P}\cdot d\vec{A} = \frac{N\Phi\cos\zeta}{\sin\zeta}\int Prdr$, where the integral must be done numerically. We note that the net force in the horizontal direction is zero (because oppositely located dispensers produce oppositely directed horizontal force), but a horizontal stiffness can be found

by considering the derivative from a single outlet with respect to h.

For our bearing, we selected $r_{eo} = 3$ in, $D = 2$ in, $N = 6$ dispensers, and $\zeta = 40°$. This means that the air inputs needed to be 0.8 in from the base of the bearing, and with an air gap of $h = 1\mu m$ the bearing can support a total mass (including the mass of the rotor) of approximately 5 kg. This load capacity is more than sufficient, and was selected to allow for a wide safety margin and so there would be plenty of capacity for any future uses.

6.1.2.2 Magnetic Torque Readout If unrestrained, the air-bearing would turn freely under any applied torque. While the speed at which it turns is a function of the applied torque, this would be heavily effected by the flowing liquid inside the tank but outside the gap, and would also be vulnerable to crashing. We instead provide a calibrated magnetic spring, such that the bearing rotates to a fixed angle; that angle then allows us to calculate the torque.

As any solid contact would introduce friction into the system, the most logical resistance is a magnetic torque. A permanent NdFeB block magnet ($\frac{1}{16} \times \frac{1}{16} \times \frac{3}{16}$ in) is placed on a shaft hanging from the bottom of the bearing (the shaft axis is on the bearing axis of rotation). A pair of NdFeB ring magnets ($1\frac{1}{4}$OD $\times$ $\frac{3}{4}$ID $\times$ $\frac{1}{8}$ in) in a Helmholtz configuration on the table generate a stable magnetic field. This provides a simple magnetic spring from the dipole torque $\vec{\tau} = \vec{\mu} \times \vec{B}$, or more simply $|\tau| = \mu B \cos(\theta) = \beta \cos(\theta)$, where μ is the dipole moment of the central magnet and B is the field it is immersed in. We paramaterize this with β since for real magnets the field produced by the rings will have some non-uniformity over the expanse of the block magnet, and the dipole moment for an extended object is not simply calculated. β must be found by calibrating the system anytime the ring spacing is changed. The torque applied to the sample by the fluid is found by reading the angle at which the bearing is at equilibrium under this magnetic spring.

It should be noted that this torque is a simple restoring force; the bearing will oscillate as a driven underdamped harmonic oscillator about the equilibrium when the cone is rotating. In order to easily read out the steady applied torque (as well as minimize the occurrence of major oscillations which endanger the bearing), it is necessary to apply additional damping so as to force decay to equilibrium. This is achieved by hanging a paddle off the shaft holding

the magnet; this paddle is placed in an appropriate damping fluid which will ideally damp transient motions, while leaving steady forces unaffected. This fluid must have a high enough viscosity to bring us near critical damping, without appreciable additional drag or hysteresis. Because avoiding additional drag and hysteresis was more important than rapid damping, a damping fluid consisting of mineral oil ($\eta \approx 2.2cP$) with a damping time on the order of minutes was experimentally chosen in preference to stronger but more hysterically prone and/or non-Newtonian damping fluids (such as Sugar water, Mollasses, or Corn Syrup). Therefore one must wait 3 minutes after any change in applied torque for equilibrium to be reached before a reading is taken. Viscosity was measured by dropping a ball of radius r_{ball} through a tube filled with the fluid; then viscosity is $\eta = \frac{2r_{ball}^2(\rho_{ball}-\rho_{fluid})g}{9v_{term}}$, where v_{term} is the terminal velocity of the ball.

6.1.2.3 Moire Pattern A moire pattern is used to read the angle. The moire pattern consists of a 50/50 clear/black sinusoidal pattern of lines, with a $\frac{\pi}{2}$ phase shift forming a central clear line and a period of 0.245 mm. Our moire grid pattern is 2 in in diameter, printed at high DPI on a transparency and then cut out and fixed to a diffuser in a rotational optical mount. This pattern is reflected off of a mirror attached the shaft holding the bar magnet, and the reflection is recorded with a CCD camera (Amscope MU300 - 1/2" Sensor, 2048x1536 Resolution, 3.2 μm square Pixels). Using the long direction of the sensor for maximum range, this gives 6.55 mm of total readable displacement.

This image is vertically averaged, creating a 1-D array of pixel values. An fft of the data is then performed, and this is compared to a simulation of the fft of the grid at each possible position using chi-squared fitting to select the best match. Then displacement of the pattern from center is accurately determined by checking what the displacement was for the chosen simulation. Note that the simulations take a long time to be generated, but can be reused so long as the grid and camera are not moved (if either is moved, the apparent period of the grid in the image can change).

In order to translate the horizontal displacement into an angle, we trace the central ray. Looking at Fig. 17, we see that $\frac{\pi}{4} = \epsilon + \theta$ and $\epsilon + \phi = \theta + \frac{\pi}{4} - \psi + \phi$ which tells us that $\theta = \frac{\psi}{2}$. Examining the ray between the final lens and the CCD, we see that $\tan(\psi) = \frac{h}{f}$. So

the angle of rotation is simply

$$\theta = \frac{\tan^{-1}(h/f)}{2} \tag{6.13}$$

Where f is the focal length of our imaging lenses and h is the distance of the bright from center. In this way, the angle of rotation of the mirror can be determined to within 0.001°, relative to a chosen 0 point. This requires that the strength of the constraining magnetic field (the spacing of the ring magnets) be such that at the maximum torque of interest the central bright will still be visible on the CCD. Added range can be achieved by setting the 0 of the system with the central bright reflection at one end of the CCD and only applying torque in one direction.

The torque system must be calibrated in order to determine β. Two simple methods are available. In one, a string is wrapped around the hanging axle and a weight is hung from the other end. The bearing will rotate until the torque from the magnetic field is equal to the applied torque from the weight. The torque exerted on the axle is then $\tau = mgr$, where m is the mass of the weight, g is gravitational acceleration, and r is radius of the axle. The calibrating equation is then

$$mgr = \beta \sin(\theta) \approx \beta\theta \tag{6.14}$$

where we can in general use the small angle approximation due to the small size of the angles involved. In order to more accurately obtain a value for β, we take this reading for multiple masses and fit a line to $\sin(\theta) = mgr/\beta + a_0$; using the slope serves to average out measurement errors. This measurement requires running the string over small bar or a pulley to transition from the horizontal to the vertical direction, which may induce a small amount of frictional hysteresis, so careful selection of the string and bar/pulley are needed to minimize this effect.

We can also obtain calibration by examining the free oscillation of the bearing in the magnetic field. This must be done carefully to avoid accidentally damaging the bearing. In order to use this method, the moment of inertia I of the entire moving assembly must be known (we remove the damping vane, which is so light as to be negligible). Net torque on the bearing is $\tau = I\alpha = \beta \sin(\theta) \approx \beta\theta$, where $\alpha = \ddot{\theta} = \frac{d^2\theta}{dt^2}$. We then have $I\ddot{\theta} = \beta\theta$, so

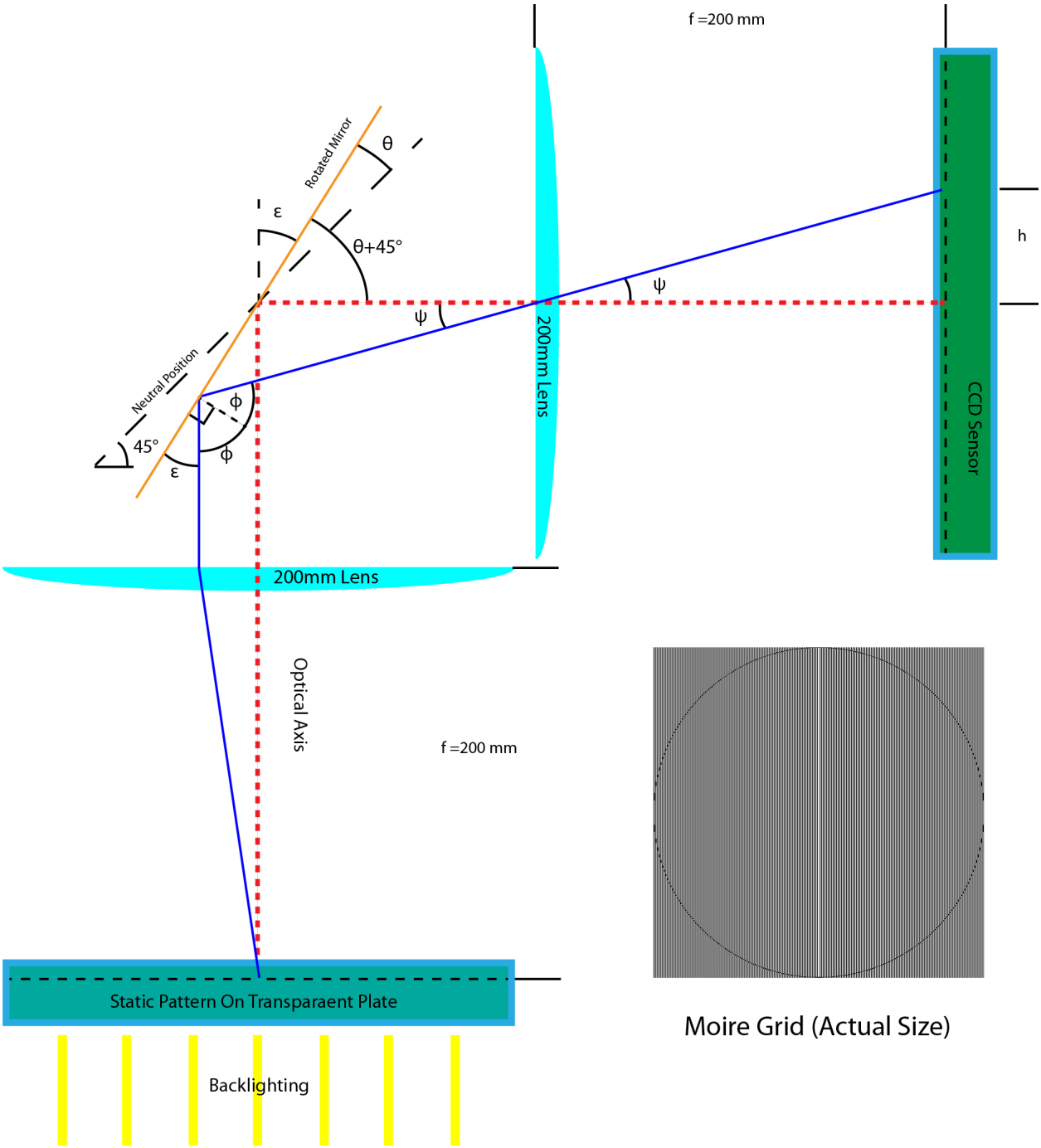

Figure 17: Diagram of optics with ray tracing, and image of Moire Grid (grid will only print accurately on a 1200 dpi or greater printer). Mirror is on the shaft hanging from the rotor.

$\theta = A\sin(\omega t + \delta) + O$, where $\omega^2 = \beta/I$, so

$$\beta = I\omega^2 \tag{6.15}$$

By fitting the angle as a function of time, we can obtain ω and thus β. This method is faster and easier to perform, and lacks the systematic issues of the other method, so once we confirmed that both methods yielded the same calibration (to within error), we used this second method exclusively.

6.1.3 PCS Measurements

The additional requirements on our CPR in order to perform PCS measurements were minimal. The only added requirements were that the sample be raised high enough inside the tank that a laser could be passed through the rheometer gap in plane and that the cone angle be high enough that, at the measurement point, the gap is large enough for the laser beam to pass through with as little clipping as possible by either the cone or the plate. This second point necessitated the use of a 6° cone for these measurements, the highest angle we could reach without rendering the theory discussed in Chapter 5.1.1 invalid. Simple optical stages and rods allowed us to achieve the needed degrees of freedom to control the laser and detector positions. Our system was designed to allow for manual 3-D linear translation/tilt and horizontal rotation of the detector, as well as horizontal rotation, vertical tilt, and vertical displacement of our laser source.

To measure the shear tensor, we direct a Gaussian laser beam from a HeNe laser (6 mW, $\lambda = 632.8$ nm, beam diameter $2w = 0.81$ mm) into the cylindrical glass tank and through the cone-plate gap of our CPR. The tank is filled with water in which we have suspended a low concentration of spheres of diameter d=0.4 μm, ultrasonically dispersed, as scattering particles (they are small enough to follow the local velocity; the Stokes number is much less than unity [91]). The concentration of particles is kept low to avoid multiple scattering. With this incident intensity the photon counting rate is of the order of 750 kHz to 1.5 MHz (when shielded from ambient light) at a scattering angle of 20.5°. The measurement count rate will increase if unshielded, but as this light will be uncorrelated the measurement of shear is insensitive to ambient light levels.

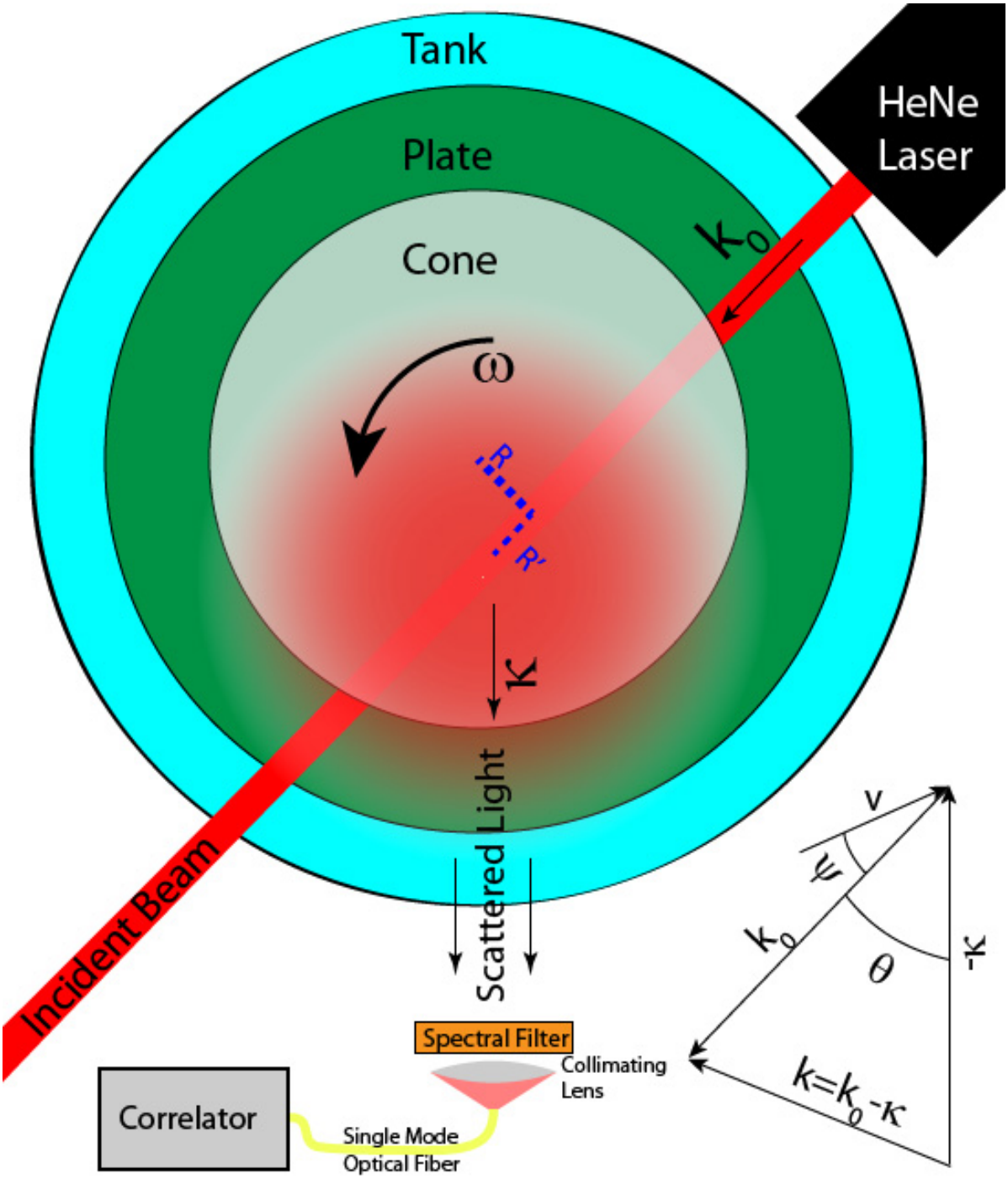

Figure 18: Overhead schematic view of a PCS measurement in a Cone & Plate Rheometer.

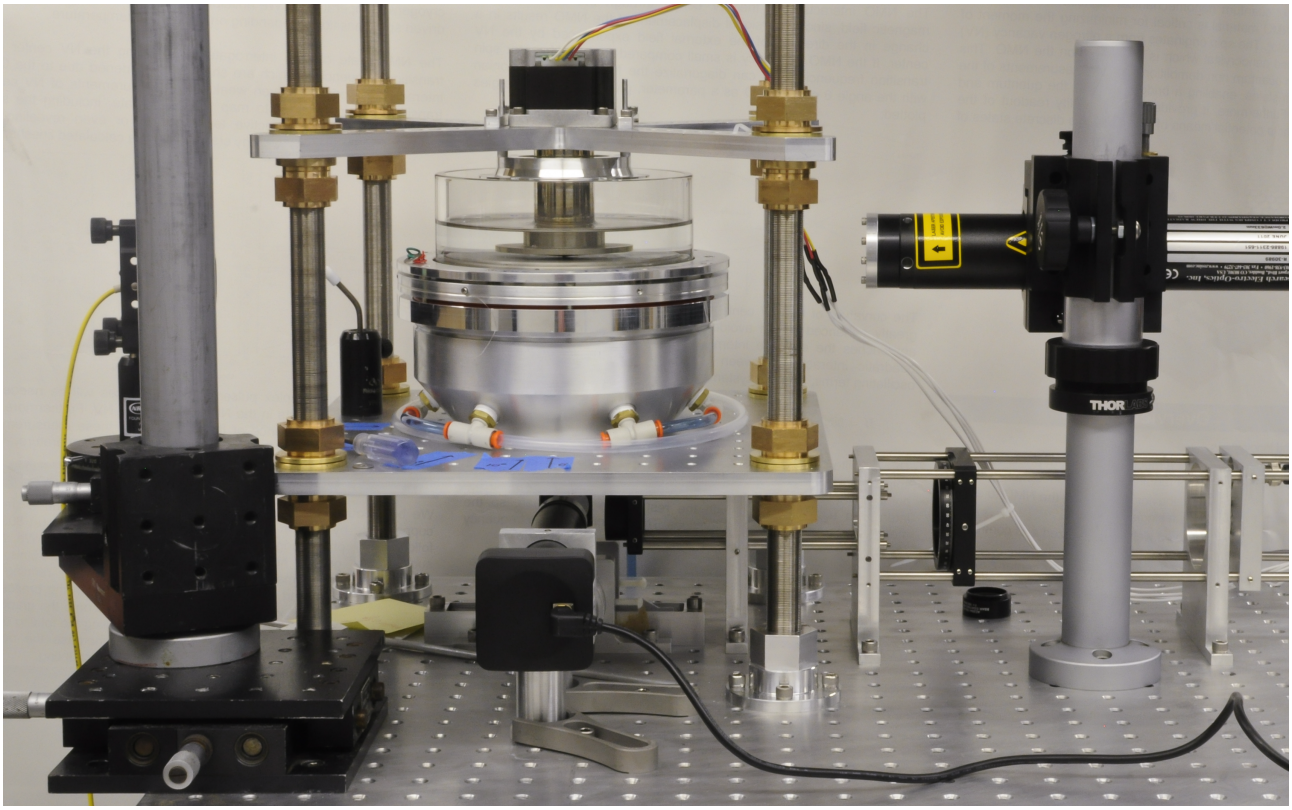

Figure 19: Picture of the Dynamic Measurement system as currently configured.

We take measurements by orienting the beam and receiver in the horizontal plane, parallel to the plate. The collimating lens (Thorlabs TC12FC-633) receives the scattered light, which is coupled into the single-mode optical fiber (Thorlabs SM600), so that the direction of the received light is well defined. The coupled light is transmitted to an avalanche photodiode based single photon counting module (Excelitas SPCM-AQRH-14-FC). The SPCM signal is fed into an ALV-5000 autocorrelation card that converts the intensity $I(t)$ into an intensity autocorrelation function $G(\tau)$. The effective sizes w_c and w_d of the detector can be found by measuring the dimensions of a laser beam sent backward through the fiber and out through the collimator.

Readout of the scattering angle and the location of the scattering volume was achieved by running a beam back through the detector's optical fiber. An image was taken from

above using a Nikon D5000 equipped with a 30mm fixed focal length lens (to allow for photographing at $f1.8$ for low light sensitivity); the camera was placed on a transparent plastic plate on top of the four support rods. Finding the angle and positions required manual analysis of the resulting image (see for example Fig. 33). Vertical alignment between the laser and the detector simply involved maximizing the count rate for the scattered light. Setting the height and tilt of the input beam so it passed through the gap parallel to the surface and without clipping was done manually by operator's best judgment (quantitative methods such as maximizing the transmitted power tended to favor reflection), which introduces the possibility of experimental error.

6.1.4 Design Flaws/Issues with the current system, and Future Improvements

The current iteration of the system has several issues which make it difficult to use, or which could be improved upon in future refinements.

- The LVDT measurement points are currently between the crossbar limbs. This means that measurements with the LVDT do not isolate the two rotation axes of the crossbar, making adjustment slightly more difficult. Placing holes in the crossbar itself, so the measurement locations are in line with the threaded rods, will make adjustment easier.
- The adjustment of the laser angle and position is difficult and time consuming. The stages must be set to a position, a picture taken, and then the picture manually analyzed in order to get the current locations; these action must be repeated until the desired position is reached. This can take 5 min or longer per positioning attempt; the total alignment process can sometimes require hours due to interaction with the curvature of the tank making it hard to judge exactly how the beams will move with a given adjustment. A more efficient means of adjustment is needed.
- The adjustment of the height of the laser in the gap and of the tilt of the laser so as to be parallel to the sample surface are both performed by eye by the operator. This leads to the possibility of experimental errors either from imperfect leveling or accidental clipping. Adjusting this by maximizing the transmitted power was found to favor reflecting off the cone rather than minimizing clipping.

- Currently, the camera for taking the image of the lasers is not fixed, merely put on a plate that is placed on top of the threaded rods. A fixed solution may improve the speed of the alignment, and possibly allow for automation.
- There is a limited field of view from above due to the crossbar, the motor, and the cone. Some scattering angles cannot be tested without rearranging both the laser and the detector, as one or both beams are not visible from above. An alternative method of measuring the intersection location and the scattering angle may increase efficiency.
- On samples which possess an air layer, bubbles can form during immersion or can transfer to the surface from the cone or the alignment ring. This makes the air layer loading inconsistent, greatly increasing the systematic errors in both torque and PCS measurements. While this is partly a property of these materials, developing methods for minimizing this variability will increase repeatability.
- Bubbles attached to either the surface of the sample or the cone, passing through or permanently present in the beam path, will disrupt PCS measurement by scattering the beam. This can require disassembling and reassembling the apparatus to remove the bubbles, or can make it impossible to take usable readings at some speeds if previously fixed air bubbles become mobile due to increasing shear.
- Because the air bearing is constructed using screw-in orifices sealed with teflon tape, the airflow is not completely uniform inside, leading to a very slight constant torque. This is compensated for by the fact that torque measurements require zeroing, which includes this slight offset, but an alternate method for constricting the airflow may achieve better uniformity.
- The mineral oil used for damping oscillations was selected as the best out of the materials that were tested. A fluid with more ideal damping characteristics may be found with more exhaustive testing.
- The ALV-5000 is an older correlator system, and requires a Windows 2000 system to run it as it uses the deprecated ISA slot. We used remote access from a newer computer via VNC and graphical recognition via the Sikuli Python package in order to automate the measurement process. A newer commercial correlator or a custom built solution will allow for greater ease of use.

- The ALV-5000 has several limits on functionality, including a minimum averaging time of 2 s, which prevents the gathering of very short time data, and a maximum automated repetition rate of 20 runs, which prevents gathering very large data sets without manually restarting after 20 cycles and creating a time gap. A newer commercial correlator or a custom built solution will mitigate these issues.
- On our grooved samples, it is desirable to scan horizontally over the surface when performing PCS measurements, in order to spatially resolve the effects of the patterning (see chapter 7.2). This capability is not included in the current PCS optics setup; the input laser is fixed with regard to linear translations in the horizontal plane and all translation and rotation stages are manually operated. Both the input laser and the detector stage will need to be equipped with automated positioning stages to allow for these spatially resolved measurements, and a method for reading the scattering angle and the location in an automated fashion (accounting for tank curvature effects on the angles) will also be needed.

7.0 FLUID DRAG ON PATTERNED SURFACES

Using our Cone & Plate Rheometer (CPR) system, we measure how drag is effected by multiscale surfaces and changes in surface wetting state. Our samples have structure on two length scales: microscopic spikes and micro to millimeter scale concentric grooves. Our surfaces can also be switched between the Cassie-Baxter and the SLIPS/SuperSLIPS (depending on sample geometry) state in the absence or presence of silicone oil. We explore changes in drag behavior caused by varying the larger scale features (groove depth, groove angle) and the interface type (Superhydrophobic, SLIPS/SuperSLIPS) of our samples. We do not vary the characteristics of our microscopic spikes, as this has been explored before.

Drag reduction via surface modification has been studied on some Superhydrophobic materials, but not in a consistent fashion; measurements have been taken in a wide variety of fashions, including using strips glued to a couette cylinder [30], flowing water through a channel made of Superhydrophobic material [35], and by placing a sample in a CPR [36]. By measuring a large parameter space consistently, we hope to be able to more simply compare the effect of different surface modifications. Drag measurements in bulk fluids have never been performed on SLIPS or SuperSLIPS, so these measurements will give the first indications as to whether these surfaces are useful for drag reducing applications.

7.1 TORQUE MEASUREMENTS

Our primary method for quantifying the drag reduction is via torque measurements taken with our CPR system. We compare the torque on a control sample to that on our modified surfaces. This gives gives an average reading of the force exerted on a large area of material by a fluid.

When discussing the data, we will refer to samples as X-Y Z, where X is the groove angle in degrees (from the horizontal), Y is the groove depth in mm, and Z is SH for Superhydrophobic, SLIPS for SLIPS, or SSLIPS for SuperSLIPS.

7.1.1 ORNL tests

A selection of samples (flat bare aluminum control, 45-10 SH, 45-100 SH, and 45-1000 SH) were prepared in our laboratory at The University of Pittsburgh and then tested at the Center for Nanophase Materials Science at Oak Ridge National Laboratory by our collaborator, Dr. Charlotte Barbier. Torque was measured using a commercial CPR (TA Instruments AR 2000) with a 2° cone having a radius of 30 mm and a vertical truncation of 51 μm (parameters of our custom system were chosen to match). These tests were performed before the work detailed in Chapter 4. Because the commercial system lacked a tank, the plate holding the sample was constructed with a slanted lip to help retain the water. Water was pipetted onto the sample, then the cone was lowered into position with an automated positioning system, and then excess water was removed if needed. Measurements were performed from 2 to 6 rad/s with a 0.5 rad/s increment, then from 6 to 70 rad/s with a 4 rad/s increment (or as high as could be managed before water was ejected from the gap).

These measurements show that the grooving produces a measurable change in drag, and that this change varied with groove depth (see Fig. 20). 1000 μm grooves were more effective in the laminar regime but drag reduction rapidly decreased until it was even with 10 μm grooves as turbulence set in. 100 μm grooves gave a fairly even 15% reduction through the entire range of measurement (see Fig. 21) [31].

7.1.2 Comparing Superhydrophobic and SLIPS/SuperSLIPS behavior

To gain an understanding og the effect of groove angle, as well as to examine SLIPS and SuperSLIPS samples (which we had not yet begun studying when the measurements were taken at Oak Ridge), we prepared a new set of samples for testing in our custom CPR (detailed in Chapter 6). We did not test every sample geometry that was examined in chapter 4, as this would require an inordinate number of samples, and it was also likely that many of the geometries would show similar behavior, as they did in drop testing. A trio of representative geometries were chosen instead. For control purposes, a flat aluminum plate and its Superhydrophobic and SLIPS analogues were examined. To represent a SLIPS on a multiscale surface, 45° grooves were examined, as they are steep enough to be significantly

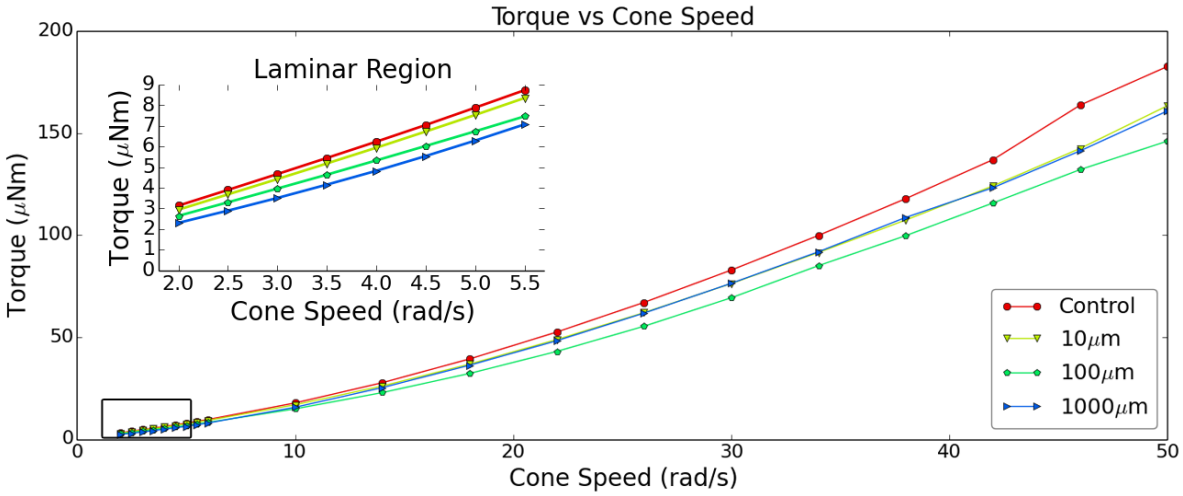

Figure 20: Measurements of 45° grooved samples with varying groove depth taken at Oak Ridge National Laboratory. Inset shows a closeup of the laminar region.

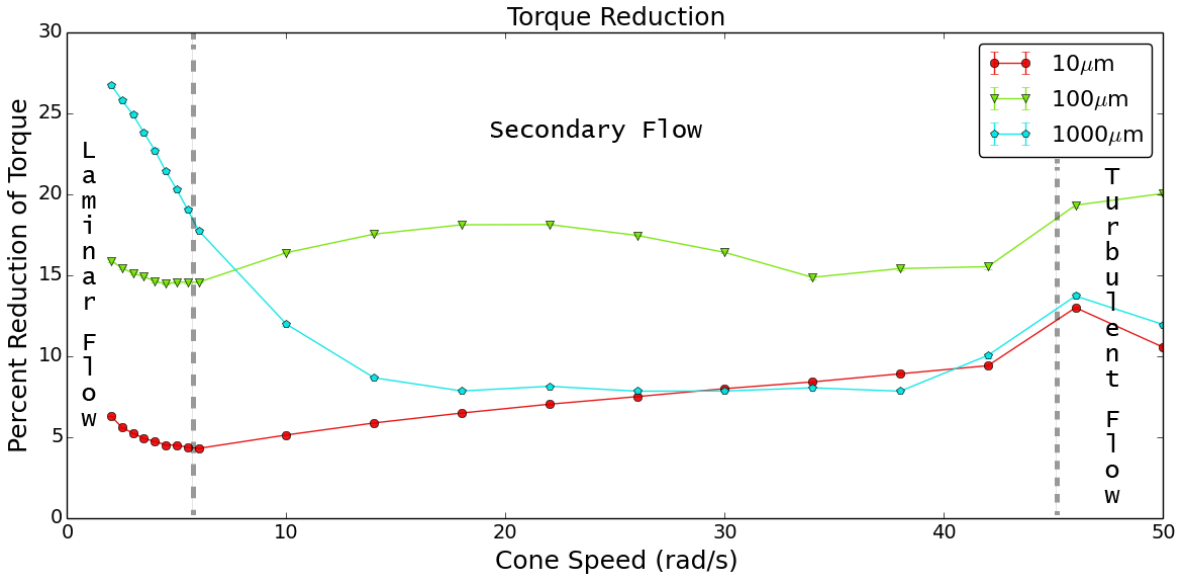

Figure 21: Reduction in torque compared to flat control for 45° grooved samples with varying groove depth taken at Oak Ridge National Laboratory.

different from flat samples, but too shallow to become SuperSLIPS when oil coated. These samples also allowed us to compare our system with the commercial one. Finally, 75° grooves were examined as they will become SuperSLIPS when coated with oil.

Grooved samples were cut to depths of 20 mm, 100 mm, and 500 mm and cut such that adjacent grooves met at the surface of the sample. Our system was designed to utilize 4 in samples in order to mimic the standard industrial rheometer used by Oak Ridge; this required that coating of SLIPS samples with a thin layer of oil be performed at 8 kRPM for 2 min, rather than the 10 kRP for 25 s as in Chapter 3 (the size made it impossible to safely spin at the higher speed). As can be seen from Fig. 8, the difference between these speeds in not significant.

Superhydrophobic samples, 75-500 SLIPS, and 75-100 SLIPS all displayed a visible air layer when immersed, showing that samples were achieving their respective Cassie-Baxter state, while all other samples (including 75-20-SLIPS; we presume this sample is acting as a SLIPS) did not.

Our measurements were taken using our custom CPR, from 0 to 10 rad/s with a 1 rad/s increment, then from 10 to 50 rad/s with a 5 rad/s increment. A 2° cone is used; secondary flow began at 5.5 rad/s and full turbulence began at 44 rad/s (at the edges of the cone).

Torque measurements taken with the tank filled to a fixed level are shown in Fig. 22. We render the data as percentage reduction of torque, relative to the flat aluminum control, shown in Fig. 24. We can clearly see from these graphs that 45-500 SH has the best torque reduction in secondary and turbulent flow at about 27%, followed closely by 45-100 SH with about 24% and 75-500 SH with about 20%. Looking closely at the the laminar regime (Fig. 23), we see 45-500 SH is still best, but with 75-500 SH having slightly better drag reduction than 45-100 SH. Most samples did not exceed 10% reduction at any point.

The torque is quite a bit higher than anticipated analytically, even in laminar flow. This is due to added torque on the outer surface of the tank, which proved to be a larger effect than anticipated. We are unsure how much of the measurement was due to the sample and how much is due to the tank.

In order to mitigate this issue, additional measurements were taken by completely draining the tank via pipet as soon as the full tank measurement were complete (without removing

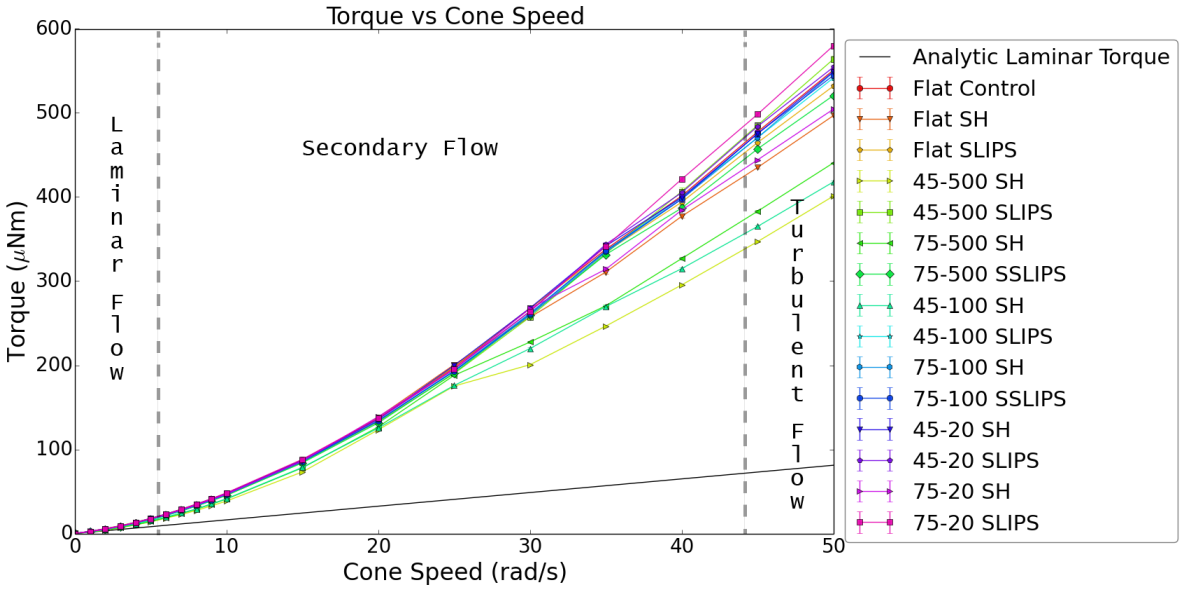

Figure 22: Torque Measurements with a full tank. Note that all measurements are well above analytic expectations.

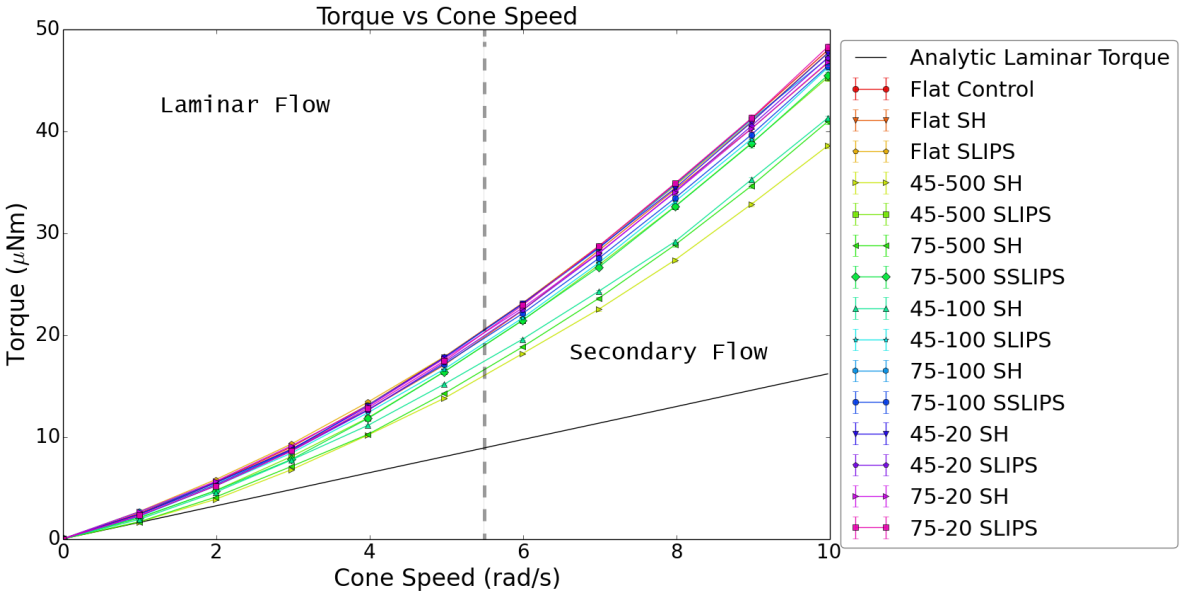

Figure 23: Torque Measurements with a full tank in Laminar flow.

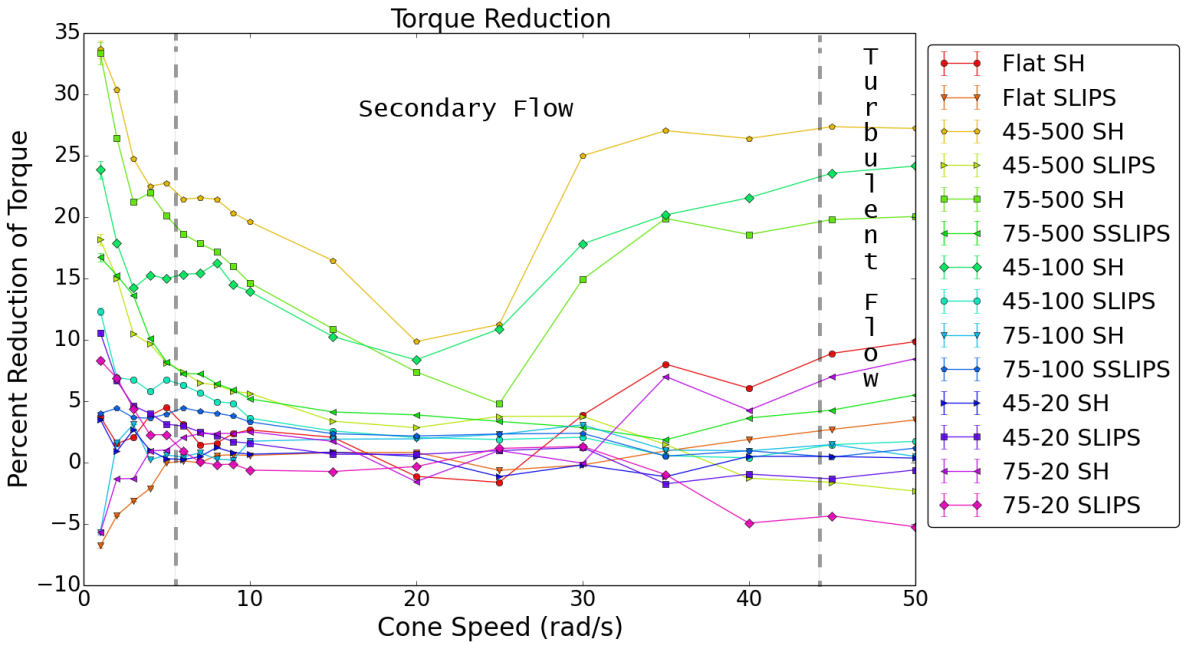

Figure 24: Percentage drag reduction with a full tank.

the sample or changing any other factors), leaving in place only the liquid trapped between the cone and the plate by surface tension. This more closely resembles traditional CPR measurements, and has the disadvantage that measurements can only be taken until the liquid is thrown out of the gap.

Torque measurements with the CPR in this 'minimal water' configuration can be seen in Fig. 25 (lines end at the highest speed before water was ejected from the gap). We look closely at the laminar region in Fig. 26. We again render the data as percentage reduction of torque, relative to the flat aluminum control, shown in Fig. 27. We clearly see that 45-500 SH gives the highest drag reduction in secondary flow at 30%, and retains water longer than most other samples, as before. 45-500 SLIPS, 45-100 SLIPS, 45-20 SLIPS, and 75-20 SLIPS were the only samples to retain water into the beginning of full turbulence; these samples all displayed at best 10% reduction in torque and were SLIPS. This indicates that patterning SLIPS increases water retention; Flat SLIPS and SuperSLIPS, as well as all SH samples, ceased retaining water before this point, reaching at best 35 rad/s.

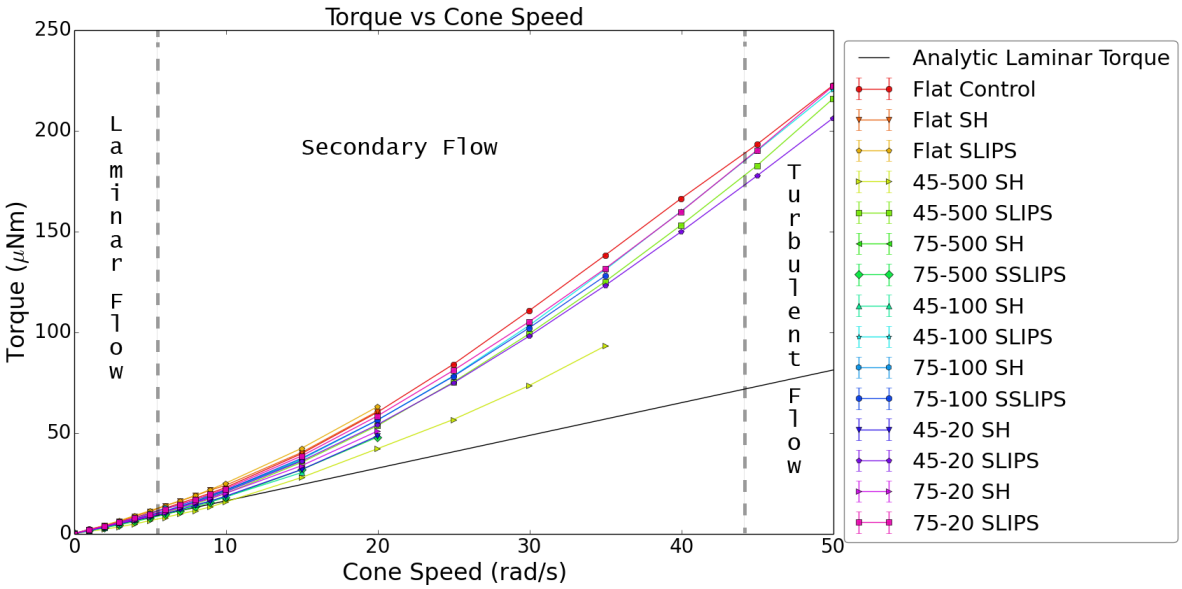

Figure 25: Torque Measurements with minimal water. Lines that end early indicate that water was ejected from the gap under centrifugal forces above that speed.

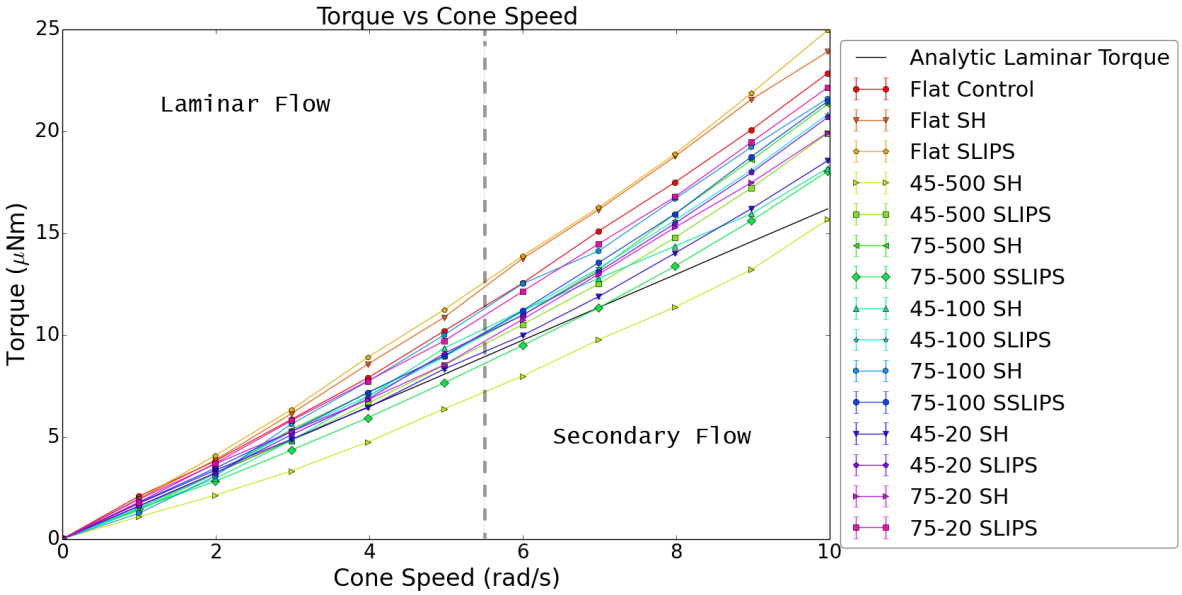

Figure 26: Torque Measurements with minimal water in Laminar flow.

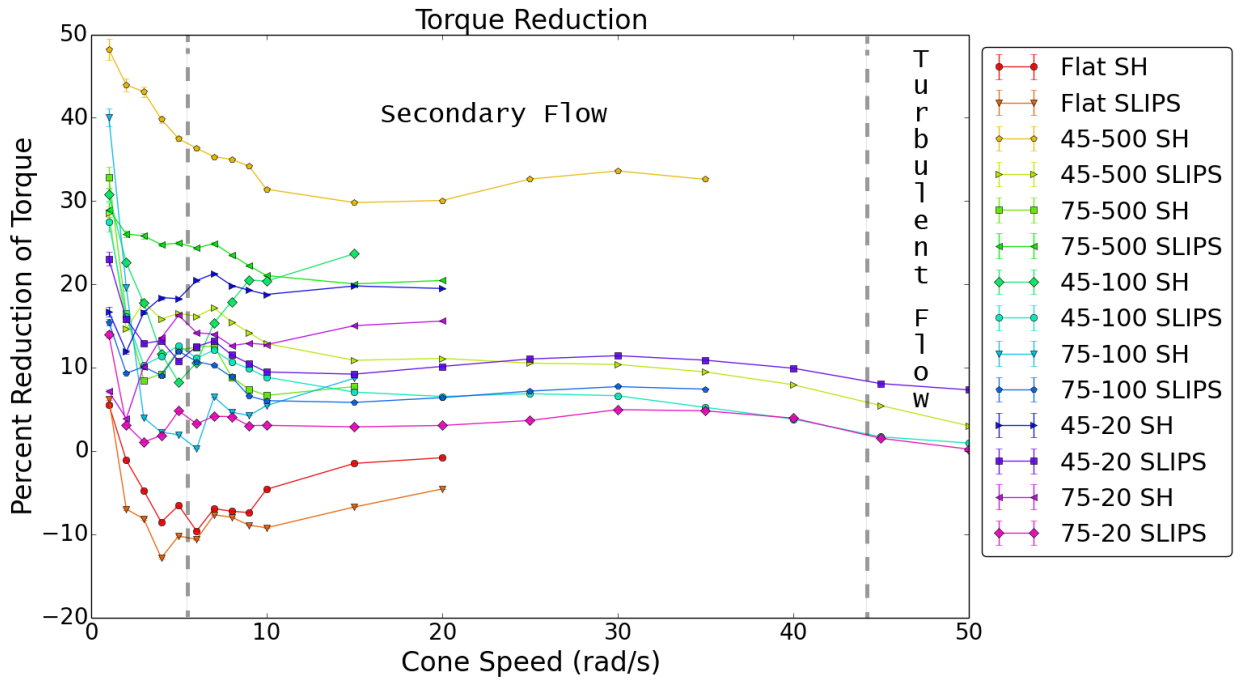

Figure 27: Percentage drag reduction with minimal water compared to a flat plate. Lines that end early indicate that water was ejected from the gap under centrifugal forces above that speed.

For laminar flow the reduction is approximately constant, so we show the average torque in laminar flow for each sample in Fig. 28. We see once again from this data that 45-500 SH provides the largest drag reduction of any sample, at slightly below 40% reduction in laminar flow. Interestingly, this is far higher than the best performance of the 45-1000 SH sample tested by ORNL, which may indicate that making the grooves too deep causes the drag reduction performance to worsen. 75 SH samples performed poorly in general, barely breaking 10% reduction and being much less effective than 45 SH samples at all depths. 75-500 SLIPS had the best SLIPS performance at about 25% reduction, nearly 2/3 the performance of our best superhydrophobic samples. 45-100 SLIPS was slightly more drag reducing at 16% than 45-100 SH and 75-100 SLIPS, which were about equivalent around 10%. 75-100 SH and 75-20 SLIPS samples had notably bad performance, giving almost

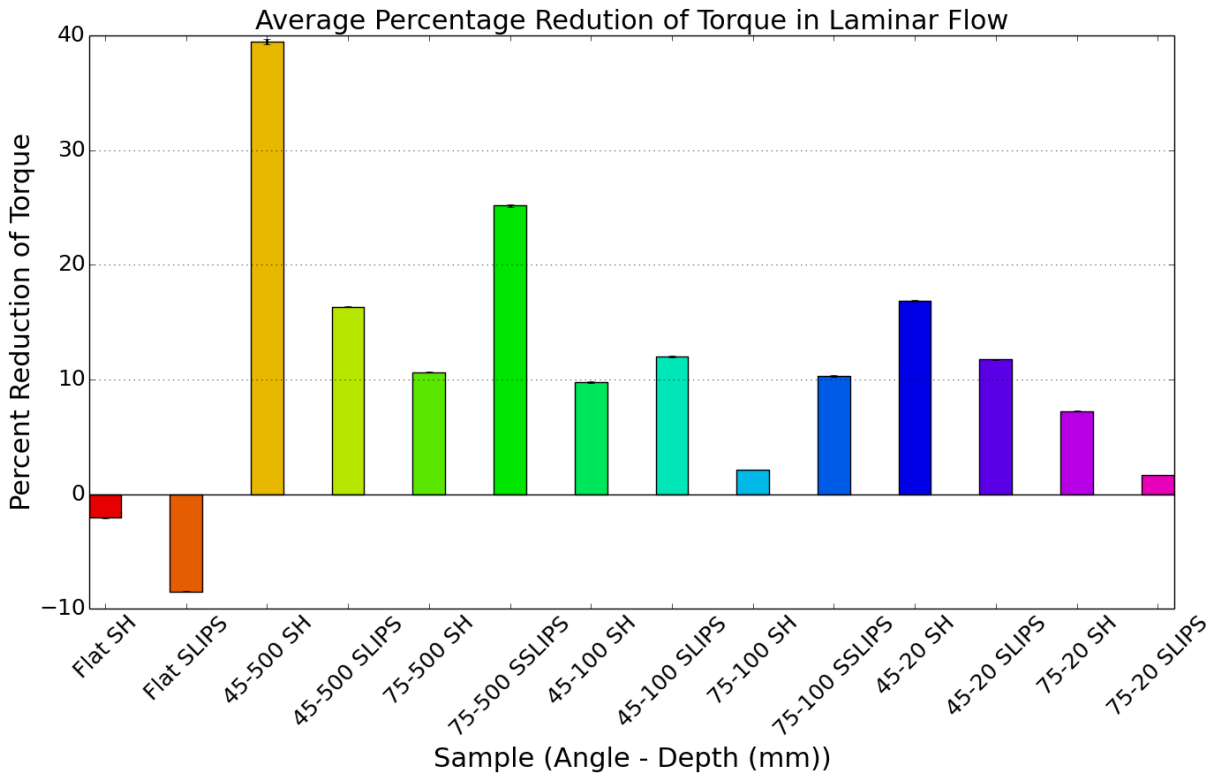

Figure 28: Average percentage drag reduction with minimal water in Laminar flow compared to a flat plate.

no drag reduction at all. Overall, SLIPS material showed the ability to reach about 10% reduction with 1 exception, being slightly worse than SH material in most cases when not SuperSLIPS. When SuperSLIPS was achieved, it tended to be more drag reducing than SH samples with the same geometry.

However, there the question of how much of this drag reduction is due to the effect of simply grooving the surface, as such grooving is already known to produce drag reduction without microstructuring [92]. To check this, we measured a series of bare metal controls, cut to the same shape as each sample, and percentage reduction was recalculated relative to these grooved controls. Looking at Fig. 29, and most strikingly at Fig. 30, we see that, while for 45° grooved samples only a very small portion of the drag reduction was due to the

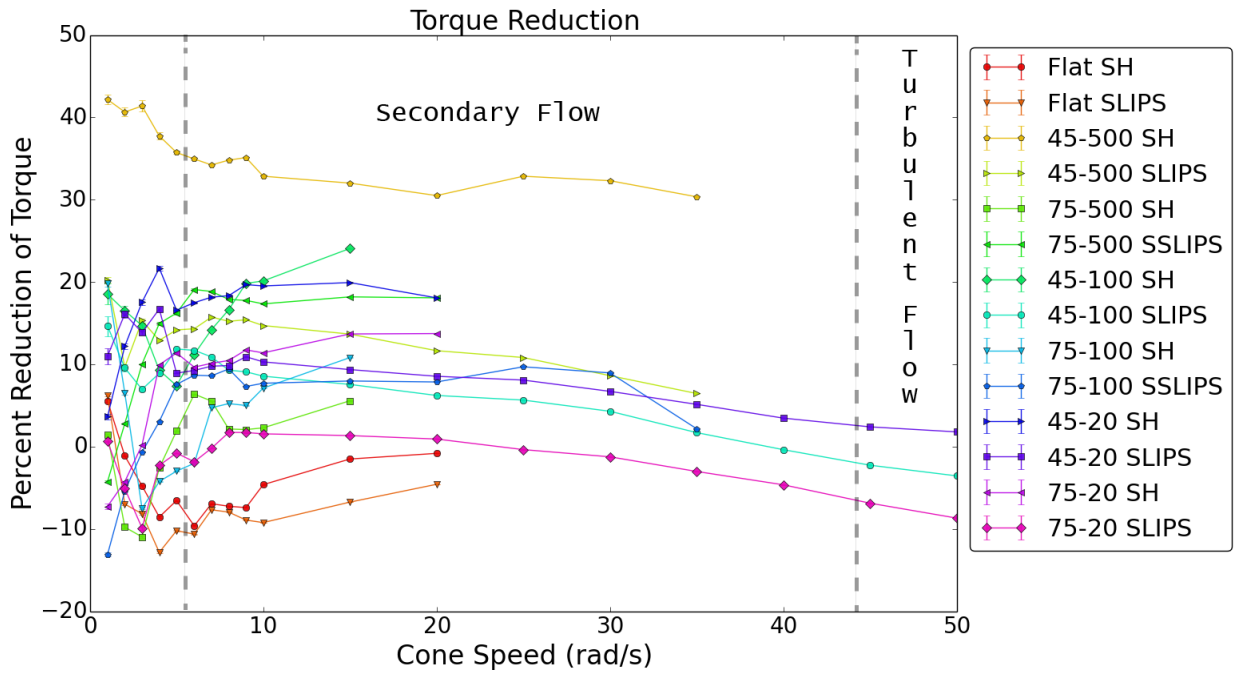

Figure 29: Percentage drag reduction with minimal water compared to identically shaped grooved controls. Lines that end early indicate that water was ejected from the gap under centrifugal forces above that speed.

groove shape, for 75° grooved samples the Superhydrophobic coating makes little difference. 45-500 SH provides the largest drag reduction of any sample, at slightly below 37% reduction in laminar flow, dropping to 30% in secondary flow. 45-100 SLIPS was slightly more drag reducing at 10% than 45-100 SH at 8%. 45-20 SH at 16% and 45-20 SLIPS at 9% performed better than 45-100 SH. SuperSLIPS still show improved behavior relative to the behavior of Superhydrophobic samples of the same shape, but on the whole 75° grooves are measurably worse than any surface with 45° grooves. SuperSLIPS do not appear to provide a useful benefit based on these measurements, as the overall drag reduction performance is less than that of more easily produced Superhydrophobic surfaces or SLIPS. However, there is still the possibility that the state may prove more useful on other materials where it can be achieved on less steeply angled surfaces.

All data presented except for our control sample is for singular runs. The control measure-

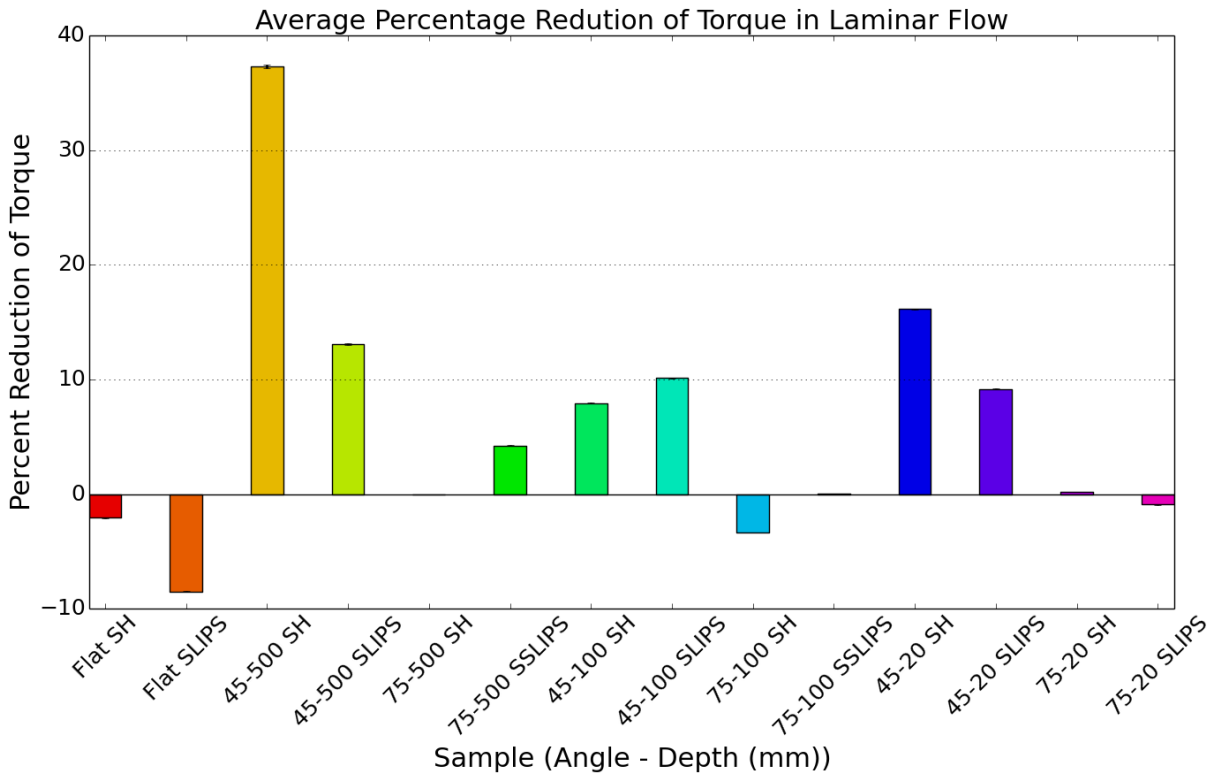

Figure 30: Average percentage drag reduction with minimal water in Laminar flow compared to identically shaped grooved controls.

ment was repeated 4 times to examine repeatability and to provide a more robust comparison basis for the percentage presentation. Examining average performance over a large number of runs would provide for less noise, but this is impractical for our setup.

Experimentally, one of the main points of uncertainty is in the air layer loading of our surfaces. Future work would benefit from finding a way to obtain more consistent loading; currently we must simply accept whatever air layer is present (our only method of controlling this is to remove and reapply the water if there are visible bubbles or other issues). This could lead to differences in air loading beyond the differences caused by varying geometries and surface states that we have no control over. This importance of this issue is increased because our measurements take such a long time (due to alignment and equlibration time),

leading us to only take single measurements on most samples, so that this effect is not averaged out over multiple runs.

7.2 PHOTON CORRELATION SPECTROSCOPY MEASUREMENTS

Torque measurements do not directly measure the behavior of the fluid itself, and are an average measurement over the entire surface. Measurements of the shear rate, on the other hand, allow us to measure the fluid directly and locally. Photon Correlation Spectroscopy (PCS) measurements, as discussed in Chapter 5.2 allow us to directly measure the shear rate. This is done by scattering the light from a collimated HeNe laser off of particles seeded in the flow, and collecting this light with a collimating lens feeding into a single mode optical fiber.

For these measurements we utilize a 6° cone to allow our beam to pass through the gap without major clipping. For this cone, taking our measurements at a radius of about 15 mm, the onset of secondary flow is about 2 rad/s and the onset of turbulence was seen at about 15 rad/s [82](due to slight positional differences between runs, the transition speeds shift slightly between samples). Before we can measure our novel surfaces, we must confirm that the method works by checking it on our control sample.

7.2.1 Verifying Our Method For Shear Rate Measurement

PCS data taken in fluid flowing past a flat aluminum plate, and a fit curve to that data, are shown in Fig. 31. The shear rate vs cone speed curve generated by our apparatus is compared to the theoretical line (Eq. 5.3) in the laminar limit in Fig. 32. Data sets were gathered by increasing the cone speed from 0.2 rad/s to 3.0 rad/s in increments of 0.2 rad/s, with data at each cone speed averaged from 20 repeated readings at that speed with an averaging time of 10 s each. Five complete data sets were gathered, with a full removal of the sample and realignment between sets, to test the repeatability of the measurement.

We see remarkably good agreement with the theoretical values of shear rate in the laminar

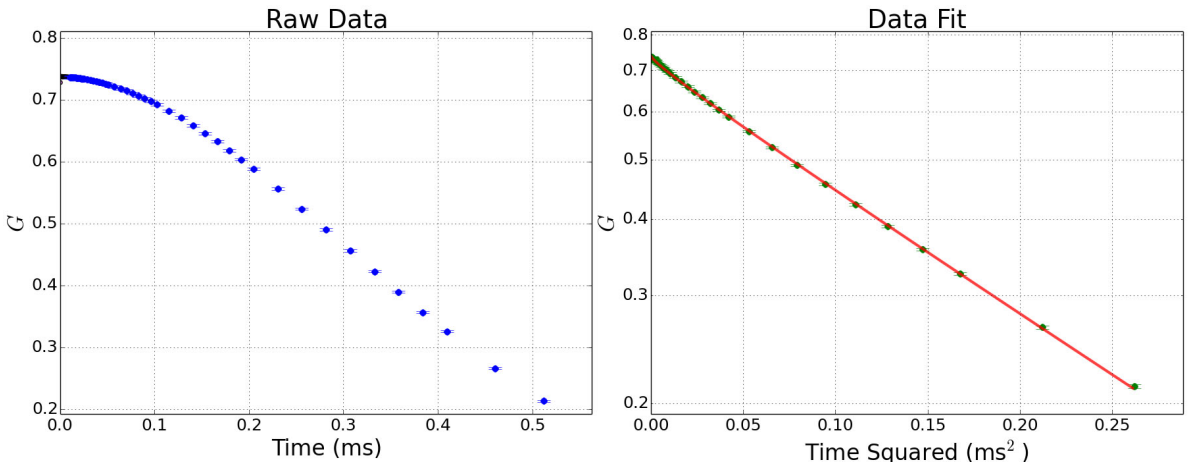

Figure 31: Data and fit for a measurement taken at 0.4 rad/s cone speed at a scattering angle of 20.5° on a control sample, with a $2w_0 = 0.81\ mm$ beam and a $2w_s = 1.05\ mm$ detector. The left graph shows the raw data, while the right shows fitting with Eq. 5.32 on a logarithmic scale vs τ^2, so $G(\tau)$ is a straight line except near $\tau^2 = 0$.

regime, where the average slope of the Shear Rate vs Cone Speed graph over the 5 data sets was $9.61 \pm 0.03\ rad^{-1}$, a 0.6% error compared to the theoretical slope of $9.55\ rad^{-1}$. Slopes from individual data sets showed a statistical error of at most ±0.5%, while individual slopes varied from the theoretical value by a maximum of ±2%, larger than could be accounted for by statistical error alone, indicating additional sources of error in our experiment.

Tests of repeatability indicate that the additional error results from limited repeatability in assembly and alignment, including the setting of the scattering angle, measurement of the widths of the input beam and the lens/fiber detector, determination of the direction of the velocity at the measurement point (which is needed to properly perform the scalar product $\vec{k} \cdot \hat{\phi}$, see Fig. 33), errors vertically aligning the beam and the receiver with each other and the gap, and error in the distance of the cone from the plate. Despite these issues, our measurements were still highly accurate, indicating that the method is quite robust.

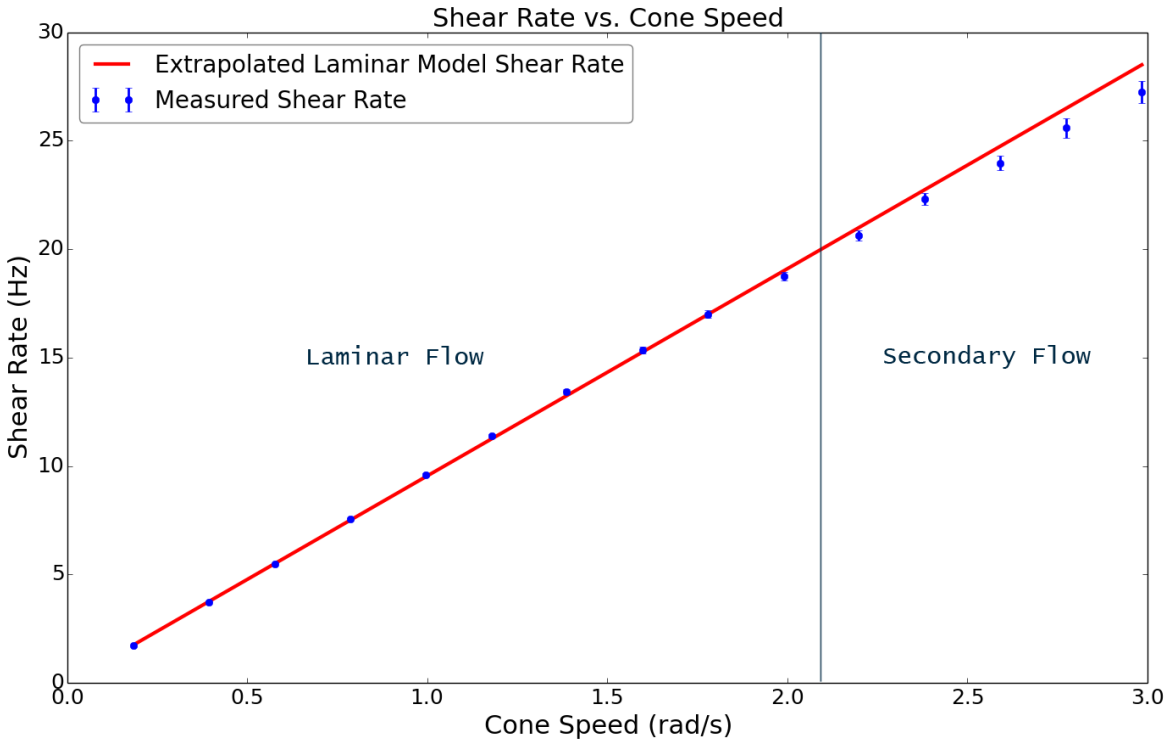

Figure 32: A single data set showing the measured and theoretical shear rate as a function of cone speed at a scattering angle of 20.5° for a single run on a flat control sample.

7.2.2 Shear Rate Measurements on Superhydrophobic Samples

We examined each of our Superhydrophobic samples using PCS measurements, at a scattering angle of 20.5° and a radius of approximately 15 mm; shear rate measurements in the laminar regime can be seen in Fig. 34. We graph the reduction in shear rate, which should be approximately proportional to the reduction in drag, in Fig 35. Looking at these graphs, it appears that simply making a flat surface Superhydrophobic can be detrimental at lower speeds, having a 4% increase in shear rate at worst. Unlike other surfaces, our flat Superhydrophobic surface varies non-linearly in the laminar regime, increasing from 0% reduction at 1 rad/s to 7% as we enter secondary flow. The reduction in shear rate for grooved surfaces is mostly grouped by groove depth, with no significant differences between the reduction seen for 45° grooves and 75° except at the lowest groove depth. Grooving to 500 mm shows

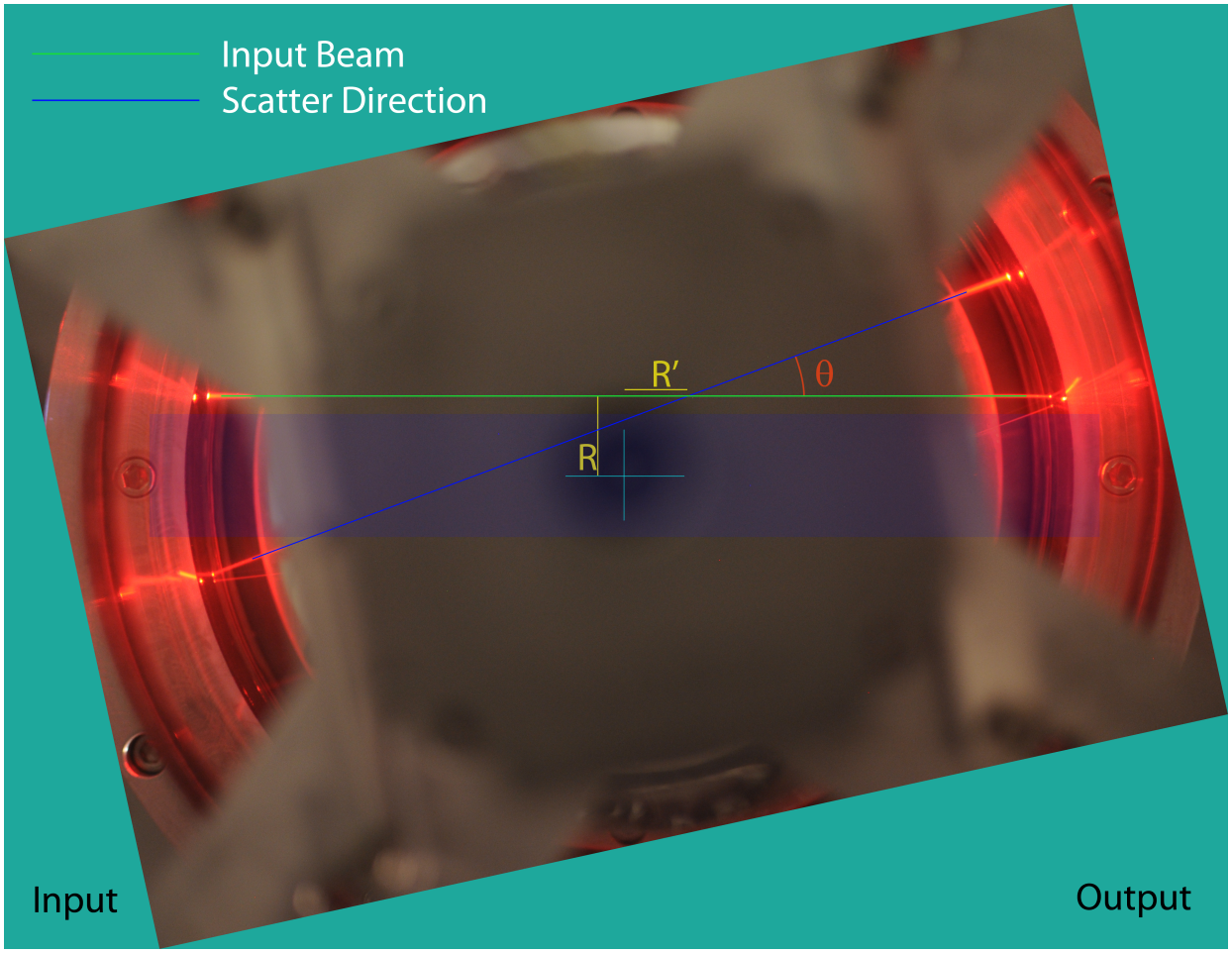

Figure 33: Example of measurement of the position and angle of scattering. The point where the beams cross is where shear rate is being measured. R and R' must be kept track of to determine ψ (see Chapter 5.2.1)

great improvement at the lowest speeds at almost 10%, but this rapidly decreases to around 3% with increasing flow speed. 100 mm deep grooves give slight but reasonably consistent reduction throughout the laminar regime at 2-3%, actually slightly improving with increased shearing. At 20 mm, however, 75° grooves are far superior, giving a consistent reduction of 1%; still smaller than that given by 100 mm or 500 mm grooves. In contrast, 45° grooves at this depth lead to increased shear, barely reaching 0% reduction in the laminar regime. A possible mechanism behind the loss of drag reduction in the more deeply grooved samples is

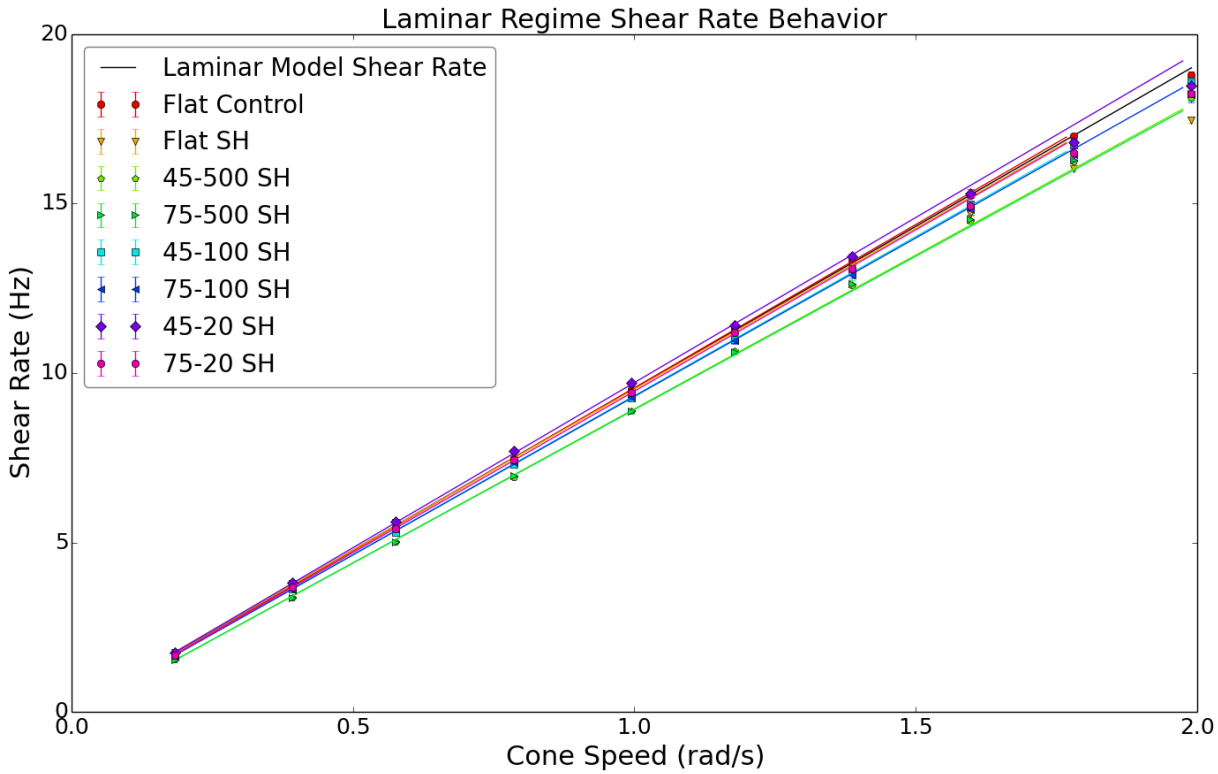

Figure 34: Shear Rate in the Laminar Regime as a function of cone speed.

that the deeper grooves are unable to hold onto the thicker air layer as shearing increases. Another possible mechanism is that the thicker air layers in the grooves enter heavy turbulence before the water leaves laminar flow; Reynolds number is proportional to viscosity, and turbulence manifests more strongly in larger fluid volumes.

When looking at the laminar torque and shear rate measurements taken, we see some inconsistencies. Most notably, the shear rate measurements do not indicate a significant difference in the shear rate with groove angle, while the torque measurements of superhydrophobic samples show 75° grooves performing much worse than 45° grooves at all depths.

In chapter 5.1.1, we saw a scaling relationship between torque and shear rate in the simple case of a flat plate and a single fluid. However, as shown in Eq. 5.5, even in the case of simple superhydrophobic surfaces the introduction the air layer makes it difficult to

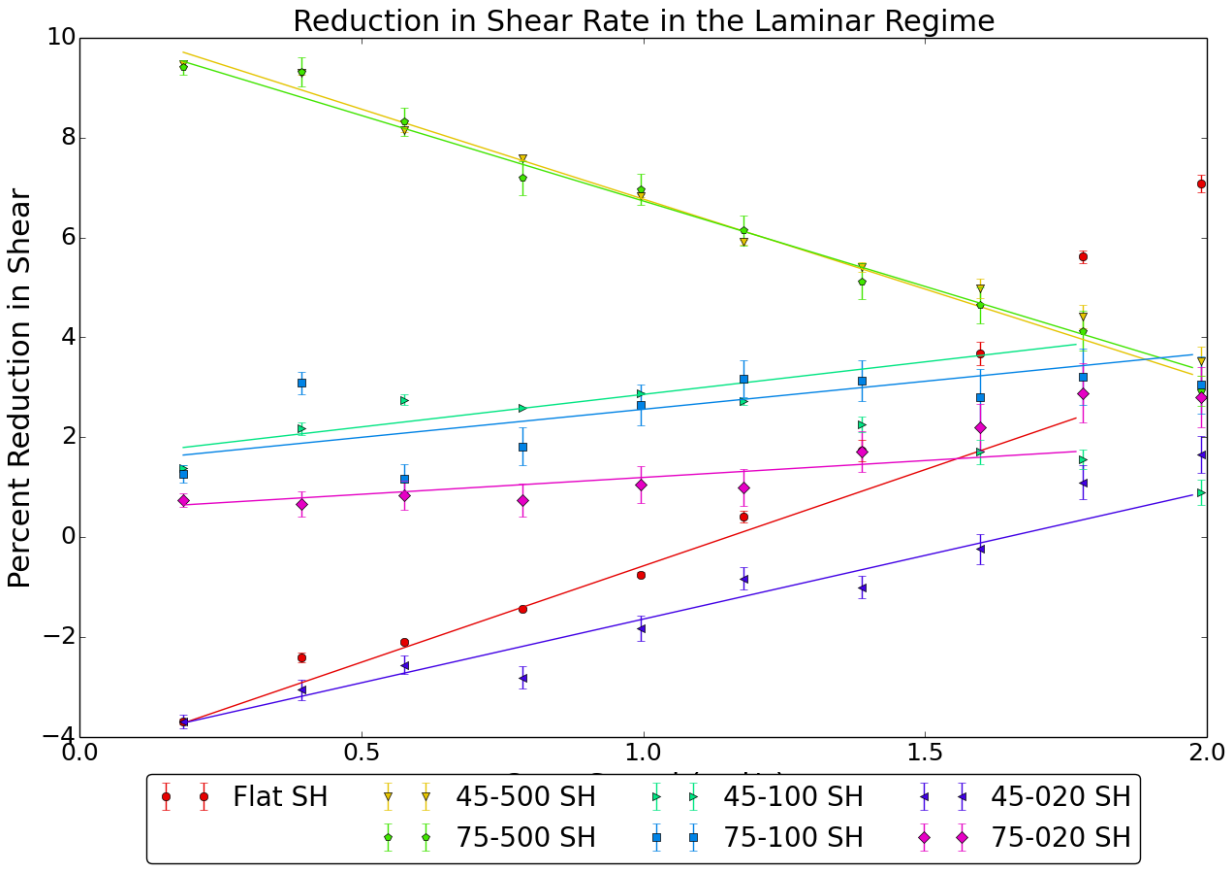

Figure 35: The percentage reduction in shear rate, relative to a flat aluminum plate, in the Laminar Regime as a function of cone speed.

relate torque and shear rate, and as shown in Eq. 5.7, we cannot analytically relate torque and shear rate at all in the presence of large scale structure. We expected that, while it would not be possible to quantitatively transform between the torque and shear rate, the measurements would still have the same qualitative relationships across our various samples. This does not appear to be the case.

There are several issues with these measurements. We took shear rate measurements at a single point, but the shear rate is likely not only a function of radius in general but also of the surface grooving, behaving differently over the points, the troughs, and as a function of the instantaneous depth of the grooves. These differences would only become more apparent

as we move into turbulence. Even in laminar flow, we cannot say we are in exactly equivalent locations relative to the grooves on each sample, as our alignment only informs us of our position relative to the cone. Therefore single point measurements such as these are not truly representative. We would need to be able to scan the scattering volume across the surface structure in order to reasonably state that we have sufficient data to account for the variations in flow they cause. We would need to significantly modify our apparatus to allow automation of the positioning in order to take these readings across a representative space above the sample (at least several grooves); it would also require additional theoretical work to understand how to interpret the spatially varying information.

We do not analyze measurements in the turbulent regime for several additional reasons. First, our measurements are taken over 10 s, so we may be missing fine details in the turbulence due to averaging. In all likelihood, readings of the turbulence probably contain multiple shear rates as the flow fluctuates, so analysis would be required to extract the different rates and see if there is any structure to these fluctuations. In order to more effectively take readings in turbulence, we would need to acquire or construct a new hardware correlator that could read shorter timescales. From a theoretical standpoint, there will no longer be only a single component of $\mathcal{S}$ that is non-zero in turbulence, so a method must be found for decomposing the fit to $G(\tau)$ into the different shear components, and to account for the time varying nature of the flow.

While we establish that the method is well behaved in simple flows, our data is not sufficient to make direct comparison to torque measurements as a technique for measuring drag on samples of this type. Note that even with the need to scan horizontally, we still vastly reduce the amount of movement needed compared to older methods, such as LDV.

8.0 CONCLUSIONS

In this thesis, we have examined the static wetting and dynamic drag properties of mutltiscale structured surfaces. Our surfaces were composed of a spiked Porous Anodized Alumina microstructure with a polymer coating over a set of micro to millimeter scale concentric grooves. We varied the depth and angle of these grooves and explored the effect this had on the Superhydrophobic and SLIPS wetting and drag properties.

We investigated the wetting properties of multiscale Superhydrophobic surfaces and SLIPS by examining the contact and rolling angles as we altered the angle of our millimeter scale concentric grooving, as well as observing the samples underwater. As anticipated from previous work, contact angles on SLIPS were much lower than on Superhydophobic surfaces, but this did not lead to significant increases in the rolling angle. For some groove angles, rolling angle was lower on SLIPS than for similar Superhydrophobic samples, which would seem to indicate that the SLIPS state is capable of providing higher drag reduction than Superhydrophobic samples for some geometries.

By varying the oil layer thickness, we also found clear evidence that, pursuant to geometric conditions on the grooves and a proper oil level, the SuperSLIPS state does exist. It has a noticeable effect on the rolling and contact angles, and can it can be clearly seen to reduce the wetting contact of droplets on surfaces.

Our investigation of torque showed that drag reduction is greatly influenced by the groove geometry. Both Superhydrophobic and SLIPS/SuperSLIPS samples displayed changes in the drag correlated to varying groove depth and angle. We found that multiscale SLIPS with 45° grooves have some drag reducing potential, even managing to approximately match the drag reduction of hydrophobic samples of the same geometry in a few cases. This shows that SLIPS can be used in drag reducing applications if their anti-fouling properties are desirable, and in a few cases they may be preferable. SuperSLIPS outperformed identical Superhydrophobic samples, which had negative or near zero drag reduction compared to simple bare aluminum of the same shape. These results demonstrate that SuperSLIPS have an effect on the properties of surfaces, but do not provide a significant benefit compared to SLIPS with wider or more shallowly angled grooves, particularly since wider and shallower grooves are easier to produce. Further experiments would be needed to determine if SuperSLIPS surfaces are practical; in particular, the state needs to be looked at on material that can

transition from SLIPS to SuperSLIPS with wider/shallower grooves. They show potential for increasing drag reduction in cases were multiscale surfaces are otherwise of little benefit, but on the surfaces tested, the net drag reduction is not significant compared to more easily produced SLIPS.

Additional measurements at more groove angles and depths would provide a better understanding of what factors influence drag. Specifically, further exploration of depth on 45° samples may demonstrate an optimal depth for maximum drag reduction, while exploration of drag with regard to groove angle may explain why 75° groove angles performed so badly. Multiscale SLIPS samples do not appear to provide much benefit compared to Superhydrophobic samples in terms of drag reduction alone, so further work is mainly indicated for anti-fouling benefits. The anti-fouling behavior of SuperSLIPS has not been tested, so it is possible that SuperSLIPS on an alternative material could more effectively achieve anti-fouling drag reduction, but at this time this is pure supposition. Generally, more consistent air loading of Superhydrophobic and SuperSLIPS samples would be beneficial to future torque measurements, making comparisons between runs simpler. As far as our system is concerned, faster cone alignment and better damping would also make it possible to take more measurements more quickly.

We tested an alternative method of performing drag measurements, by directly measuring the shear rate using Photon Correlation Spectroscopy (PCS), which had not been applied with quantitative accuracy to 3-D flows before. We successfully confirmed that PCS measurements worked in simple laminar flow, as our readings of the single non-zero shear rate component on flat samples agree with theory and extensive prior work to within 2% error. Our principle derivation does not depend on use of a CPR for measurements, so this formalism can be applied to other systems.

It had been hoped that, despite the non-analytic theoretical relationship between torque and shear rate on multiscale surfaces, experimental work would show qualitatively proportional behavior, but this does not appear to be the case. It is apparent that looking at a single shear rate measurement, which takes a reading only at a single location on a sample, is a poor choice for comparison to torque measurements, which average over the entire sample, in cases where the sample is not spatially homogeneous.

Further theoretical work is needed to understand PCS measurements in turbulent flow, and to relate these to torque in our system. Work is also needed to understand this relationship in laminar flow in a Cone & Plate Rheometer in the case of non-homogeneous flows. Measurements need to be taken across an area of the sample, so that the spatial variation in the shear rate in relation to the spatial variation in the sample can be examined. Measurements in turbulent flow would also be better taken in shorter amounts of time, which will require the purchase or construction of a new correlator that can go to lower averaging times. With this shorter time data, we should be able to see changes in the shear rate as eddies occur in the scattering volume, or alternatively, if the eddies are too fast, it may be possible to decompose the data in order to see substructure. This indicates that further work with the method could provide useful information on turbulent flows, which are in general difficult to observe.

Overall, this work provides us with an insight into drag properties on Superhydrophobic and multiscale SLIPS samples, opens up investigation of a new type of surface wetting state, the SuperSLIPS state, and begins to explore a new method for the investigation of fluid flow involving complex surfaces.

APPENDIX A

PROCEDURES

A.1 ANODIZATION AND COATING PROCEDURE

A.1.1 Anodization System

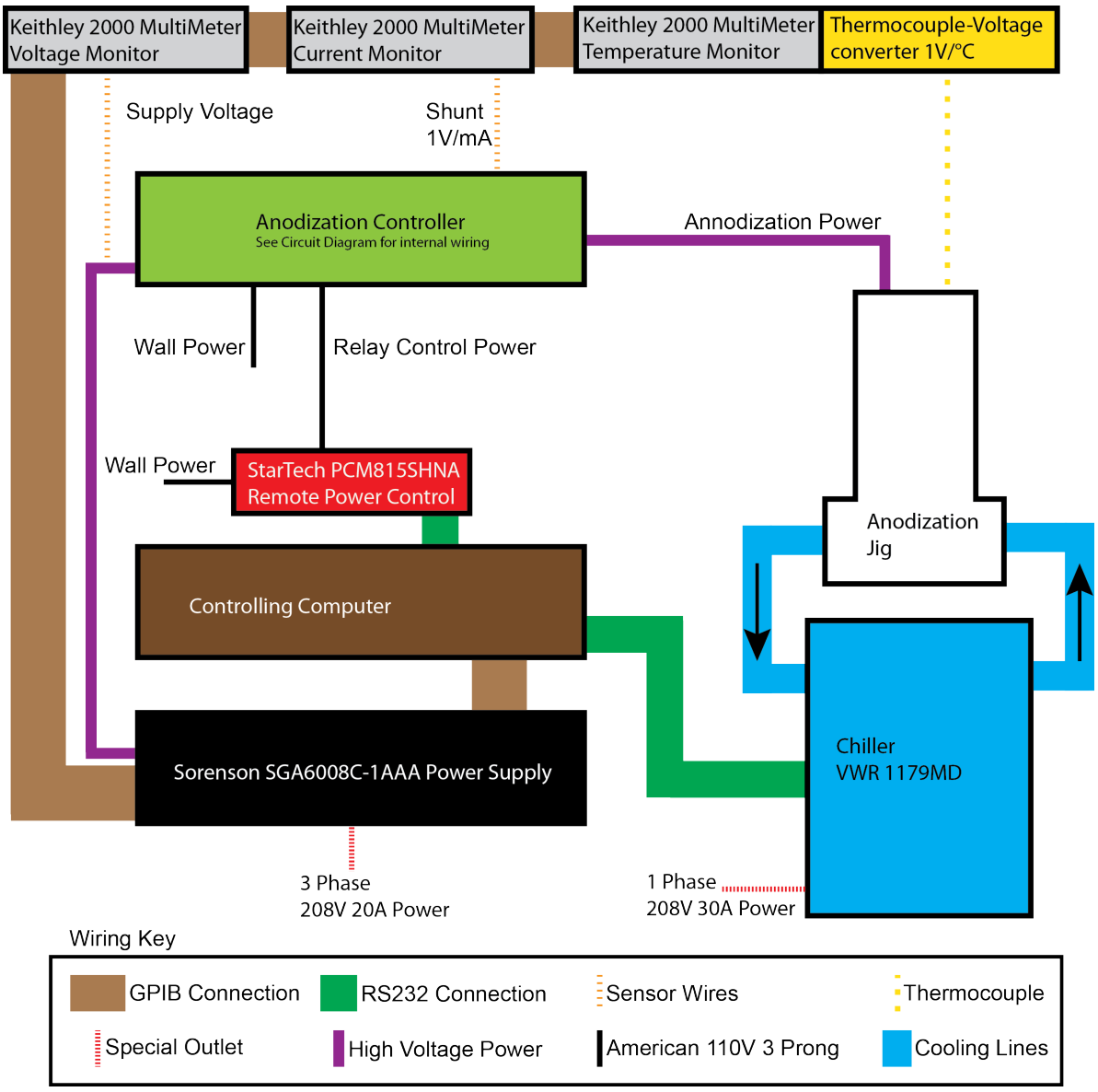

Figure A.1: Anodization System Wiring.

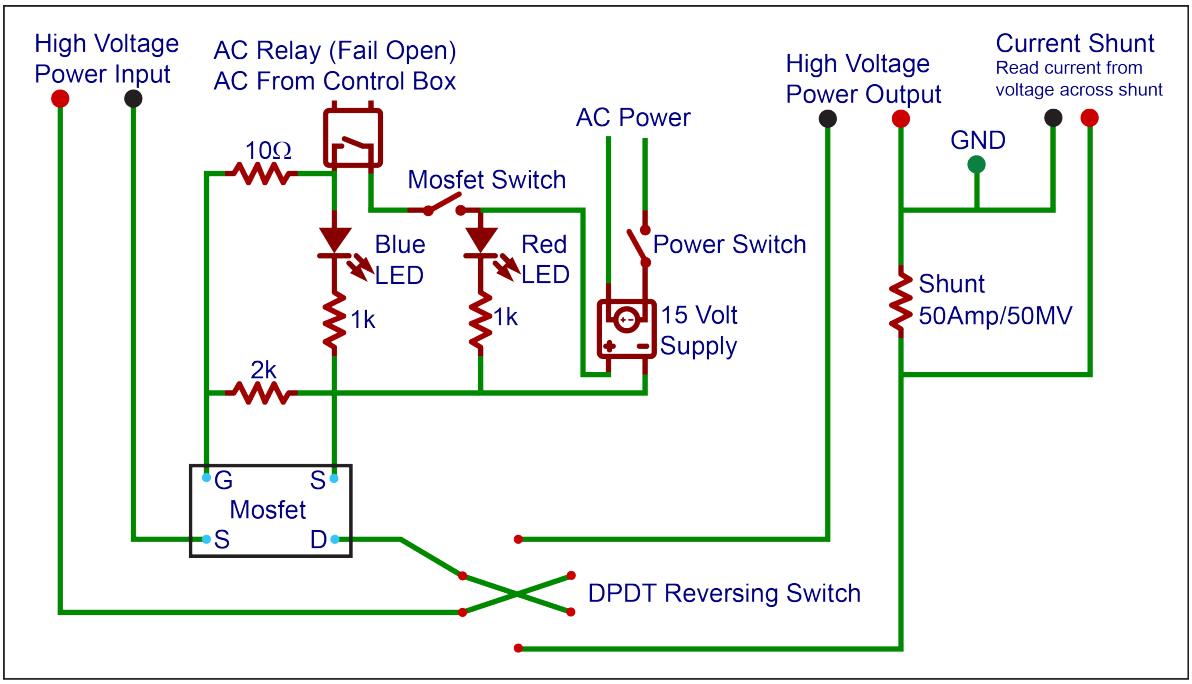

Figure A.2: Anodization Controller Box Circuit Diagram. Input and output colored dots match plugs on box. High Voltage Power Output is ground to negative voltage when reversing switch is in forward anodization position. Power and mosfet manual flip switches and the relay must all be closed to engage anodization. AC inputs take American 110 V 60 Hz power via built in cables.

A.1.2 Sample preparation

Before being cut on the Diamond Turning Machine, the samples must be annealed. Annealing temperature depends on size and shape of material.

Sample Type	Temperature
2in Diameter 0.5mm Thick	500°C
2in Diameter 0.25in Thick	655°C
4in Diameter 0.25in Think	500°C

Anneal discs for 16 hours. After cutting on Diamond Turning Machine, if not being anodized immediately, store in vacuum to prevent native oxide regrowth.

A.1.3 Anodization

Chemicals for anodization

- Citric Acid 0.1175 Molar:
  - 2 in system: 23.5 mL 1 Molar Citric Acid + 176.5 mL H_2O
  - 4 in system: 47 mL 1 Molar Citric Acid + 353 mL H_2O
- Tetramethylammonium Hydroxide (TMAH) 2%wt (81ml 25% TMAH + 749mL H_2O):
  - 2 in system: 200 mL
  - 4 in system: 400 mL

1. - For Thin Foil samples: Apply water to center of mediator disc such that it is coating with a thin film of liquid across the surface. Place disc on mediator, being sure to touch only outer edge. Beware as discs bend extremely easily.
   - For Thick Disc samples: Place aluminum foil strips around rim of holder. Ensure disk is properly seated.
2. Screw down upper vessel. Tighten evenly using alternating pattern. Do not over torque, as this will deform upper vessel and sample.
3. Open coolant lines; watch for leaks and correct.
4. Add rinse water (greater than chemical volume), place stirrer and rinse for at least 1 minute at 500 RPM+. For the anodization stirrer, be careful when putting in, as teflon rods are breakable.
5. While rinsing, prepare anodization cycle script. Always power cycle the automated switch box (by pulling and reconnecting the plug) before starting the software. Turn on all multimeters, the power supply, and engage the power switch on the power control box. Watch for warnings and failures in the initialization; reload the VI once errors are fixed. If the chiller is not responding, power cycle it with the switch on the rear.
6. Check cycle script carefully. While the settings for a step can be changed while the script is in progress (step is re-read every time it starts), whether or not the step is used and how many times it runs cannot be changed once the script is started. Group repetitions are set by the first group member and groups must be contiguous.

7. Attach thermocouple and check that the relevant multimeter is reading a logical temperature (in Celsius). Ensure that coolant lines are open.
8. Dump rinse water into beaker (for disposal or reuse) and add or prepare insitu Citric acid solution.
9. Put in anodization grid and stirrer and activate. Anodization steps are stirred at 500 RPM.
10. Begin script. Bath will cool to precooling temperature before starting first anodize. Disengage power circuit safety; for the duration of the script, power will be controlled by the computer operated switch, and will automatically engage when an anodization step begins.
11. Ensure electrical contact occurs at start of first cycle. If current does not go to limit, tighten screws a little and flick the MOSFET switch on and off until connection is established. Once it has connected once, it will always connect on future steps.
12. Observe initial anodize to ensure there are no issues. If there are issues making electrical connections, try slightly tightening the upper vessel and/or flipping the manual power switch open and closed. Abort if needed.
13. Pour Citric Acid into designated beaker, and add rinse water. Rinse cycles should always stirred be at 500 RPM, by whichever stirrer is in. Dual rinse between steps: one quick rinse (about 30 s), and a thorough rinse for 2 min. Second rinse water can be reused as first rinse water in the following swap for conservation.
14. Separate pause steps are used to allow for rinsing and swapping liquids. To proceed from a pause step, push 'Go To Next Step'. Be careful to move mouse away from button, so as to not accidentally hit this button during a step or double tap it.
15. Measure out TMAH and add to jig. Have the stirrer already in place and running at 100 RPM before adding TMAH. Beaker volume markings are sufficient for TMAH measurement.
16. The software will sound a gong at the end of each step. Change liquids as needed. Do not mix up liquids. When going to anodization, let citric acid reach 18° or less before engaging current.

17. The chiller will stop at the end of the final anodize (there will be no gong). Coat the sample in IPA while dissembling the upper vessel. Remember to close the coolant lines before releasing the screws, to prevent leakage. Also turn off the MOSFET switch, preventing any power from flowing into the grid. For samples directly in contact with the coolant, a vacuum may develop under sample; In this case, slightly open the outlet value in order to equalize.

    Notes and warnings:

- Upper area is manual controls.
- The precool temperature will cool down the bath initially to the set temperature. All temperatures are ± 0.5 degree Celsius.
- Set each step individually. Always place a pause step when changing working fluids. Any steps with a pause between them will proceed with no break. In the event of problems, the previous and next step buttons may be used to navigate the cycle (this will reset the timer/counter in any steps involved). If paused, use the next step button to proceed.
- Be sure to save (using the File Actions area) before exiting, as all data will be lost on restart. In the event of error, find the file listed under Run Data File location at the bottom of the VI and rename it before the next load-up of the controller; this file holds the data while the run is in progress and will not be overwritten until the next time the VI is initialized.
- Any steps with group none will act independently, and if a repeat is set it will repeat this step without proceeding.
- All grouped items will repeat using the first group members repeat count; after pressing start, all following group members numbers will change to match. Groups will repeat sequentially, running through all steps in order before returning to the first. Group assignments, repeat counts, and whether a step is active cannot be changed while the sequence is running. Other step settings may be changed so long as the step is not currently being executed; steps are reread from the GUI everytime they start.
- If the Use settings for all steps box is checked, the first steps voltage and current settings will override any manual entries for the later steps; an override switch is also provided if

Sample (angles from flat)	Voltage	Current Limit	Initial Anodize	Initial Etch	Primary Growth Cycle	Final Anodize
2 in Diameter Flat	320 V	.12 A	50 C	50 min	20 C + 24 min	30 C
2 in Diameter 30°	320 V	.14 A	57.74 C	50 min	23.09 C + 24 min	34.64
2 in Diameter 45°	320 V	.17 A	70.71 C	50 min	28.28 C + 24 min	42.43 C
2 in Diameter 60°	320 V	.24 A	100 C	50 min	40 C + 24 min	60 C
2 in Diameter 75°	320 V	.46 A	193.19 C	50 min	77.27 C + 24 min	115.91 C
4 in Diameter Flat	320 V	.46 A	190 C	50 min	76 C + 24 min	114 C
4 in Diameter 45°	320 V	.65 A	268.7 C	50 min	107.48 C + 24 min	161.22 C
4 in Diameter 75°	320 V	1.78 A	734 C	50 min	293.6 C + 24 min	440.5 C

Table A.1: Anodization Cycles - Primary cycle is repeated 6 times. Anodization cycles for 2 in samples assume grooving from 5.5 mm to 21 mm Radius. Anodization cycles for 4 in samples assume grooving from 4 mm to 45 mm radius. Depth of grooving does not change anodization cycle (exception: 20 μm deep grooves are anodized as flat samples, regardless of groove angles).

only a few steps need to be changed.

- If different voltages are needed throughout, then they must be set manually.
- Step names are for user assistance only; they will appear in the status box to help the used track what they are doing. They are not recorded in the data file.
- The chiller requires time to start up. When in maintain mode, the chiller will try to hold the bath temperature constant, as read from the thermocouple. While in set mode, the chiller will hold based on the temperature of the coolant fluid in the chiller lines. It is recommended that the chiller be set reasonably close to where it needs to be when next engaged during steps when it is not maintained, as there is some rise and fall time.
- For pause steps, it is recommended to use set mode, as the thermocouple may be disconnected, in air or in rinse fluid during most operations during a pause. Check what the temperature on the chiller is in the following step and set the pause step to this value for smooth transition.
- VI can take a second to register clicks. Do not get impatient. If you click twice, it will double register.
- Chiller does not stop until the end of the sequence. Be sure to stop it manually before removing sample if a fault occurs, as coolant is under pressure while it is running. Closing the cooling valves with the chiller running may cause damage to the chiller.
- Chiller circulates 4:1 Water:Propylene Glycol as coolant. Propylene Glycol will not evaporate if spilled. Be aware that anytime the coolant passthrough under the sample is uncovered, coolant will escape. If the lines are closed, there may still be some seepage from the liquid inside the base. May be cleaned using paper towels.
- The pythics VI will freeze if the remote power switch fails. The VI must then be reloaded. Remember to move/rename the data file before reloading, and to note sequence location. You can resume a sequence by restarting the VI (after power cycling the switch), but you will need to set the active steps and the repetition counts correctly to resume.
- Do not set measurement period below .5s, as this will result in slowdown.

A.1.4 Spinner Programs

The following are the parameters of the spinner programs that will be used throughout the rest of this appendix.

Step	Time (s)	Speed (RPM)	Acceleration Index
1	6	100	001
2	13	500	001
3	30	4000	005
4	16	0	001

Table A.2: Spinner Program B Parameters

Step	Time (s)	Speed (RPM)	Acceleration Index
1	6	100	001
2	13	500	001
3	30	1000	005
4	8	0	001

Table A.3: Spinner Program F Parameters

A.1.5 Hyflon Coating

1. Clean Sample Thoroughly
2.
   - 2 in Samples: Oxygen Plasma Clean for 7min at 50W, at a pressure of 25 mTorr and a flow rate of 20 Sccm for Ar and 8 Sccm for O_2. Move from vacuum to coating as fast as possible.
   - 4 in Samples: Bake at 200°C for 2 Hours in convection oven. Allow minimal time to cool, while covered.
3. Apply HMDS: Spin Coat with (1:4 HMDS:PGMEA) using program B. Wait 10 s after full coat before starting spinner.

4. Apply Hyflon: Do not wait or allow HMDS to dry. Spin Coat using Program F.
5. Bake 30min at 75°C in convection oven (preheat oven)
6. Bake 30min at 300°C in furnace (preheat furnace to 75°C, then ramp as fast as possible with sample inside, Start timer when at 300°C.)
7. Minimally crack oven door to allow oven to cool to about 100° c before removing sample.
8. Cover immediately upon removal from oven to keep dust off

Notes:

- Be aware that samples are too hot to handle by hand, use tweezers or tongs to grasp the sample or use a cover glass to slide samples onto carrying plates.
- Center well before coating (center based on anodized part, not overall disc)
- Spread coatings across surface to improve quality (easier to coat with spinner lid up, then close)
- Errors direct function of time to coat; be aware of dust
- Touch outside anodized area only once coated

A.1.6 Hyflon Patterning

Photo patterning:

1. Clean Sample
2. Coat sample with AZ1512 Photoresist Using Program F, three coats
3. Soft Bake sample for 1 min at 100°C for thin foil or 10 min for think disc.
4. Expose sample[1]:
   - 5.5 min in exposure column with UV light
   - Direct write using DTM in lithography mode. Change between a slow speed to write and a very fast sped to run past asreas that should not be exposed. Using a 2x lens, with the laser at 2.25W, expose with 60 mm/min write speed and 500 mm/min run speed.
5. Develop PR using TMAH for 1 min, rinse in DI water and dry

[1]NOTE: Numbers given are approximate. Exact values depend on current properties of Photoresist, which change over time due to aging.

6. Oxygen Plasma Clean for 10min at 10W or apply metal coating
7. Remove PR by spraying with Acetone and Isopropanol, then blow drying

DTM Patterning:

1. Clean Sample
2. Mount sample to disc
3. Coat sample with AZ1512 Photoresist Using Program F, three coats
4. Affix to DTM and cut pattern
5. Release sample, taking care never to touch the upper surface

A.2 RHEOMETER LOADING & VERTICAL ALIGNMENT

1. Place sample in holder and secure with horizontal screws. Make sure sample is reasonably centered if uundersized. Do not over tighten as plastic screws will strip.
2. Place Sample holder in sample tank gently, and press down onto alignment pins. Be careful not to touch the top surface of the sample. It may be necessary to apply pressure to the holder to make it go completely onto the pins; apply pressure only to the outer rim are (where the vertical screw holes are). Be careful not to break glass cylinder.
3. Screw in vertical screws. These screws minimize the disturbance the holes cause in the fluid flow, they only minimally hold down the sample holder. Do not over tighten as plastic screws will strip.
4. Adjust bushing nuts coarsely to ensure cone will not touch sample accidentally when crossplate is lowered.
5. Fill tank high enough that the sample will not be accidentally uncovered when putting it in place. If needed, tilt, empty, or shake in order to deal with bubbles or other issues.[2]
6. Ensure the air bearing is not floating to prevent damage. Lift crossplate and place the sample tank onto the air bearing, rotating it until it drops onto the alignment pins.[3]
7. Lower the crossplate onto the top of the bushings, watching carefully for bubbles on the lower surface.[4]

8. Lower crossplate slowly and carefully down the bushings. Be aware that it will sometimes stick, resulting in a more sudden movement that intended.[5]
9. Carefully lower the alignment ring until it is resting on the upper lip of the cone.[6]
10. Check for air bubbles. If they are present and will present an issue, remove the sample holder and try again after removing them.
11. Screw down and tighten the upper bearing nuts. The crossbar may jerk downward if any bushings were stuck on a tread.
12. Adjust LVDT so entire travel to be used is within -1.5 to +1.5 V (linear range at 1V/mm) and secure. a reading of .8 V when on the alignment ring is ideal for a 1.74 mm target spacing.
13. If the experiment will use the airbearing, turn it on now.
14. Perform the following steps, proceeding in a star pattern around the 4 measurement positions, until all 4 readings are within 10 μm of target:
    a. Place LVDT on the alignment ring between the gaps.
    b. Check the reading on top of measurement plate. The reading will not be the same at all 4 positions.
    c. Subtract target spacing from this reading to get target reading. Do not be shocked if this reading is static for several runs; opposite sides may be acting counter to each other.
    d. Lift LVDT and rotate plate so LVDT is in gap
    e. Adjust plate to average of LVDT reading and target. Adjusting to the target will tend to overshoot, increasing the time it takes to align.
15. Lift and secure measurement plate
16. If performing torque measurement, ensure pattern is in an acceptable 0 position; adjust as needed.

Notes:

- Do not take a single reading on one side and use throughout. Cross is not 100% even. Take a new reading each time a position is taken.

[6]Watch for accidental bubble capture during this step; any bubbles that are trapped on the sample once alignment is complete cannot be removed without starting over.

- Perform alignment with motor on, as there is a slight change in height from the off state.
- Always align with air bearing in the same state (on or off) as it will be during measurements.
- Always make sure the airbearing is off when taking the sample tank on and off.
- Watch for suspicious changes in readings. If plate gets too low, it can be pushed up by the sample, giving the illusion of the cone needing to be lowered when it is actually being pushed into the sample. If air bearing is on, check that it moves freely after each adjustment. Take care not to hit the damper plate into the sides of the damping tank, as this will upset the zero point.
- When the airbearing is on, rotate both nuts on side together as much as possible. With the airbearing off, or when making very tiny adjustments with it on, designate one nut to each measurement position and adjust only it.
- Target is set during machining so that the gap will be a specific size (plate thickness + a leftover gap space). To check, use a flat plate and a thickness gauge (think metal shim) at nearest thickness.
- Be sure that no items are touching the air bearing during measurement.
- The control lines for the motor frequently fall down and touch the air bearing during alignment; make sure to pin then back up.
- Always check that the motor is working before beginning measurement cycles. Occasionally it can electrical issues which cause it to not move at all or to oscillate instead of rotating. Powercyle the motor and restart the VI to fix this. Once the motor is seen rotating normally, it will generally not fault later in the process.

A.3 TORQUE CALIBRATION

Inertial Calibration is recommended, as it involves lower uncertainties and less physical meddling with the apparatus, but both methods are viable. Inertial Calibration is also much faster.

A.3.1 Inertial Calibration

1. Center pattern in video window
2. Disconnect damper plate
3. Displace air bearing so that oscillations will traverse entire visible area
4. Record video of oscillations for at least 5 periods
5. Open video in Open Source Physics Tracker and fit to find oscillation frequency ω
6. $\kappa = I\omega^2$, where I is the moment of inertia of the entire air bearing and κ is the calibration constant, represent μB, where μ is the moment of the center magnet and B is the magnetic field from the ring magnets.
7. Reattach the damper plate and re-level it

   Notes:

- Be sure to include all parts that are attached to the air bearing at the time of measurement in I.
- Beware of spilling damping oil or dropping damper plate into the oil.
- Damper plate will twist vertically when screwed, so it must be gently re-leveled after screw is tightened.

A.3.2 Gravity Calibration

As this method is not generally used, it is highly manual, as time was not spent automating it extensively.

1. Turn off air bearing. Wrap string around air bearing shaft just above the mirror. be sure to wind at least twice, with final wind going around the shaft itself and not over other winding, tape, or other obstructions. Ensure string does not fall into mirror slot.
2. Turn on air bearing. Run sting over to pulley, and adjust so string is horizontal and hangs over pulley and into open air. Tie a loop in the string for hanging masses.
3. Set grid so it is as far as possible to the side for maximum range.
4. Taking a calibration point:
   a. Displace air bearing in one direction.

b. Wait 3 min for bearing to stop oscillating.

c. Using time lapse function in AmScope viewer (under capture), take 100 images. Label as weight of *mass*g, ie 1.45g. For no mass, label as 0.0g.

d. Displace air bearing in opposite direction.

e. Wait 3 min for bearing to stop oscillating.

f. Using time lapse function in AmScope viewer (under capture), take 100 images. Label as *mass*g, ie 1.45g. For no mass, label as 0.0g. To distinguish direction of displacement, you may add 0.000001g to the label without significant error.

5. Take points with at least 4 masses if possible.
6. Open 'grid_readout' pythics VI.
7. Load first 0g image. Set center as close as possible by eye.
8. Press 'Find Grid Parameters'. This will work out the actual grid center and spacing. If threshold is below 0.50, set to 0.50, or an indentation will appear in the simulation grid.
9. Press 'Load Simulation' and load the best available simulation, or press Simulate to generate a new simulation (takes about half and hour). Simulations must have a period within ± 5 bits and a threshold within ± 0.10 for reliable pattern matching. If threshold is too high, check to see if it still is close with a lower number; as long as it is approximately representative, it will lock.
10. Set batch processing mode to 'Zero' and press 'Batch Process'. This will find the average center of the zero mass images, giving more accurate absolute readings.
11. Set batch processing mode to 'Calibrate', and press 'Batch Process'. This will step through all the images in the folder and output to file labeled Results which will be placed in the same folder.
12. Open 'fitting_mag_torque_const.py' and set file path to this results file. Fit parameter κ is given in the CMD window as the first printed item.
13. Remove string from center shaft.

Notes:

- Ensure that the string is taught for all measurements. At low enough mass, the string will not be straight and this method cannot be used.

- Ensure that mass does not pull so hard that grid center is more than half out of view of the camera. At this point the software cannot tell the difference between the center and the rest of the pattern.

A.4 TORQUE MEASUREMENT

A.4.1 Measurement

1. Check grid position using AmScope viewer to ensure it is as far to the left as possible for clockwise rotation (right for counter-clockwise).
2. Load 'automatic_delay_series_moire_grid' pythics VI and set output file location.
3. Check all settings
4. Push start. Check camera internal settings.
5. Allow sequence to run. Avoid jostling experiment.

Notes:

- Ensure that maximum speed does not move the grid so far that the center is more than half out of view of the camera. At this point the software cannot tell the difference between the center and the rest of the pattern. If this happens, magnets must be moved closer and the system re-calibrated or a lower maximum torque must be accepted.
- Pythics settings cannot be changed while code is running.
- Camera settings are Manual exposure with an exposure time of 16 ms and a gain of 5 (maximum), Mode Gray and Flip Horizontal (under misc panel), and a resolution of 2048x1536 (maximum).
- Be sure to close AmScope viewer, as it will block the camera from being accessed by pythics.
- If Amscope viewer is choppy, disconnect laptop power cable. AmScope viewer (but not pythics) has issues with the camera when on wall power, but not battery.

A.4.2 Data Processing

1. Open 'grid_readout' pythics VI.
2. Load first 0 speed image. Set center as close as possible by eye.
3. Press 'Find Grid Parameters'. This will work out the actual grid center and spacing. If threshold is below 0.50, set to 0.50, or an indentation will appear in the simulation grid.
4. Press 'Load Simulation' and load the best available simulation, or press Simulate to generate a new simulation (takes about half and hour). Simulations must have a period within ± 5 bits and a threshold within ± 0.10 for reliable pattern matching. If threshold is too high, check to see if it still is close with a lower number; as long as it is approximately representative, it will lock.
5. Set batch processing mode to 'Zero + Measure' and press 'Batch Process'. This will find the average center of the zero speed images, giving more accurate absolute readings, and then step through all the images in the folder and output to file labeled 'Results.txt' which will be placed in the same folder. These actions may be triggered individually using the respective batch processing modes.
6. Copy 'Trend_Graph.py' to the folder with this data and run it. It will then output a Torque vs. Speed graph.
7. Place the folder name of the 'Results.txt' file in the folder list in 'Unified_Trend_Graph' to add the data to a multi-set graph.
8. Place the folder name the desired control sample and of the 'Results.txt' file in the folder list in 'Unified_Trend_Graph_percent' along with to add the data to a multi-set percent reduction graph.
9. Place the folder name of the 'Results.txt' file in the folder list in 'Unified_Trend_Graph_weighted_percent' along with the desired control sample's to add the data to a multi-set weighted average percent reduction graph. This should be used in laminar flow only.

Notes:

Pythics VI will proceed if you forget to load a simulation. This can be detected by the simulated grid not moving with each image scanned, and by the process being much faster

than normal. For Zero cycle, will set nonsense number to zero. For Measure cycle, will output meaningless results. In either case, reload VI and begin again.

A.5 PCS MEASUREMENTS

A.5.1 Measurement

1. Prepare particle solution at a concentration of $0.15\frac{\mu LparticleFluid}{mLWater}$, sonicating for at least 10 min if fresh or 5 min if refilling. Particle solution should not be reused if older than 1 week or if left to sit for more than a day. Solution may be discarded down the sink. Solution should be refrigerated (not frozen) when not in use.
2. Ensure Air Bearing is off.
3. Fill tank with particle-infused water. Check for any floating dirt and pipette it out (remove as little liquid as possible). If air bubbles are an issue, empty, tilt and refill until an acceptable level is reached.
4. Place the sample on the apparatus.
5. Turn on input HeNe laser. Check that the laser beam is almost completely uniform. If visible flecks are passing through it the liquid may be degraded or dirty.
6. Ensure correlator and its computer are powered on.
7. Check that count rate is acceptable (lower the cone to near the surface and run at any speed; the count rate due to diffusion alone is not stable). If receiving 0 count rate, make sure fibre is plugged into avalanche photodiode and if it is and still receiving 0 counts, power cycle/adjust the plug on the photodiode until it turns on.
8. Finish alignment.
9. Check height and tilt are approximately correct for detector by plugging fibre into fibre-coupled laser and observing the reverse beam. It may be necessary to turn off or block the input beam temporarily to see this beam.
10. Place Plexiglas plate on threaded rods and center camera on motor. After centering, change focus to the top of the plate.

11. Angular Alignment:
    a. Turn off room lights so you can see the beams clearly using blackout curtains. In order to see the centering circles inscribed on the tank's outer ring, it may be necessary to let some light in so they are visible in photographs.
    b. Rotate and move lasers as needed. It may be necessary to detach the detector rotation stage from the linear stage for extremely large changes, as the is a limited range achievable at each position. Ensure that the input beam is not clipping on the cone of the plate.
    c. Adjust height of detector to get maximum count rate. Be aware of reflections.
    d. Run laser back through detector
    e. Take picture of Laser beams, visible in particle-infused water.
    f. Turn on room lights
    g. Transfer image to computer and open in Adobe Photoshop or GIMP.
    h. Rotate image such that input beam is horizontal. If editor attempts to crop to square, override.
    i. Carefully trace both beams using line tools.
    j. Align the corners of a rectangle object as well as possible to the inscribed circles on the tank clamp. Be sure to align to the same circle on both sides. Mark the center of rotation as the center of this rectangle. Dropping the red channel to 0% with 200% contrast can make the circles easier to see.
    k. Using measurement tools, find the angle between the beams, the distance from the center to the input beam, and the distance from the center to the intersection of the beams. Record in Measured beam parameters.txt in the folder for this test; the data processing will acquire this data from the file automatically.
12. Perform alignment as many times as needed to achieve desired parameter values. Remember to use locking screws to secure stages.
13. Plug fiber into photodiode, cover with black cloth, and ensure acceptable count rate (at least > 1 kHz). Signal should be unaffected by turning the lights on and off; if a signal change is seen, reposition cloth. Fine vertical adjustment should not throw off angular alignment.

14. Taking data:
    a. Load 'automatic_delay_series_PCS' python VI
    b. Set speed sequence and ensure parameters are correct
    c. Open https://sremote.pitt.edu/ and log in with 'Network Connection' method.
    d. Click 'Firewall-PHYAST-SSLVPN-RemoteMonitors-NetworkConnect'
    e. Start 'Network Connect'
    f. Open VNC connection to correlator computer
    g. Ensure default directory in 'save as' is pointing at desired save location. Sequence will save in whatever directory is brought up by the dialogue box. If a different directory is needed, save a dummy file and then delete it.
    h. Press start in pythics VI
    i. IMMEDIATELY change to the VNC window. Program will take control of mouse; if VNC window is not up it will then fault because it cannot find the GUI elements it is working with. If so, restart and try again.
    j. Let run. For duration of run, computer should not be used as VNC must remain on top and sequence requires mouse control.
15. In VNC, use 'Transfer Files' dialogue to move files to local computer.

Notes:

- Alignment should be checked anytime the apparatus is unscrewed.
- All samples are not the exact same height. Ensure that lasers are clear of all surfaces. Clipping the beam will cause measurement errors. Clipping can be seen in the data by a reversal or jump in the general slope as laminar flow is exited to about where turbulent flow begins.
- In order to operate the software on the remote Windows 2000 system, a package called Sikuli is used. This package uses pattern recognition to find buttons and moves the mouse to them. Scripts are programmed separately from the main python program and called from the command line using the subprocess module. Changes in how the script behaves must be done in the Sikuli GUI. While Sikuli does not lock out the mouse, it cannot register if the user has moved the mouse independently of its control, so it can fail

to function properly if the user tries to use the mouse at the same time. While running scripts, it is recommended the computer not be touched.

- Sikuli is supposed to bring the VNC window to the foreground, but a bug prevents this from working when called from python at the time of writing. Therefore, the user must ensure that after hitting the start button in pythics, the VNC window is brought to the front and left there for the remainder of the run.
- If the VNC connection stops responding properly or disconnects, restart it and continue from the last good PCS cycle. No saving will occur until the end of a cycle, so if a file exists, the data was saved.
- If cycle fails to start, hit e-stop and retry. Occasionally a residual call can become queued in the buffer and prevent the next sequence from starting properly.

A.5.2 Data Processing

1. Open 'Data_Process' pythics VI. You may load individual data runs for viewing with 'Load Data'.
2. Press 'Batch Process'. This will process all data in a folder and output results to 'Results.txt' in the same location.
3. Copy 'Trend_graph.py' into folder with these results and run it. This will generate a Shear Rate vs. Speed graph.
4. Place the name of folder name containing the 'Results.txt' file in the folder list in 'Unified_Trend_Graph' to add the data to a multi-set graph.
5. Place the folder name containing the desired control sample's 'Results.txt' file and the folder name containing the desired sample's 'Results.txt' file in the folder list in 'Unified_Trend_Graph_percent' to add the data to a multi-set percent reduction graph.

Notes:

- Batch process will not graph the individual runs; if you need to see them use 'Load Data' to load individual files. It is recommended you check at least one run each time to ensure fitting is not misbehaving.

- Batch processing will process any data files in the same folder. To exclude files, place them in a subfolder.
- Data points can be excluded from graphing by 'Trend_graph.py' by commenting them in 'Results.txt' using '#'.
- Any physical parameters not encoded in the file name or the parameter file (ie. Cone Radius, Fluid Viscosity, Index of refraction) are saved in the VI. They will reset to default values for water on each reloading of the VI unless the default is changed.
- If there is a parameter file, the VI will set the values of 'Scattering Angle', 'Measurement Position', and 'Perihelion Distance' to match what is in this file on load. To set these manually, remove the parameter file from the directory.
- The 'Low End Noise Threshold' sets the minimum time below which all data is noise from the Avalanche Photo diode. The default of 0.01 μs is good in most cases.
- Fitting uses all points between the low noise cuttoff (which eliminates shot noise from the SPCM) and the Low G Threshold (which excludes noise once the correlation has fully decayed). Fitting fits to $G_0 e^{-at} e^{-Xt^2}$, where a and X are the fitting parameters. a is discarded without use, since the linear part compensates for effects we are not examining.
- The 'Exponential Fit dV/dt' is the actual fit data, taking into account uncertainties. The linear fit information is provided as a sanity check and to help detect errors, and should not be used for reporting.
- Graph rescaling can be disengaged by unchecking 'Automatically Rescale to fit?'.

APPENDIX B

FLYING CARPETS

The Crookes Radiometer was first created by Sir William Crookes in 1874. An example of this device is shown in Fig. B.1, where the bulb is partially evacuated and each vane is typically $1cm^2$ by $0.1mm$. When exposed to light, this device is observed to spin in rough correlation to the intensity of light shone upon it, with the driving force apparently acting on the blacked surfaces. This force, on the order of 2 μN, is generated by the heat gradient resulting from the difference in absorption between the black and white surfaces; the temperature difference is on the order of 0.1-0.5 K. This force is dependent on the pressure in the vessel; for the original Crookes design it vanishes as the pressure is increased and also decreases as pressure is continually lowered past a critical point [93].

This force, referred to as a Knudsen Force, a Gas-Kinetic Force, or a Radiometric Force, is of limited value on the size scale at which first discovered. However, the fact that it functions without the need for physical connection to a motor or moving parts makes it practical for use in small devices; given the magnitude of the force, this effect is perfectly suited to providing propulsion to micro and nano-scale mechanical systems.

Radiometric forces are a non-equilibrium edge effect, the result of the flow of gas around the edge of an object under a temperature gradient, from cold to hot. This flow interacts with the surface within one mean-free-path of the edge. The remainder of the surface is inactive dead weight; this is why Crookes' model ceases to function at atmospheric pressure, where the mean-free-path is 70nm. The magnitude of the effect is also dependent on the thickness of the vane. Having a thickness equal to the mean-free-path in the gas in which the vane is immersed maximizes the force. Since this is an edge effect, the options for increasing the active/inactive surface ratio are to shrink the vane to the one mean-free-path scale or to perforate a larger vane, increasing the amount of active edge and minimizing the dead weight. We attempted to follow the latter course, producing a thin, regularly perforated vane via nano-fabrication that can generate significant force at atmospheric pressure, such that it can generate, under a reasonable heat gradient, a force sufficient to more than overcome its own weight.

Figure B.1: A Crookes Radiometer (Image from http://en.wikipedia.org/wiki/Crookes_radiometer)

B.1 THEORY OF RADIOMETRIC FORCES

Radiometric forces are primarily examined using the kinetic theory of gases. The phenomenon is an inherently non-equilibrium gas flow process, and thus statistical mechanics must be applied very carefully. A purely mathematical explanation of the effect was developed by Boltzmann, Reynolds, and Hettner, while Einstein provided a tractable qualitative model which produces the correct result to within constants [93].

B.1.1 The Physical Picture of the Force

Einstein's model of the Gas-Kinetic Force is useful for explaining physically why there is a force on the vane. We consider a vane that is free to move and has been given ample time for the sides of the vane and the gas in their vicinity to reach their respective equilibrium after having a temperature gradient placed across the vane. Looking at the gas near the surface, above and below the vane but away from the edges, the pressure must be constant. Therefore, the density must be higher on the cold side of the vane.

Within a mean free path of the edges, this requirement is broken because the particles can move around the edge, meaning that equilibrium cannot be reached so long as the temperature gradient exists, as a pressure difference between the two sides is present. Because of this pressure difference, the higher density cold particles tend to diffuse into the lower density hot region. This essentially acts as a low power jet, decreasing pressure near the edge on the cold side. Despite the higher speed of the hot molecules, they tend to be deflected back into the hot region either by the migrating cold particles or those in the cold region, due to the relatively high density. This also tends to increase the rate of collision on the hot side, which delivers more energy per impact due to temperature, further increasing the pressure from that direction. Note that these effects rapidly fall off on both sides past a single mean free path of the edge, as the remaining area of the surface is effectively an infinite sheet at equilibrium with even pressure on both sides. Using this picture, Einstein obtained the identical pressure equation to what will be derived below to within numerical constants.

B.1.2 Derivation of Gas Kinetic Forces

Following kinetic theory, the approximate first-order distribution of velocities in the presence of a temperature gradient is

$$f(\vec{v}) = \frac{\beta}{\pi}^{(3/2)} e^{-\beta(v_x^2+v_y^2+v_z^2)} \left[1 + Av_y \left(\frac{5}{2} - \beta(v_x^2 + v_y^2 + v_z^2)\right)\right] \tag{B.1}$$

where $A = \frac{15}{32n\pi\sigma^2 T}\sqrt{2\pi\beta}\frac{dT}{dy}$, n is the number density, $\beta = \frac{m}{2k_B T}$, T is the temperature, k_B is Boltzmann's Constant, m is the molecular mass and $\pi\sigma^2$ is the molecular cross section [94].

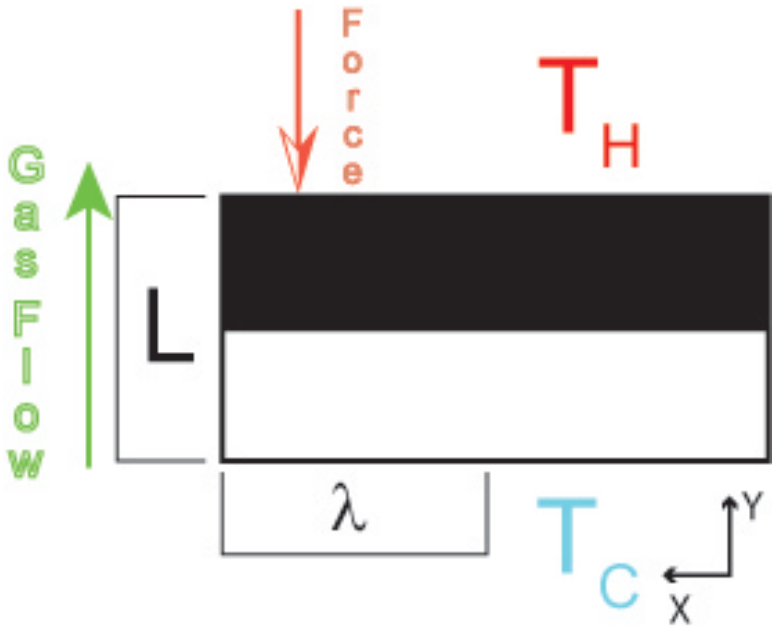

Figure B.2: Schematic Closeup of a radiometer vane edge. L is the thickness of the vane, λ is the mean free path, T_c is the colder temperature and T_h is the hotter temperature. Classical black/white painting for a vane is indicated.

Given this distribution, the pressure on a given surface in the normal direction is

$$\begin{aligned} P &= \frac{2}{A}\frac{d(p_H - p_C)}{dt} \\ &= 2nm\int_{-\infty}^{\infty} dv_x \int_{-\infty}^{\infty} dv_z \left[\int_{-\infty}^{0} dv_y v_y^2 f(\vec{v}) - \int_{0}^{\infty} dv_y v_y^2 f(\vec{v})\right] \\ &= \frac{15k\Delta T}{16\sqrt{2}\pi\sigma^2 L} \end{aligned} \tag{B.2}$$

where p is the momentum of the gas particles at the semi-infinite surface and the factor of two is added to take into account that the collisions are approximately elastic [93].

Substituting for the mean free path $\left(\lambda = \frac{k_B T}{\sqrt{2}\pi\sigma^2 P}\right)$ and the Knudsen Number $\left(Kn = \frac{\lambda}{L}\right)$, this can be re-expressed as

$$P = \frac{15nk_B\Delta T}{16L}\lambda = \frac{15nk_B\Delta T}{16}Kn \tag{B.3}$$

These integrals were taken over the entire plate. However, from Einstein's model, it is known that the central surface of the plate cannot contribute to the force. It is therefore only the area $\lambda\ell$, where ℓ is the perimeter of the vane, that contributes to the force. Accordingly the total force on a square vane [94] is

$$F = \frac{15nk_B\Delta T}{16}Kn(\lambda\ell) \tag{B.4}$$

B.1.3 Optimization

This force increases as L is decreased toward the scale of the mean free path, but it must obviously have some bounds on acceptable lengths and temperatures before the approximations become invalid. A bound on the temperature gradient can be found by examining the pressure on the cold surface alone, $P_C = \frac{nk_BT}{2} - \frac{15k_B\Delta T}{32\sqrt{2}\pi\sigma^2 L}$ (P_H is identical except for the sign). Since pressure cannot be negative in this context, this imposes an upper limit on the temperature gradient,

$$\frac{\Delta T}{L} \leq \frac{16T}{15\lambda} \tag{B.5}$$

However, if the thickness of the plate were much less than the mean free path of the gas, then the effect of the edge would become vanishing. Therefore

$$0 < \lambda \leq L. \tag{B.6}$$

Therefore, $L = \lambda$ is seen to be the optimum vane thickness.

Since the force is proportional to perimeter, a larger vane would seem to be a simple solution for increasing the force. However, increasing vane size with a simple square geometry as used by Crookes would increase vane mass far more rapidly than perimeter. Therefore, alternate geometries must be considered must to increase the force.

B.1.4 Alternative Geometry: The Perforated Vane

Looking at Einstein's explanation of the force, and with good intuitive agreement based on the above equations for the pressure, it seems clear that a fairly straightforward way to increase the force acting on the vane is to perforate it. This results in more edges at which the force can be active and simultaneously decreases the total mass. If we look at a hexagonally packed 50% area fraction array of circular holes, we can consider the force acting on one unit cell of the pattern. Then the considerations are identical as those for the preceding derivation, except that instead of the outer perimeter of a solid square, we are treating an area that is the net perimeter of the perforations. Therefore the active area is $\lambda\ell' = \lambda\frac{A}{r}$, where A is the total active area of the vane and r is the radius of the circular holes. The force from the holes is therefore [93]

$$F = \frac{15nk_B\Delta T}{16} Kn \left(\lambda\frac{A}{r}\right) \tag{B.7}$$

For a hole diameter on the order of the mean free path of a gas, which is typically nanometers, $\frac{A}{r}$ is much greater the perimeter ℓ so long as the vane is several mean free paths or greater across. Note that this requires that the material between holes and the holes themselves be at least a mean free path across, or else the derivation of the pressure becomes incorrect.

B.2 FABRICATION

We construct vanes using PAA anodized using oxalic acid. Anodization of pure Al (99.999%) in oxalic acid under proper temperature and electrical conditions results in a self-ordered hexagonal array of pores with 100nm spacing and 40nm diameter. Thickness of this oxide is easily controlled by anodization time [69]. Our target dimension is 70 nm, the average mean free path of air at room temperature (20°C), so the spacing and pore size provided by this process is nearly ideal.

At 20°C, $n \approx \frac{p}{k_B T} = 250.3477 \times 10^{21} Molecules/m^3$. Then the force available from a membrane in Newtons would be $(324.04A\Delta T)$, assuming the ideal case of $\lambda = r = L =$

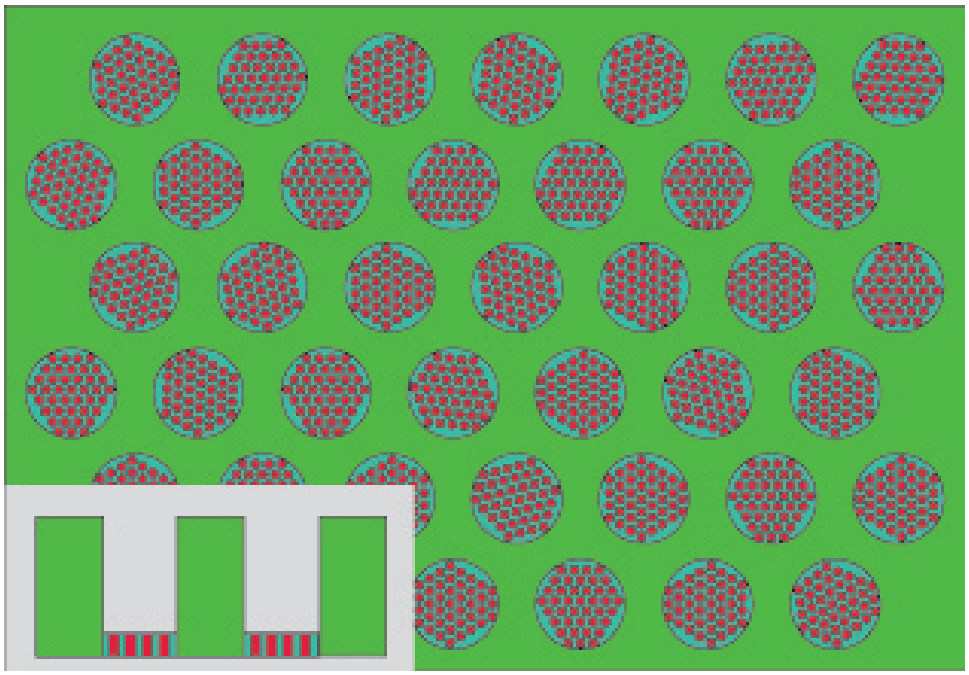

Figure B.3: Schematic top view of a perforated vane. Inset shows a schematic side view.

70 nm. If 1 mm^2 of active area can be subjected to a 0.1 K temperature difference, then a force of 32μN can theoretically be achieved, enough to lift 3.27 mg.

A large sheet of alumina on the order of 70nm thick would be unable to support its own weight. For structural integrity purposes, a much thicker inactive skeleton must be produced to support the thinner active membrane. We produce a millimeter scale hexagonal array with 50% fill fraction, on the order of 20 microns thick, and engineer in this layer indentations containing the membranes which will be our active areas. These indentations are 50 μm diameter. In order to create regions of variable thickness, we utilize 2 anodization steps. After creating the initial thick layer, we perform photolithography and etching to define through holes where our thinner oxide will reside, then reanodize briefly to grow it. We then remove the remaining aluminum and open and widen our pores. The final product is schematically represented in Fig. B.3.

B.2.1 Fabrication Process

The thick anodization is carried out over 15 hours at 40V, 20mA in 0.3 molar Oxalic acid at 6°C while the acid is being stirred at 500RPM. This produces on the order of 20μm of oxide. AZ1512 Photoresist (PR) cannot be placed directly on porous materials, because it will tend to penetrate into the pores, and PR inside the pores of such thick oxide will be nearly impossible to remove, while that on the surface will tend to delaminate. To solve this issue, we offaxis sputter coat the oxide with 180nm of W and Al. The Al is patterned using 15:1 H_2O:85% phosphoric acid [95] at 50°C and the W is imprinted with the pattern using 30% H_2O_2 [70]. The layer of Al is needed because the PR delaminates from W in H_2O_2, while a direct layer of Al could not easily be selectively removed. Note that interlayer stresses cause the Al and W to separate in etching if layer thicknesses exceed 225nm. Once the pattern has been imprinted in the coatings, the PR is removed and the open areas are etched through to the bottom. This is done by etching in phosphoric acid at 50°C, which also removes the Al coating, with 1 mL chromic acid added once the sputtered layer is cleared. The addition of chromic acid stops the etching of Al but not alumina, leaving clean, unetched aluminum at the bottom of the indentations.

We then reanodize the sample, which grows a new layer in the indented regions. This is far more controllable than trying to etch down to this thickness in the previous step, and also improves ordering in the indentations as the indentations in the underlying aluminum generated by the previous anodization act as an ordering template [96]. We widen the pores by briefly etching in Phosphoric acid at room temperature.

Wet etching in 1:2:0.4:4 $CuSO_4$:HCl:H_2O_2:H_2O on a strainer while coated with PMMA frees the membrane by dissolving the remaining Al backing. Etching in 1:1 $CuSO_4$:HCl has been successfully used in this way to separate 100nm membranes in the past [96, 97], however this leads to redepostion of Cu on the membrane, requiring careful cleaning. The additional H_2O_2 and HCl act to keep the Cu in solution, resulting in a clean membrane. Alternate methods involving the use of $FeCl_3$ have been pursued in the past, however these lead to Fe contamination (clearly visible as the membranes turn rust brown) and clogging of our porous membranes [98]. A further etch in room temperature phosphoric acid removes the

naturally occurring end caps on the pores, resulting in through holes. The PMMA is then removed, leaving porous, variable thickness, single piece alumina membranes.

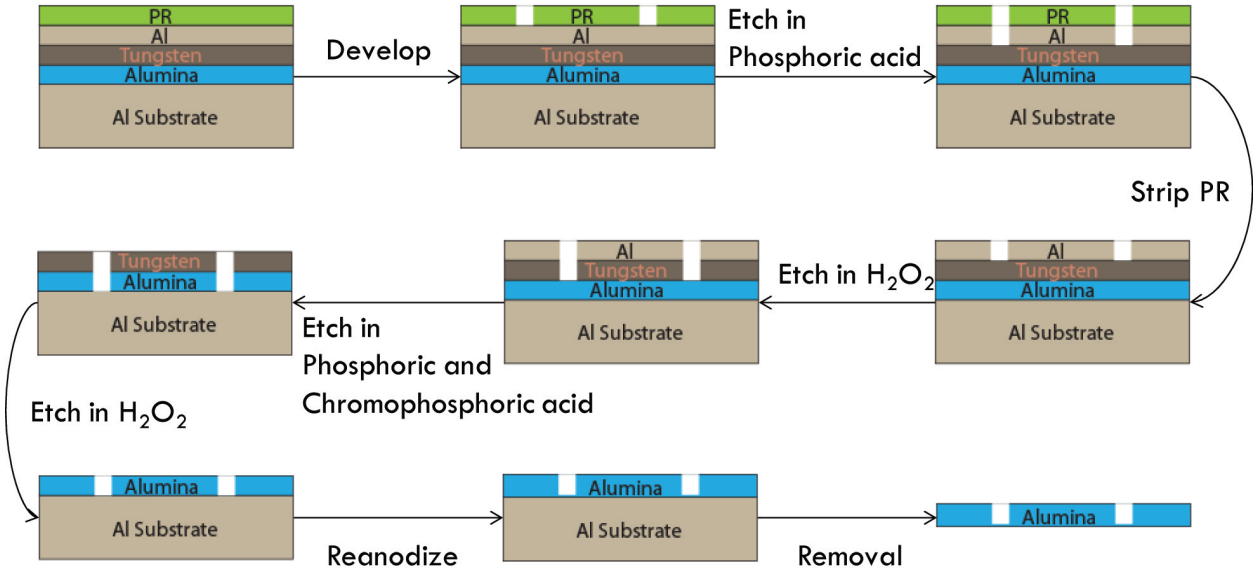

Figure B.4: Schematic of Etching Process

While this fabrication was performed successfully a few times, the fabrication method in its entirety proved to be unreliable. Consistent adhesion and thickness of the metal layers proved elusive, and patterning yielded inconsistent results. Fig B.5 shows a membrane that was successfully created, although the thickness was incorrect.

B.2.2 Heat Gradient & Measurement of the Force

A sufficiently large heat gradient must be generated in order for the effect to become observable. Ideally, simply placing the membrane on a hotplate will provide enough heating, however this will tend to simply heat the entire sample and the surrounding air evenly, whereas a gradient is require between the sides of our samples. In order to gain more control over the heating and to increase repeatability and comparability to theory, a couple different approaches were considered.

One approach would be to use laser heating. An absorbing coating would be applied to one side. However, this method has the disadvantage that it would require a specialized

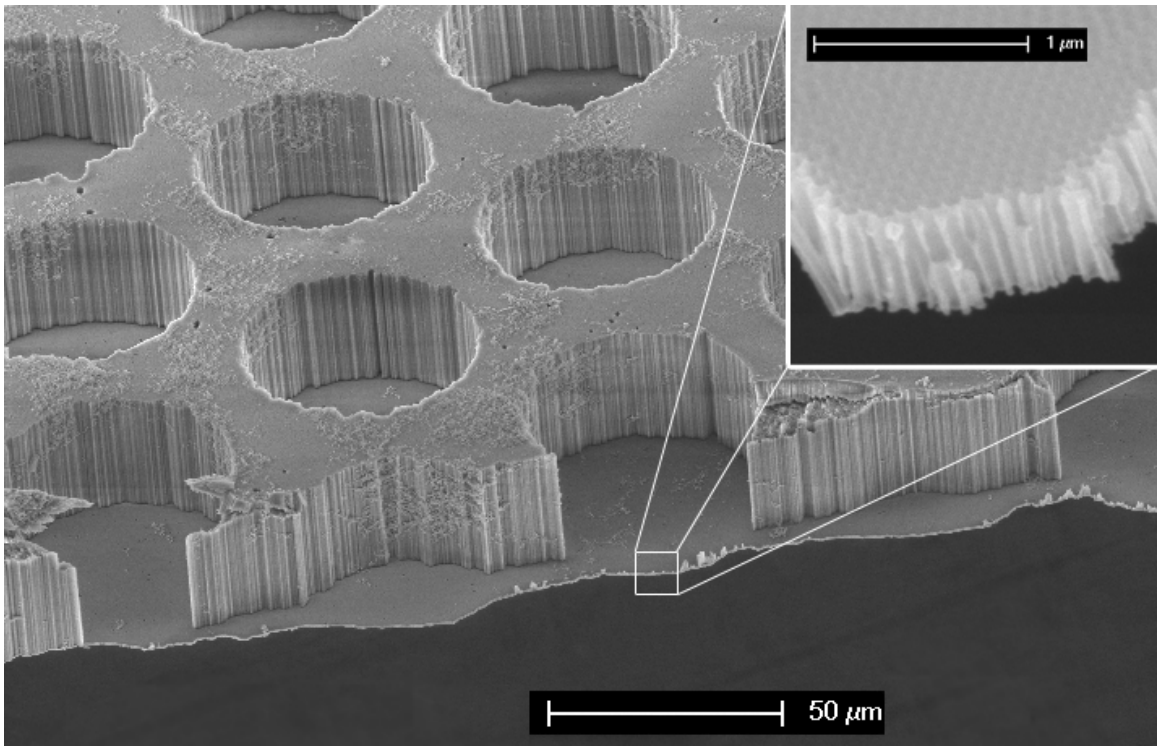

Figure B.5: SEM Image of a Variable Thickness Membrane, cracked so the cross section is visible. Thicknesses are not optimized. Inset shows a closeup of the thin region.

stage in order to give the beam access to the lower side if we wish to apply the force in the upward direction. One way to read the temperature induced by the laser could be to use thermo-florescent phosphors as the absorber [99, 100].

Another approach considered would use a metal coating to absorb microwaves and heat the membrane. This may be more useful as it does not require optical access, however it is harder to determine the temperature gradient being produced. The difficulty lies in determining how much microwave energy is being converted into heat.

The method used to measure the force is dependent on the magnitude of the force we are able to achieve. In the ideal case, the force would be large enough to generate significant lift. In this case the force can be simply determined by utilizing a micro-balance in order to measure the changes in the measured weight of the membrane. If the force proved to be

much smaller than anticipated, it would be necessary to utilize a torsion pendulum system capable of measuring a minute displacement of the membrane when it is heated. This will be more difficult to translate into a force measurement. The sample could be suspended from a wire of known torsional stiffness and the displacement measured using laser interferometry. This would be made more difficult by the fragility of the membranes.

B.3 OUTCOME

We chose not to continue this work in light of the difficulties in the fabrication. Anodization and etching techniques and lessons learned were used as the basis for the techniques detailed in Chapter 3.

APPENDIX C

DROP BEARINGS

Friction between contacting solid surfaces is a dominant force on the micro-scale and a major consideration in the design of Micro-Electro-Mechanical Systems (MEMS). Non-contact fluid bearings have been investigated as a way to mitigate this issue. Here we discuss a new design for surface tension-supported thrust bearings utilizing patterned Superhydrophobic surfaces. We examine sources of instability in the design, and demonstrate that it can be simply modeled and has superior stiffness as compared to other designs.

C.1 INTRODUCTION

MEMS are increasingly finding practical application. Friction from solid-solid contacts in bearings and hinges can lead to device failure or breakage, so practical devices have primarily used flexing components, such as cantilevers, rather than rotating shafts and gears, which are common in macro-scale devices. Frictional concerns are one of the primary obstacles to using rotating components for MEMS [101]. In macroscopic devices, air bearings with an actively injected lubricating gas layer or journal bearings with a dynamically maintained lubricant film are used in high-performance applications, but engineering such intricate structures is challenging in MEMS [102]. The use of surface tension to maintain a liquid lubricant layer is an alternative that is most effective in MEMS, since surface tension is very significant in microscopic devices. Furthermore, surface tension and fluid pressure at these scales can actually be used to passively support a MEMS bearing, eliminating all solid-solid contact. In such bearings, a liquid, usually water or an aqueous solution, is used between the two solid surfaces. Variations in surface wetting (e.g. hydrophobicity) are used to pin the liquid in position. The liquid-solid contact is low friction compared to solid-solid contacts, allowing parts to slide with less stiction and lower wear [6].

Surface tension supported liquid bearings with a variety of geometries have been investigated. In the simplest case, a single drop of water trapped between identical hydrophilic pads in the center of the bearing (Fig. C.1a) supports the rotating part (rotor) above the stationary substrate (stator). Wear is reduced due to the lack of solid contact and concentricity of the pads is well maintained by surface tension, but the tilt stability is poor, as there

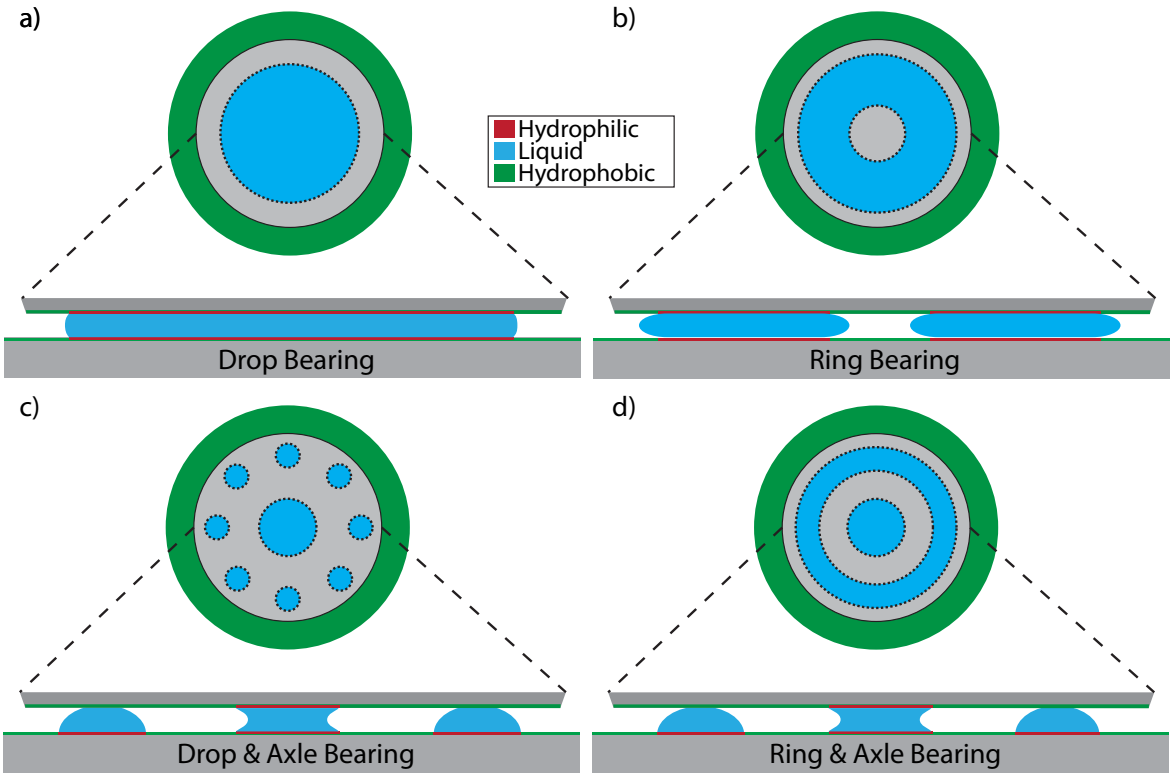

Figure C.1: Liquid bearing configurations, showing top view and cross section.

is little energetic cost to tipping the rotor even to the point of a collision between the rotor and stator. Using a ring of water reduces the hydrodynamic drag on the surfaces somewhat by reducing the wetted surface area (Fig. C.1b), and has increased tilt stiffness [7]. The tilt stiffness can be greatly increased by breaking up the wetting ring into discrete drops and making the rotor Superhydrophobic, as in Fig. C.1c. Since the drops do not wet to the rotor surface, a central drop, which wets to both sides, is added to the center to maintain the relative positions of the surfaces. The decreased contact area between the water and solid can reduce the hydrodynamic drag, and the superhydrophobic contacts provide high lifting forces and reduce titling, but energy loss due to the remaining contact angle hysteresis of the superhydrophobic surface may dominate the sources of drag [103].

The ideal surface tension supported liquid bearing would provide high stiffness in all directions while minimizing all sources of drag. Our work investigated a new ring and axle

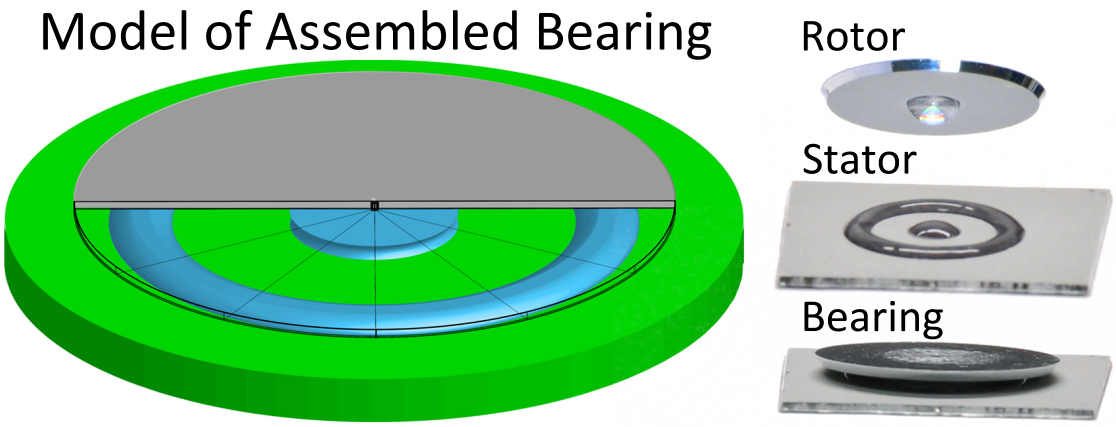

Figure C.2: A model of ring and axle liquid bearing, with photographs of a rotor, stator and assembled bearing. The model rotor is rendered as partially transparent so the liquid pattern can be seen.

bearing design (Fig. C.1d and Fig. C.2), which combines several of the best features of other designs. The design uses a central drop, which wets hydrophilic areas on both the rotor and the stator, as an axle. The axle holds the rotor down and keeps the rotor concentric with the stator. A ring of water is wetted to a hydrophilic annulus on the stator, while the surface of the rotor in contact with the ring is superhydrophobic. The ring provides a vertical force to balance that of the axle, and stiffens the bearing with respect to tilting. Since there is no wetting and dewetting in the system as the rotor spins, there are no hysteretic losses. This new ring and axle liquid bearing design is not unconditionally stable, e.g. the ring will actually push the rotor to tilt if it is overfilled with water. Here, we examine this system and determine the parametric region of stability.

The axle and ring each generally provide two contributions to the forces acting on the rotor: the force due to Laplace pressure, which is the result of the pressure difference across the liquid surface, and the force directly due to surface tension of the water acting on the rotor. Even in the simplest cases, calculating the stability and stiffness of the bearing analytically is not trivial, and numerical solution is more practical. We examine the bearings via numerical modeling using energy minimization [104].

C.2 MODELING

We performed simulations of our bearings using Surface Evolver [105], an open source finite element analysis system. Surface Evolver minimizes the energy of the liquid surface subject to constraints, which include the size and contact angles of the wetting and non-wetting surfaces, and the volume of liquid in each region. The effect of gravity is also included, using experimental values for the mass of the rotor. Only the liquid surface was directly modeled; the rotor and stator were represented by boundary conditions and constraints. Typically, the distance between the rotor and stator is allowed to vary, but the angle of the rotor is fixed in any one calculation. The stiffness of the bearing and the equilibrium tilt angle were calculated by displacing the rotor vertically or tilting the rotor while adjusting the liquid-air interface to minimize energy. The tilt with the minimum energy was recorded as the equilibrium tilt, while the curvature of the energy versus height or tilt was used to calculate the stiffness. An example of a generated liquid surface mesh can be seen in Fig. C.4.

Not all combinations of constraints resulted in physically realizable bearing configurations. In the model, a configuration was considered unstable if either the center drop separated or the contact of the ring of water on the upper surface vanished at any point during the calculation. For a range of axle and ring volumes, the model was used to determine if the configuration would be stable and, if stable, the equilibrium rotor height, tilt, and tilt stiffness.

C.3 FABRICATION

To verify the validity of the model, the bearing design was also experimentally tested. We fabricated Superhydrophobic surfaces on thin 2 in foil, for use as rotors, and 2 in discs, for use as stators, using the method detailed in Chapter 3 (these methods were initially developed here). The stator ring and axle hydrophilic areas were patterned by coating the Superhydrophobic surface with photoresist and sputter-depositing Ti, then performing lift off, to form a 1.25 mm radius circular hydrophilic region for the axle and an annular

hydrophilic region with an average 3.35 mm radius and a width of 1.4 mm. SPDT was then used to cut out 1 cm diameter rotors from 0.5 mm thick discs with a superhydrophobic surface produced by the same method. SPTD was also used to remove the superhydrophobic structure in a 1.25 mm radius circle at the center of the rotor to create a matching hydrophilic circle for the axle water to wet. The rotor hydrophilic area was defined by SPDT instead of photolithography to guarantee concentricity of the rotor edge and the axle to within the accuracy of the ultra-precision lathe used for SPDT (< 100 nm). A rotor and stator pair are shown in Fig. C.2.

C.4 EXPERIMENTAL

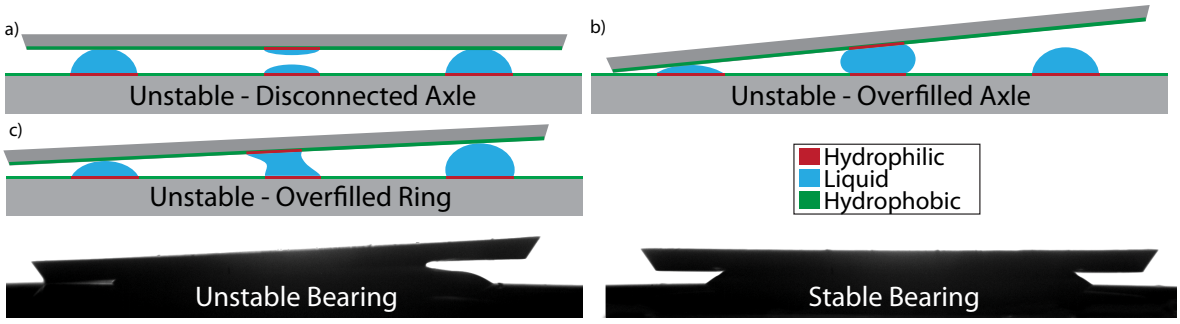

Figure C.3: Illustration of possible unstable bearing states. Images of a failed and a functional bearing are shown below.

Experimentally, the bearings were photographed in profile over a range of center and ring liquid volumes (examples shown in Fig. C.3). The parts were allowed to completely dry between tests to minimize fluid volume uncertainties, and the ring and axle hydrophilic regions were filled with water just before placement to minimize evaporation. To achieve full wetting of both axle pads reliably with such small volumes of water, half of the volume had to be placed on each side. Rotors were handled by vacuum tweezers from the back side to ensure that the superhydrophobic surfaces were not damaged. After placement of the rotor, the entire bearing was carefully rotated to ensure that the image was taken in profile

perpendicular to the tilt. Image analysis was then used to find the height and angle of tilt.

In both experiments and models, we find that there are several possible sources of instability. If the axle has insufficient liquid relative to the ring, the liquid on the rotor and stator will not join to form an axle or will re-separate due to the lift from the ring with most of the water on one side, and the rotor will not remain centered (Fig. C.3a). If the liquid in the ring is insufficient relative to the axle, then the rotor is lifted partially off of the ring and tips to one side, since balancing on the center drop alone is unstable (Fig. C.3b). Finally, if the ring has too much water in it, it bulges asymmetrically, again resulting in a tilted (and often off-center) rotor (Fig. C.3c).

Fig. C.4 shows the results of experiments and models with the same range of axle and ring volumes. There is an exact match between the predicted and measured regions of stability. This shows that a simple model can predict the stable range of parameters for the bearing. There are unstable regions to the left and right of the stable volume regions in Fig. C.4. The upper left unstable region is caused by too much liquid in the ring compared to that in the axle, resulting in a bulge in the ring or separation of the axle. The lower right unstable region results from too much liquid in the axle compared to that in the ring, resulting in the rotor tipping over.

The experimentally measured and numerically modeled rotor heights show reasonable agreement. Both show increasing height of the rotor with increasing volume in either the axle or the ring. Quantitatively, the results agree to within 30% with no free parameters in the model. The results for the rotor tilt show less agreement between the experiments and model. The model predicts effectively no tilt in the stable region, while experimentally measurable tilt is observed, particularly near the high ring volume and low axle volume boundary of the stable region. This experimental tilt seems to fluctuate without any clear trend, and is not highly repeatable. It is likely that experimentally this results from the assembly process of the bearing, where the bearing is not guaranteed to start off with zero tilt; i.e. near the edge of the stable region, there may be some hysteresis in the tilt.

With some evidence that the model is accurate, we can then predict the stiffness of the bearing with respect to tilt (vertical stiffness is not generally difficult to achieve, and thus is not analyzed). The results, calculated from the dependence of the energy of the system

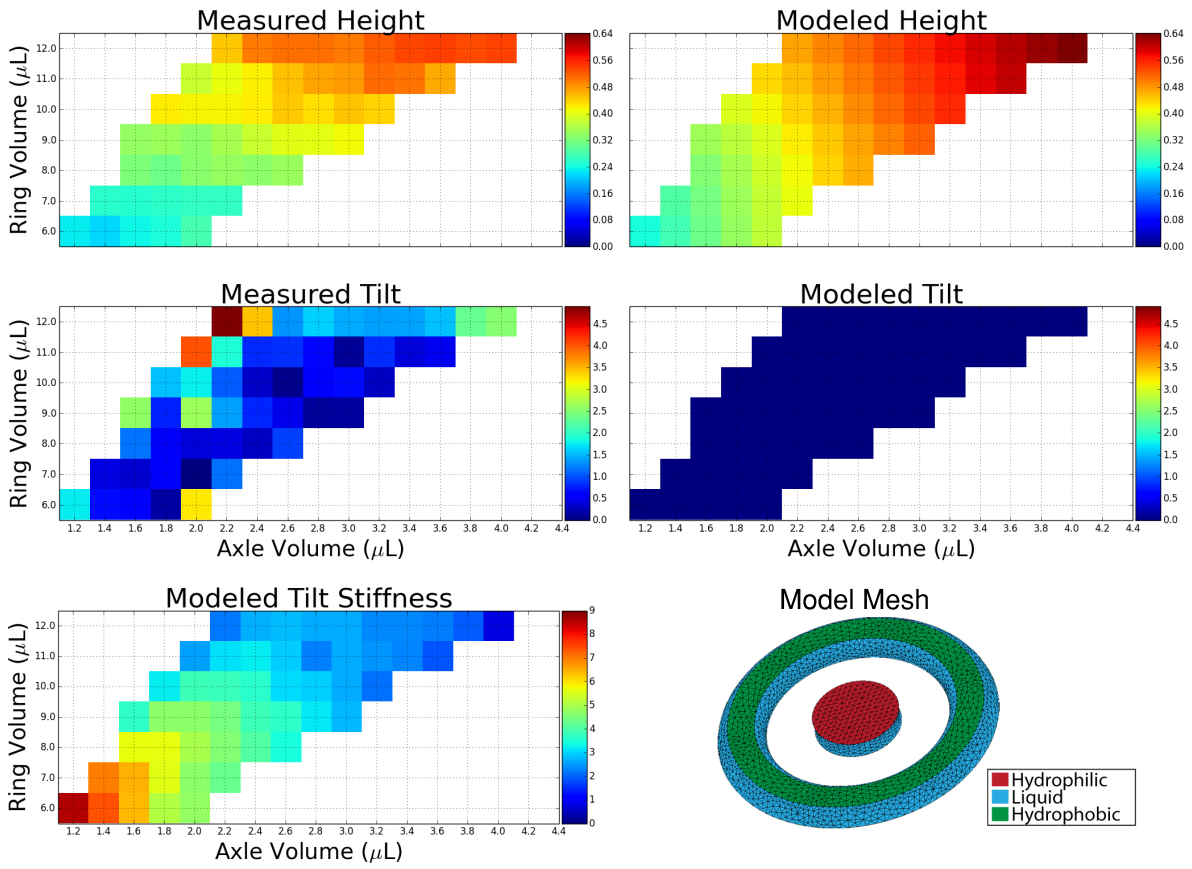

Figure C.4: Graphs of height and tilt angle for the examined ring and axle volumes, where the color axes are height in mm and tilt in degrees, respectively. The stable regions match between the experiments and model, although particular tilt angle is not well correlated. We also show modeled tilt stiffness, where the color axis is k in nJ/degree^2, and an example of our model mesh, which directly simulates only the liquid surface (solid contacts are represented by constraints).

on tilt, are shown in Fig. C.4. As a comparison, for a single bearing thicknesses (0.38 mm), a model drop bearing has a spring constant of 0.32 nJ/degree^2 (drop covers the same area as the full ring and axle bearing), a ring bearing has a spring constant of 0.34 nJ/degree^2 (ring inner radius equal to the outer radius of th axle of the ring and axle bearing), and a ring and axle bearing has a spring constant of 2.55 nJ/degree^2, which represents a significant

improvement. The tilt stiffness of ring and axle bearings is calculated to generally increase with decreasing volume of liquid in either the axle or ring. It is likely that having less liquid in the ring directly increases the stiffness, while less liquid in the axle pulls the rotor closer to the stator and compresses the ring, increasing its stiffness.

C.5 OUTCOMES

Surface tension supported ring and axle bearings have significant potential for use in MEMS due to their low frictional losses and complete lack of solid on solid contact. These results demonstrate that these devices are stable over a large range of ring and axle volumes, and that this region can be modeled using energy minimization, simplifying design and experimental work with these devices. It also shows that these devices have a higher spring constant for a given size than alternative designs.

A common objection to water-based liquid bearings is that, while promising from a mechanics standpoint, the evaporation of the liquid water makes them of limited practical use. Although the testing presented here was performed with pure water, we have also tested longer term use of a saturated water-$CaCl_2$ solution on superhydrophobic surfaces with patterned hydrophilic regions. This solution has similar surface tension to pure water and since $CaCl_2$ is deliquescent, it can actually pull moisture from the air, rather than allowing the water to evaporate. In practice, this solution was stable over a period of at least a year under ambient conditions, and shows no signs of evaporation or corrosion of the underlying surface.

These bearings were originally developed for the purpose of demonstrating effective low drag microscopic systems. Initial plans to measure the deceleration of our bearings using a high speed camera in order to quantify drag had issues with consistently assembling the bearing and getting it up to speed without introducing instability into the system. Methods considered for spinning up the rotors included spinning up the stator and then suddenly stopping it or adding magnets to the rotors and spinning up using magnetic torque (the reverse of this would eventually be applied to our torque system). Sample durability also

proved to be a challenge, as the need to continually remove and replace the rotors revealed that our surfaces needed further refinement (see Chapter 3.1.2). Attempts at scaling the process down also revealed that we were at the lowest size our fabrication method for the rotors could tolerate; there was too little surface area for them to be held on the diamond turning machine chuck reliably when they were shrunk further. Thus we would have had to completely redesign our fabrication to reduce the size of the bearings. It was therefore decided to pursue a project that we could achieve with our current surfaces and fabrication method.

BIBLIOGRAPHY

[1] M. E. McCormick, R. Bhattacharyya, Drag reduction of a submersible hull by electrolysis, Naval Engineers Journal 85 (2) (1973) 11–16.

[2] R. Blossey, Self-cleaning surfacesvirtual realities, Nature materials 2 (5) (2003) 301–306.

[3] M. Graham, Drag reduction and the dynamics of turbulence in simple and complex fluids, Bulletin of the American Physical Society 58.

[4] E. Burger, L. Chorn, T. Perkins, Studies of drag reduction conducted over a broad range of pipeline conditions when flowing prudhoe bay crude oil, Journal of Rheology (1978-present) 24 (5) (1980) 603–626.

[5] C.-M. Ho, Y.-C. Tai, Micro-electro-mechanical-systems (mems) and fluid flows, Annual Review of Fluid Mechanics 30 (1) (1998) 579–612.

[6] K. Hiratsuka, A. Bohno, H. Mendo, Water droplet lubrication for micromachines, Tribology Letters 43 (3) (2007) 423–428.

[7] M. L. Chan, B. Yoxall, H. Park, Z. Kang, I. Izyumin, J. Chou, M. M. Megens, M. C. Wu, B. E. Boser, D. A. Horsley, Design and characterization of mems micromotor supported on low friction liquid bearing, Sensors and Actuators A: Physical 177 (2012) 1–9.

[8] B. R. Elbing, E. S. Winkel, K. A. Lay, S. L. Ceccio, D. R. Dowling, M. Perlin, Bubble-induced skin-friction drag reduction and the abrupt transition to air-layer drag reduction, Journal of Fluid Mechanics 612 (2008) 201–236.

[9] K. Fukuda, J. Tokunaga, T. Nobunaga, T. Nakatani, T. Iwasaki, Y. Kunitake, Frictional drag reduction with air lubricant over a super-water-repellent surface, Journal of Marine Science and Technology 5 (3) (2000) 123–130.

[10] G. K. Patterson, J. L. Zakin, J. Rodriguez, Drag reduction-polymer solutions, soap solutions, and solid particle suspensions in pipe flow, Industrial & Engineering Chemistry 61 (1) (1969) 22–30.

[11] L.-G. Stenberg, T. Lagerstedt, E. R. Lindgren, Polymer additive mixing and turbulent drag reduction, Physics of Fluids (1958-1988) 20 (10) (1977) S276–S279.

[12] D. Quéré, Wetting and roughness, Annu. Rev. Mater. Res. 38 (2008) 71–99.

[13] P.-G. De Gennes, Wetting: statics and dynamics, Reviews of modern physics 57 (3) (1985) 827.

[14] J. Jopp, H. Grüll, R. Yerushalmi-Rozen, Wetting behavior of water droplets on hydrophobic microtextures of comparable size, Langmuir 20 (23) (2004) 10015–10019.

[15] J. Bico, U. Thiele, D. Quéré, Wetting of textured surfaces, Colloids and Surfaces A: Physicochemical and Engineering Aspects 206 (1) (2002) 41–46.

[16] C. Neinhuis, W. Barthlott, Characterization and distribution of water-repellent, self-cleaning plant surfaces, Annals of Botany 79 (6) (1997) 667–677.

[17] W. Barthlott, C. Neinhuis, Purity of the sacred lotus, or escape from contamination in biological surfaces, Planta 202 (1) (1997) 1–8.

[18] H. Wang, D. Dai, X. Wu, Fabrication of superhydrophobic surfaces on aluminum, Applied Surface Science 256.

[19] L. Zhai, F. C. Cebeci, R. E. Cohen, M. F. Rubner, Stable superhydrophobic coatings from polyelectrolyte multilayers, Nano Letters 4 (7) (2004) 1349–1353.

[20] K. Liu, L. Jiang, Metallic surfaces with special wettability, The Annual Review of Materials Research 42.

[21] N. Tasaltin, D. Sanli, A. Jonáš, A. Kiraz, C. Erkey, Preparation and characterization of superhydrophobic surfaces based on hexamethyldisilazane-modified nanoporous alumina, Nanoscale research letters 6 (1) (2011) 1–8.

[22] J. T. Han, D. H. Lee, C. Y. Ryu, K. Cho, Fabrication of superhydrophobic surface from a supramolecular organosilane with quadruple hydrogen bonding, Journal of the American Chemical Society 126 (15) (2004) 4796–4797.

[23] X. Yao, Q. Chen, L. Xu, Q. Li, Y. Song, X. Gao, D. Quéré, L. Jiang, Bioinspired ribbed nanoneedles with robust superhydrophobicity, Advanced Functional Materials 20 (4) (2010) 656–662.

[24] W.-L. Min, B. Jiang, P. Jiang, Bioinspired self-cleaning antireflection coatings, Advanced Materials 20 (20) (2008) 3914–3918.

[25] B. Bhushan, Y. C. Jung, Micro-and nanoscale characterization of hydrophobic and hydrophilic leaf surfaces, Nanotechnology 17 (11) (2006) 2758.

[26] X. Gao, L. Jiang, Biophysics: water-repellent legs of water striders, Nature 432 (7013) (2004) 36–36.

[27] E. Bormashenko, Y. Bormashenko, T. Stein, G. Whyman, E. Bormashenko, Why do pigeon feathers repel water? hydrophobicity of pennae, cassie–baxter wetting hypothesis and cassie–wenzel capillarity-induced wetting transition, Journal of colloid and interface science 311 (1) (2007) 212–216.

[28] H.-Y. Kim, H. J. Lee, B. H. Kang, Sliding of liquid drops down an inclined solid surface, Journal of colloid and interface science 247 (2) (2002) 372–380.

[29] G. McHale, N. Shirtcliffe, M. Newton, Contact-angle hysteresis on super-hydrophobic surfaces, Langmuir 20 (23) (2004) 10146–10149.

[30] R. Truesdell, A. Mammoli, P. Vorobieff, F. van Swol, C. J. Brinker, Drag reduction on a patterned superhydrophobic surface, Physical Review Letters 97.

[31] C. Barbier, E. Jenner, B. DUrso, Drag reduction with superhydrophobic riblets, in: ASME 2012 International Mechanical Engineering Congress and Exposition, American Society of Mechanical Engineers, 2012, pp. 199–205.

[32] V. Zorba, E. Stratakis, M. Barberoglou, E. Spanakis, P. Tzanetakis, S. H. Anastasiadis, C. Fotakis, Biomimetic artificial surfaces quantitatively reproduce the water repellency of a lotus leaf, Advanced Materials 20 (21) (2008) 4049–4054.

[33] T.-S. Wong, S. H. Kang, S. K. Tang, E. J. Smythe, B. D. Hatton, A. Grinthal, J. Aizenberg, Bioinspired self-repairing slippery surfaces with pressure-stable omniphobicity, Nature 477 (7365) (2011) 443–447.

[34] M. Nosonovsky, Materials science: Slippery when wetted, Nature 477 (7365) (2011) 412–413.

[35] R. J. Daniello, N. E. Waterhouse, J. P. Rothstein, Drag reduction in turbulent flows over superhydrophobic surfaces, Physics of Fluids (1994-present) 21 (8) (2009) 085103.

[36] C.-H. Choi, C.-J. Kim, Large slip of aqueous liquid flow over a nanoengineered superhydrophobic surface, Physical review letters 96 (6) (2006) 066001.

[37] C. Extrand, Designing for optimum liquid repellency, Langmuir 22 (4) (2006) 1711–1714.

[38] M. Callies, D. Quéré, On water repellency, Soft matter 1 (1) (2005) 55–61.

[39] N. A. Patankar, Mimicking the lotus effect: influence of double roughness structures and slender pillars, Langmuir 20 (19) (2004) 8209–8213.

[40] L. Vogelaar, R. G. H. Lammertink, M. Wessling, Superhydrophobic surfaces having two-fold adjustable roughness prepared in a single step, Langmuir 22.

[41] N. J. Shirtcliffe, G. McHale, M. I. Newton, G. Chabrol, C. C. Perry, Dual-scale roughness produces unusually water-repellent surfaces, Advanced Materials 16 (21) (2004) 1929–1932.

[42] T. Onda, S. Shibuichi, N. Satoh, K. Tsujii, Super-water-repellent fractal surfaces, Langmuir 12 (9) (1996) 2125–2127.

[43] Y. Su, B. Ji, K. Zhang, H. Gao, Y. Huang, K. Hwang, Nano to micro structural hierarchy is crucial for stable superhydrophobic and water-repellent surfaces, Langmuir 26 (7) (2010) 4984–4989.

[44] K. Fukagata, N. Kasagi, P. Koumoutsakos, A theoretical prediction of friction drag reduction in turbulent flow by superhydrophobic surfaces, Physics of Fluids (1994-present) 18 (5) (2006) 051703.

[45] X. Gao, X. Yao, L. Jiang, Effects of rugged nanoprotrusions on the surface hydrophobicity and water adhesion of anisotropic micropatterns, Langmuir 23 (9) (2007) 4886–4891.

[46] B. D'Urso, J. Simpson, M. Kalyanaraman, Emergence of superhydrophobic behavior on vertically aligned nanocone arrays, Applied physics letters 90 (4) (2007) 044102.

[47] E. Jenner, C. Barbier, B. DUrso, Durability of hydrophobic coatings for superhydrophobic aluminum oxide, Applied Surface Science 282 (2013) 73–76.

[48] E. Jenner, B. D'Urso, Wetting states on structured immiscible liquid coated surfaces, Applied Physics Letters 103 (25) (2013) 251606.

[49] S. Stefanus, S. Steers, W. Goldburg, Direct measurement of turbulent shear, Physica D: Nonlinear Phenomena 240 (23) (2011) 1873–1876.

[50] D. P. Chowdhury, C. M. Sorensen, T. Taylor, J. Merklin, T. Lester, Application of photon correlation spectroscopy to flowing brownian motion systems, Applied optics 23 (22) (1984) 4149–4154.

[51] G. Fuller, J. Rallison, R. Schmidt, L. Leal, The measurement of velocity gradients in laminar flow by homodyne light-scattering spectroscopy, Journal of Fluid Mechanics 100 (03) (1980) 555–575.

[52] C. W. Macosko, R. G. Larson, Rheology: principles, measurements, and applications, VCH New York, 1994.

[53] H. A. Barnes, J. F. a. Hutton, An introduction to rheology, Vol. 3, Elsevier, 1989.

[54] S. Wang, L. Jiang, Definition of superhydrophobic states, Advanced Materials 19.

[55] A. Lafuma, D. Quéré, Superhydrophobic states, Nature Materials 2 (7) (2003) 457–460.

[56] R. N. Wenzel, Resistance of solid surfaces to wetting by water, Industrial & Engineering Chemistry 28 (8) (1936) 988–994.

[57] X.-M. Li, D. Reinhoudt, M. Crego-Calama, What do we need for a superhydrophobic surface? a review on the recent progress in the preparation of superhydrophobic surfaces, Chemical Society Reviews 36 (8) (2007) 1350–1368.

[58] K. Liu, X. Yao, L. Jiang, Recent developments in bio-inspired special wettability, Chemical Society Reviews 39 (8) (2010) 3240–3255.

[59] A. Cassie, S. Baxter, Wettability of porous surfaces, Transactions of the Faraday Society 40 (1944) 546–551.

[60] X. Feng, L. Jiang, Design and creation of superwetting/antiwetting surfaces, Advanced Materials 18 (23) (2006) 3063–3078.

[61] L. Cao, H.-H. Hu, D. Gao, Design and fabrication of micro-textures for inducing a superhydrophobic behavior on hydrophilic materials, Langmuir 23 (8) (2007) 4310–4314.

[62] D. L. Schmidt, R. F. Brady, K. Lam, D. C. Schmidt, M. K. Chaudhury, Contact angle hysteresis, adhesion, and marine biofouling, Langmuir 20 (7) (2004) 2830–2836.

[63] A. Lafuma, D. Quéré, Slippery pre-suffused surfaces, EPL (Europhysics Letters) 96 (5) (2011) 56001.

[64] P. Kim, M. J. Kreder, J. Alvarenga, J. Aizenberg, Hierarchical or not? effect of the length scale and hierarchy of the surface roughness on omniphobicity of lubricant-infused substrates, Nano lett. 13 (4) (2013) 1793–1799.

[65] A. K. Epstein, T.-S. Wong, R. A. Belisle, E. M. Boggs, J. Aizenberg, Liquid-infused structured surfaces with exceptional anti-biofouling performance, Proceedings of the National Academy of Sciences 109 (33) (2012) 13182–13187.

[66] J. Davenport, R. N. Hughes, M. Shorten, P. S. Larsen, Drag reduction by air release promotes fast ascent in jumping emperor penguins - a novel hypothesis, Mar Ecol Prog Ser 430 (2011) 171–182.

[67] M. Nosonovsky, B. Bhushan, Biomimetic superhydrophobic surfaces: multiscale approach, Nano letters 7 (9) (2007) 2633–2637.

[68] H.-S. Kim, E.-J. Kim, Feed-forward control of fast tool servo for real-time correction of spindle error in diamond turning of flat surfaces, International Journal of Machine Tools and Manufacture 43 (12) (2003) 1177–1183.

[69] S. Chu, K. Wada, S. Inoue, M. Isogai, Y. Katsuta, A. Yaumori, Large-scale fabrication of ordered nanoporous alumina films with arbitrary pore intervals by critical-potential anodization, Journal of The Electrochemical Society 153 (2006) B384–B391.

[70] K. R. Williams, K. Gupta, M. Wasilik, Etch rates for micromachining processing - part ii, IEEE: Journal Of Microelectromechanical Systems 12 (6) (2003) 761–778.

[71] T. Yanagishita, K. Yasui, T. Kondo, Y. Kawamoto, K. Nishio, H. Masuda, Antireflection polymer surface using anodic porous alumina molds with tapered holes, Chemistry Letters 36 (4) (2007) 530–531.

[72] T. Yanagishita, T. Kondo, K. Nishio, H. Masuda, Optimization of antireflection structures of polymer based on nanoimprinting using anodic porous alumina, Journal of Vacuum Science and Technology 26 (6) (2008) 1856–1859.

[73] G. Alberti, A. DeSimone, Wetting of rough surfaces: a homogenization approach, Proceedings of the Royal Society A 461.

[74] H. Yang, V. N. Luk, M. Abelgawad, I. Barbulovic-Nad, A. R. Wheeler, A world-to-chip interface for digital microfluidics, Analytical Chemistry 81.

[75] M. J. Pellerite, E. J. Wood, V. W. Jones, Dynamic contact angle studies of self-assembled thin films from fluorinated alkyltrichlorosilanes 1, The Journal of Physical Chemistry B 106 (18) (2002) 4746–4754.

[76] J. Brzoska, I. B. Azouz, F. Rondelez, Silanization of solid substrates: a step toward reproducibility, Langmuir 10 (11) (1994) 4367–4373.

[77] X. Zhang, F. Shi, J. Niu, Y. Jiang, Z. Wang, Superhydrophobic surfaces: from structural control to functional application, Journal of Materials Chemistry 18.

[78] G. Comte-Bellot, Hot-wire anemometry, Annual review of fluid mechanics 8 (1) (1976) 209–231.

[79] R. J. Adrian, R. J. Goldstein, Analysis of a laser doppler anemometer, Journal of Physics E: Scientific Instruments 4 (7) (1971) 505.

[80] J. Wills, The correction of hot-wire readings for proximity to a solid boundary, Journal of Fluid Mechanics 12 (03) (1962) 388–396.

[81] J. C. Bhatia, F. Durst, J. Jovanovic, Corrections of hot-wire anemometer measurements near walls, Journal of Fluid Mechanics 122 (1982) 411–431.

[82] H. Sdougos, S. Bussolari, C. Dewey, Secondary flow and turbulence in a cone-and-plate device, Journal of Fluid Mechanics 138 (1984) 379–404.

[83] B. Chu, Laser light scattering, Elsevier, 1974.

[84] K. Kataoka, Y. Shibayama, M. Ohuchi, S. Yokokawa, Laser printer optics with use of slant scanning of multiple beams, Applied optics 36 (25) (1997) 6294–6307.

[85] P. Tong, W. Goldburg, C. Chan, A. Sirivat, Turbulent transition by photon-correlation spectroscopy, Physical Review A 37 (6) (1988) 2125.

[86] A. Einstein, On the movement of small particles suspended in stationary liquids required by the molecular-kinetic theory of heat, Annalen der Physik 17 (549-560) (1905) 16.

[87] J. W. Dufty, Diffusion in shear flow, Physical Review A 30 (3) (1984) 1465.

[88] R. Cerbus, personal communication.

[89] TAInstruments.
URL http://www.tainstruments.com

[90] J. Powell, Design of aerostatic bearings, Machinery's Books for Engineers, Machinery Publishing, 1970.
URL https://openlibrary.org/books/OL21500483M/The_design_of_aerostatic_bearings

[91] W. H. Snyder, J. Lumley, Some measurements of particle velocity autocorrelation functions in a turbulent flow, Journal of Fluid Mechanics 48 (01) (1971) 41–71.

[92] D. Bechert, M. Bruse, W. Hage, J. T. Van der Hoeven, G. Hoppe, Experiments on drag-reducing surfaces and their optimization with an adjustable geometry, Journal of Fluid Mechanics 338 (1997) 59–87.

[93] M. Scandurra, Enhanced radiometric forces, arXiv:physics.

[94] M. Scandurra, F. Iacopetti, P. Colona, Gas kinetic forces on thin plates in the presence of thermal gradients, Physical Review.

[95] B. Zhou, W. F. Ramirez, Kinetics and modeling of wet etching of aluminum oxide by warm phosphoric acid, The Electrochemical Society 143 (2) (1996) 619–623.

[96] A. Shing, M. Chong, L. K. Tan, J. Deng, H. Gaor, Soft imprinting: Creating highly ordered porous anodic alumina templates on substrates for nanofabrication, Advanced Functional Materials 17 (2007) 1629–1635.

[97] G. Q. Ding, M. J. Zheng, W. Xu, W. Z. Shen, Fabrication of controllable free-standing ultrathin porous alumina membranes, Nanotechnology 16 (2005) 1285–1289.

[98] O. Cakir, Chemical etching of aluminum, Journal of Materials Processing Technology 199 (2008) 337–340.

[99] S. Allison, G. Gillies, Remote thermometry with thermographic phosphors: Instrumentation and applications, Review of Scientific Instruments 68 (7) (1997) 2615–2650.

[100] L. Goss, A. Smith, M. Post, Surface thermometry by laser-induced fluorescence, Review of scientific instruments 60 (12) (1989) 3702–3706.

[101] L.-S. Fan, Y. C. Tai, R. S. Muller, Ic-processed electrostatic micromotors, Sensors and actuators 20 (1) (1989) 41–47.

[102] A. H. Epstein, Millimeter-scale, micro-electro-mechanical systems gas turbine engines, Journal of Engineering for Gas Turbines and Power 126 (2) (2004) 205–226.

[103] B. E. Yoxall, M. L. Chan, R. S. Harake, T. Pan, D. A. Horsley, Rotary liquid droplet microbearing, Journal of Microelectromechanical Systems 21 (3) (2012) 721–729.

[104] M. Fortes, Axisymmetric liquid bridges between parallel plates, Journal of Colloid and Interface Science 88 (2) (1982) 338–352.

[105] K. Brakke, The surface evolver, version 2.70, august 25, 2013 (2013).
URL http://www.susqu.edu/brakke/evolver/evolver.html